Effect of Large Tidal Variation on Storm Surge in the Western Coastal Sea of Korea

Soo Youl KIM

2007

Effect of Large Tidal Variation on Storm Surge in the Western Coastal Sea of Korea

May 2007

by

Soo Youl KIM

A dissertation

Graduate School of Urban and Environment Engineering
Coastal and Offshore Disaster Division
Disaster Prevention Research Institute
in
Kyoto University

Acknowledgements

I am grateful to my supervisor Professor Tomotsuka Takayama, Associate Professor Hajime Mase and Assistant Professor Tomohiro Yasuda for their support and assistance throughout this study.

I would also like to thank Yoshida Foundation for the financial support during my PhD course in Japan.

I really thank my family, Father, Mather and my younger brogher in Korea giving me the opportunity to award the PhD and my wife Jung hwa Jo supporting me successfully as well as our junior who will be born at October 2007.

I want to thank Japanese students in the laboratory to help me stay in Japan.

Finally I would like to say thanks to Professors Jong Tae, Lee and Sei Eui, Yoon in Kyonggi University, and Tea Min, KIM who recommended me the PhD course in Japan.

February 13 2007

Soo Youl KIM

Contents

Chapter 1

Introduction

1.1.Review

Coastal inundation and damage have mainly occurred due to abnormal changes of the water level related to storm surge which is generated by the storm wind and atmospheric pressure depression induced by Hurricane, Cyclone and Typhoon. The disaster associated with those has caused the loss of life and property damage at the coastal region. In the Korean Peninsula surrounded by three sides of coasts, landfalls of typhoons have generally been concentrated to August from July such as Fig. 1.1 showing monthly tracks of typhoons according to Korean Meteorological Administration (KMA). The track of the typhoon passes through the Yellow Sea to either the northwest or west of Korean Peninsula on July. On the other hand, it is inclined to the southern part of the Korean Peninsula on August and passes the south coast. Therefore, the potential for the disaster due to the storm surge always exists on three coasts of Korean Peninsula.

The Korean Peninsula located among the East Sea (Japan Sea), the Yellow Sea and the South Sea has the coastline of 17,300km (including islands and the offshore islands of 3,418). The east coast is very steep and monotonous and has a small tidal range within 0.5m. However, the south and west coast are heavily indented coasts. Especially, the west coast is an area of geological

submergence which has produced many head lands, bays and hundreds of islands. Tidal flats up to 1,700km^2 are exposed at a low tide and a large tidal variation reaches up to 10m in the Kyunggi Bay. In the south coast different from the west coast, a tidal range is up to approximately either 1.0m or 2.0m.

Recently, the intensity and occurrence frequency of the typhoon have been increasing in terms of an atmospheric pressure and wind speed. In the western coast of Korea, life loss of 21 persons and property damage of about 20 million USD occurred due to Typhoon 0012 (Prapiroon) in 2000 and the maximum wind speed of 58m/s was observed which was on the third record since the observation was started in Korea. When it landed on, the central atmospheric pressure of 975 hPa was recorded. Typhoon 0314 (Maemi) with the central atmospheric pressure of 950 hPa and the wind speed of 38 m/s landed on the southern coast. Its maximum wind speed of 60m/s was observed at the Jeju island located in the south sea of the Korean Peninsula. It caused the life loss and missing of 129 persons and property damage of about 5.6 billion USD. This situation will continue and even greater storm surge disaster must be anticipated, since construction of adequate coastal defenses is, and may always remain, infeasible, on economic and technical grounds (Murty, 1986).

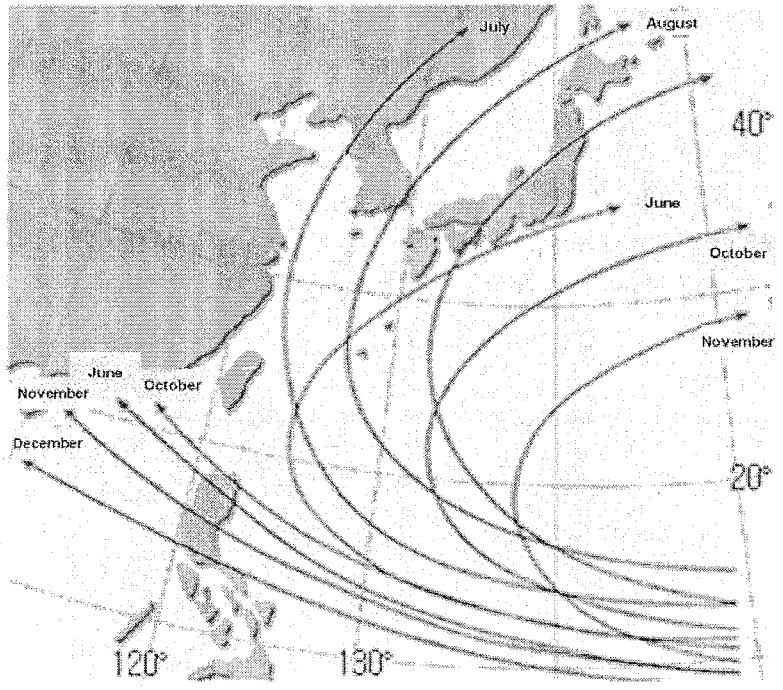

Fig. 1 1. Typhoon tracks around the Korea Peninsula (from KMA)

1.2. Background and purpose

Since the numerical modeling of the storm surge was developed and applied to the oceanic and coastal area, efforts of many researches have been concerned with the accurate hindcast and forecast of the storm surge due to Typhoon, Cyclone and Hurricane (Cheung et al. 2003, Choi et al. 2003, , Flather 1994, Murty et al. 1986, Mastenbroek et al. 1993, Moon 2004, Osuna et al. 2004, Ozer et al. 2000, Proctor et al. 1989, Peng et al. 2004, Takayama 2002 and 2004, Tang et al. 1996 and 1997). At the early stage, most attention had been paid to the modeling of only individual process such as the storm surge, tide and wind-driven current. For example, the only storm surge induced by the wind and atmospheric pressure had been considered and the storm surge modeling at the early stage had not accounted for the coastal processes such as the effect of the interaction among the tide, storm surge and wave even though it has been little known that the coastal processes will dynamically influence each other.

Murty et al. (1986) described the storm surge problem and provided an account of the factors affecting the generation of storm surges due to a cyclone in the Bay of Bengal. They focused on the only storm surge due to the cyclone even though the tide was implemented in their computation. Proctor et al. (1989) investigated the highest water levels in the Bristol Channel and severe flooding along the north Somerset coast induced by a secondary depression on the 13 December 1981. They made clear the failure of the high water level predicted due to an incorrect prediction by the atmospheric model used to provide the meteorological input to the sea model. Flather (1994) developed a numerical model for simulating and predicting tides and storm surges in regions that include areas of open sea combined with estuarine channels and intertidal banks. He showed that the timing of cyclone landfall and its coincidence with high tide determine the area worst affected by flooding. In addition, he showed that the differences in track and tidal conditions are to be important in a large area of the southern delta in 1970 and along the mainland coast south of Chittagong in 1990 by the comparison with two cyclones. Takayama (2002) described the present problems of the numerical simulations in a storm surge model to solve by the comparison with the multi and single layer model. He commonly recommended the single layer model but the multi layer model for a region with the rapid current. Takayama et al. (2004) also conducted the field investigation after the landfall of Typhoon 0314 (Maemi) in Korea. Their computation showed that the disaster was caused by not only the storm surge but also the storm waves. It was also failed to produce the accurate storm surge by the computation in comparison with the observation at Masan. Tang et al. (1996, 1997) applied a storm surge model to the North Queensland coast. They showed that the sea level with

the tides included in the storm surge model is generally lower than the tides added to the set-up. It has been commonly explained as a nonlinear interaction between the storm surge and tides. The authors demonstrated that this effect is due to the quadratic bottom friction law.

However, since a quasi-linear theory of wind-wave generation was introduced by Janssen (1989, 1991), significant efforts were made on the set-up simulation with respect to various interaction mechanisms among wave, surge and tide in the coupling model. Mastenbroek et al. (1993) studied the effect of a wave dependent drag coefficient on the generation of storm surges in the North Sea using the WAM wave and depth averaged Reynolds equation model. They clearly showed that the calculation with the wave dependent drag gives a significant improvement and preferred a wave dependent drag for a storm surge modeling. Ozer et al. (2000) developed generic module comprised of the storm surge, two dimensional shallow water equation and wave model, WAM-Cycle 4, and applied it to the North Sea and the Spanish coast. They showed that the sensitivity of waves increases due to the coupling with tide and surge in shallow sea more than in deep sea. This was explained by the importance of the two forcing components of the atmospheric pressure and the wind stress. Zhang et al. (1996) studied the interaction of waves and currents by the dynamical coupling of a third generation wave model and a two dimensional storm surge model. They also showed that the wave dependent drag coefficient improves the accuracy of the computed results. However, as far as the prediction of the wave height is concerned, it is better not to consider the wave radiation stress in the storm surge model. Choi et al. (2003) has established a coupled wave tide surge model composed of the two dimensional tide surge and wave model, WAM-Cycle 4, in order to investigate the effect of tides, storm surges and wind waves interactions during a winter monsoon in 1983. The changes of bottom friction factor generated by waves and current interactions are calculated by using simplified bottom boundary layer model. They determined the effective drag coefficient of the bottom stress from an iterative process followed by Grant et al. (1986). Their model simulations showed that the bottom velocity and effective bottom drag coefficient induced by the combination of wave and current were increased in shallow waters of up to 50m in the Yellow Sea. Cheung et al. (2003) developed a model package that simulates coastal flooding resulting from storm surge and waves generated by tropical cyclones consisting of four component models of storm surge, WAM, SWAN and Boussinesq model, respectively. The package was applied to hindcast the coastal flooding caused by the hurricane which hit the Hawaiian Islands. Their model indicated good agreement with the storm water levels and overwash debris lines recorded during and after events. Osuna et al. (2004) studied the wave current interaction process in the Southern North Sea using the coupling model applied by the nesting procedure from the ocean to coast. The simulation showed that the nesting procedure tends to improve the

qualitative agreement between computed wave parameters and measurements as well as the computed surge effect. Especially, the effect of radiation stress was found to be as important as considering the effect of a wave dependent surface stress in the coupling model. Moon (2004) investigates the impact of a coupled ocean wave tide circulation system on coastal modeling for wind waves, oceanic circulation and water mass simulation using coupling model composed of the wave model (WAVEWATCH-III) and the Princeton ocean model (POM) for the ideal winter and typhoon Winnie cases in the Yellow and East China Sea. In the Yellow and East China Sea the tides affect not only wind waves, but also seasonal circulation and water-mass distributions. The results show that the wave-dependent stress, which is strongly dependent on wave age and relative position from storm center, as well as the wave breaking have the most significant impact on the sea surface temperatures.

The most disaster due to the storm surge generated by the typhoon has been focused on the coastal region. The storm surge has been caused by the various factors such as the coastal processes, the magnitude of the typhoon and the characteristic of topography. Therefore, it is important for a certain region to understand the characteristic of the storm surge to prevent the coastal region and predict it. For example, the western coastal area of the Korean Peninsula, which is the motivated region in this study, has the large tidal variation of up to 10m. For this reason, the understanding of the characteristic of storm surge relating to the large tidal variation will give the information to the residents to deal with it. Moreover, it will be useful for engineers to design the structure such as a breakwater and sea wall since the water level is estimated by the tidal level just added to the storm surge level.

The main purpose of the study is

i. to develop the coupling model to hindcast the storm surge including the effect of waves
ii. to understand how a large tidal variation influences on the storm surge in the simplified bathymetry
iii. to understand how a large tidal variation influences on the set-up in the simplified bathymetry
iv. to understand how a large tidal variation influences on the storm surge at Gunsan in the western coastal region of Korea which the tidal range is large
v. to understand how a large tidal variation influences on the set-up at Gunsan in the western coastal region of Korea wich the tidal range is large
vi. to investigate the worst case at Gunsan in the western coastal region of Korea wich the tidal range is large

vii. To investigate the validity of the coupling model by hindcasting Typhoon 0603 (Ewiniar).

In chapter 2, the coupling model is explained, which is composed of the storm surge and wave model. The storm surge model is the horizontal 2-dimensional nonlinear shallow water equation in the Cartesian coordinated. The wave model, SWAN, is used to predict the waves. The typhoon model proposed by Fujita is used for the wind and the atmospheric pressure. The tide is imposed on open boundaries by the the tidal prediction model (Matsumoto et al., 2000). The coupling process is also described in detail. In order to calculate the high resolution, the nested scheme from the ocean to coastal region is applied to the coupling model by MPI (Message Passage Interface) on the Windows platform.

In chapter 3, the storm surge induced by the combination of the wind, atmospheric pressure and radiation stress and the set-up induced by the only radiation stress coinciding with the various tidal phases and amplitudes are investigated and discussed from the results of the numerical experiments in the ideal sea region. For the simplification, the wind is only considered as the force for the generation of the storm surge and five bottom slopes of 0.2, 0.1, 0.05 and 0.01 are chosen, which represent deep sea, intermediate sea and shallow sea. The tidal amplitudes of 0.5, 1.0, 2.0 and 3.0m are used for the large tidal variation.

In chapter 4, it is explained and discussed that how the large tidal variation influences on the storm surge induced by the combination of the wind, atmospheric pressure and radiation stress as well as the set-up induced by the only radiation stress using the coupling model at the western coastal region of Korea. It is assumed that Typhoon 0314 (Maemi), which hit the southern coastal area of Korea in 2003, hits the western coastal region. Since the tidal amplitude of up to 4.0m was observed at Gunsan of the study area, the tidal amplitudes of 1.0, 2.0, 3.0 and 4.0m are used for the large tidal variation. In addition, the worst case is discussed, which means the generation of the highest water level due to Typhoon 0314 (Maemi).

In chapter 5, storm surges and waves due to Typhoon 0603 (Ewiniar), which hit the western coastal area of the Korean Peninsula in 2006 was hindcasted and analyzed by the comparison with the observation data to confirm the applicability of the coupling model and then, the problem of the hindcast simulation in the coupling model is discussed.

Finally, Chapter 6 summarizes and concludes the study.

Chapter 2

Model description

In this chapter 2, the coupling model is explained in detail. At first, the storm surge model, wave dependent drag coefficient and radiation stress are described. Then, the typhoon and wave model are explained. Finally, the coupling process is depicted.

2.1. Storm surge/Tide model

The depth-integrated, nonlinear shallow water equations in the Cartesian coordinates are given by

$$\frac{\partial \eta}{\partial t} + \frac{\partial M}{\partial x} + \frac{\partial N}{\partial y} = 0 \tag{2.1.1}$$

$$\frac{\partial M}{\partial t} + \frac{\partial}{\partial x}\left(\frac{M^2}{d}\right) + \frac{\partial}{\partial y}\left(\frac{MN}{d}\right) + gd\frac{\partial \eta}{\partial x} =$$

$$fN - \frac{1}{\rho} d \frac{\partial P}{\partial x} + \frac{1}{\rho}(\tau_s^x - \tau_b^x + F_x) + A_h\left(\frac{\partial^2 M}{\partial x^2} + \frac{\partial^2 M}{\partial y^2}\right) \tag{2.1.2}$$

$$\frac{\partial N}{\partial t} + \frac{\partial}{\partial x}\left(\frac{NM}{d}\right) + \frac{\partial}{\partial y}\left(\frac{N^2}{d}\right) + gd\frac{\partial \eta}{\partial y} =$$

$$-fM - \frac{1}{\rho} d \frac{\partial P}{\partial y} + \frac{1}{\rho}(\tau_s^y - \tau_b^y + F_y) + A_h\left(\frac{\partial^2 N}{\partial x^2} + \frac{\partial^2 N}{\partial y^2}\right) \tag{2.1.3}$$

where, η = the sea surface fluctuation, M and N = the depth integrated currents in the x and y direction, P = the atmospheric pressure, f = the Coriolis parameter, g = the gravitational acceleration, $d=\eta+h$ = the total depth, A_h = the horizontal eddy diffusion and ρ = the density of water. F_x and F_y represent the components of the wave induced force which are the functions of the radiation stress in x and y space. At 2.3, these is explained in details. The bottom stresses is given by

$$\tau_b = \rho_w g n^2 \frac{U|U|}{d^{7/3}} \tag{2.1.4}$$

where n is the Manning coefficient, which 0.025, 0.02 and 0.015 are employed through the trial-error for the high resolution of each domain. The surface stress is usually given by

$$\tau_s = \rho_a C_D W_{10} |W_{10}| \tag{2.1.5}$$

where W_{10} is the wind speed measured at 10m above the sea surface. In the coupling model, this C_D in Eq. (2.1.5) will be replaced by a more elaborate form which is also explained at 2.2.

Eqs. (2.1.1), (2.1.2) and (2.1.3) are discretized in space on the staggered Arakawa C grid and in time using leap-frog method. The finite difference scheme is explicit and uses the first order forward and backward derivative for space and forward derivative for time. The nonlinear advective terms and the horizontal friction terms are computed by the first order upwind - central derivative and the second order one, respectively.

The boundary condition is given by zero flow normal to a solid boundary. The somefeld explicit method for the radiation condition is applied to the open boundary (Miller and Thorpe 1981, Palma 1998).

$$\phi_B^{n+1} = r\phi_{B\pm1}^n + (1-r)\phi_B^n \tag{2.1.6}$$

$$r = \begin{cases} 1 \; if \; C_n \geq 1 \\ C_n \;\; if \; 0 < C_n < 1 \\ 0 \; if \; C_n \leq 0 \end{cases} \tag{2.1.7}$$

$$C_n = \frac{\phi_{B\pm1}^n - \phi_{B\pm1}^{n-1}}{\phi_{B\pm2}^{n-1} - \phi_{B\pm1}^{n-1}} \tag{2.1.8}$$

where B is the boundary point and n denotes the time. ϕ stands for η. The disturbed water

surface at an open boundary is given by

$$\eta_n = \eta_{tide} + \eta_{storm\ surge} \tag{2.1.9}$$

where $\eta_{storm\ surge}$ is assumed as follows:

$$\eta_{storm\ surge} = (p_a - p_0)/g\rho \tag{2.1.10}$$

where p_a and p_0 represent 1013 hPa and the atmospheric pressure at the open boundary. η_{tide} is imposed by the ocean tide model for a regional model around Japan developed by Matsumoto (2000) which can make the realistic tide prediction. The wet/dry scheme is also applied for the sake of tidal flat simulation.

$$\begin{aligned} &If\,(D = h + \eta) \le 0.0005 \\ &\Rightarrow D = 0 \end{aligned} \tag{2.1.11}$$

where D represents the water depth, h; the mean water level and η; the water surface elevation.

2.2. Wind stress on sea surface

Janssen (1989, 1991, 1992) described the effect of wind generated gravity waves on the airflow and especially introduced that at the early stage of the wave development, a strong interaction between wind and wave is found under the constant wind speed in their result of the computation, resulting in a substantial increase of the stress in the surface layer.

Following the theory of Janssen, the total stress is the sum of a turbulent and a wave-induced stress as follows

$$\tau = \tau_{turb} + \tau_w \tag{2.2.1}$$

Here, τ_{turb} is the turbulent stress, which is modeled by a mixing length hypothesis,

$$\tau_{turb} = \rho_a (\kappa z)^2 \left(\frac{\partial U}{\partial z} \right)^2 \tag{2.2.2}$$

where κ (=0.4) is the von Karman constant and $U(z)$ the wind speed at height z. Based on the

numerical results of Janssen, the velocity profile still has a logarithmic shape for the young wind sea and is deviated from the profile of turbulent air flow over a flat plate. The velocity profile is assumed as follows

$$U(z) = \frac{u_*}{\kappa} \ln\left(\frac{z + z_e - z_0}{z_e}\right) \tag{2.2.3}$$

$$u_* = \sqrt{\tau / \rho_a} \tag{2.2.4}$$

where u_* is the friction velocity and z_0 represents the roughness length. The effective roughness length z_e at $z = z_0$ depends on z_0 and the sea state through the wave induced stress τ_w and the total surface stress τ.

$$z_e = \frac{z_0}{\sqrt{1 - \tau_w / \tau}} \tag{2.2.5}$$

$$z_0 = \hat{\alpha} \frac{u_*^2}{g} \tag{2.2.6}$$

Eq. (2.2.6) shows a Charnock-like relation in which $\hat{\alpha}$ is constant and 0.01. Since the drag coefficient defined by

$$C_D = u_*^2 / U(L)^2 = \left[\frac{\kappa}{\ln \frac{z + z_e - z_0}{z_e}}\right]^2 \tag{2.2.7}$$

is fully determined by the roughness length where $U(L)$ is the wind speed given at L and then, the drag coefficient C_D in Eq. (2.2.7) is alternatively used on the coupling model instead of one in Eq. (2.1.5). The wave stress · vector · τ_w is determined by

$$\tau_w = \rho_w \int_0^{2\pi} \int_0^{\infty} \omega S_{in}(\sigma, \theta) \frac{\bar{k}}{k} d\sigma d\theta \tag{2.2.8}$$

where σ is the angular frequency, S_{in} is the wind input source function, and k and $\bar{k}$ represent the wave-number of a wave component and the mean wave-number, respectively. In the SWAN model the iterative procedure of Mastenbroek (1993) is used to determine the surface stress, through this iterative procedure from Eqs. (2.2.3) to (2.2.8).

Janssen performed numerical experiments with a one gridpoint version of their coupled wave surface layer model. He showed that the stress induced by the wave becomes larger at the early stage of wave development under the steady state of the wind speed of U_{10} = 18.45m/s shown in Fig. 2.1 The evidence of that is also confirmed in Fig. 2.2 which shows the drag coefficient as a function of time for the uncoupled and coupled model under the same condition with Fig. 2.1. At the early stage of the wave field, the drag coefficient is enhanced under the constant wind speed. He implemented their coupled model on the limited area of the North Sea and Norwegian Sea. Fig. 2.3 gives a plot of drag coefficient as a function of wind speed U_{10} for North Sea hindcast in 1989 where c_p/u_* (with c_p the phase speed of the peak, u_* the friction velocity) represents the wave age. A realistic scatter in the relation of drag versus wind speed is found in comparison with the observation. It should be noted that the data was stratified for the drag by means of each wave age. Inspecting the expression for the roughness length z_e, it is obvious that a labeling of the data by means of τ_w / τ would be much more effective in stratifying the data. Consequently, the ratio τ_w / τ depends on the sea state. Hence, the surface stress will be enhanced if the ratio approaches one and behaved the Charnok relation of Eq. (2.2.6) if the ratio is small.

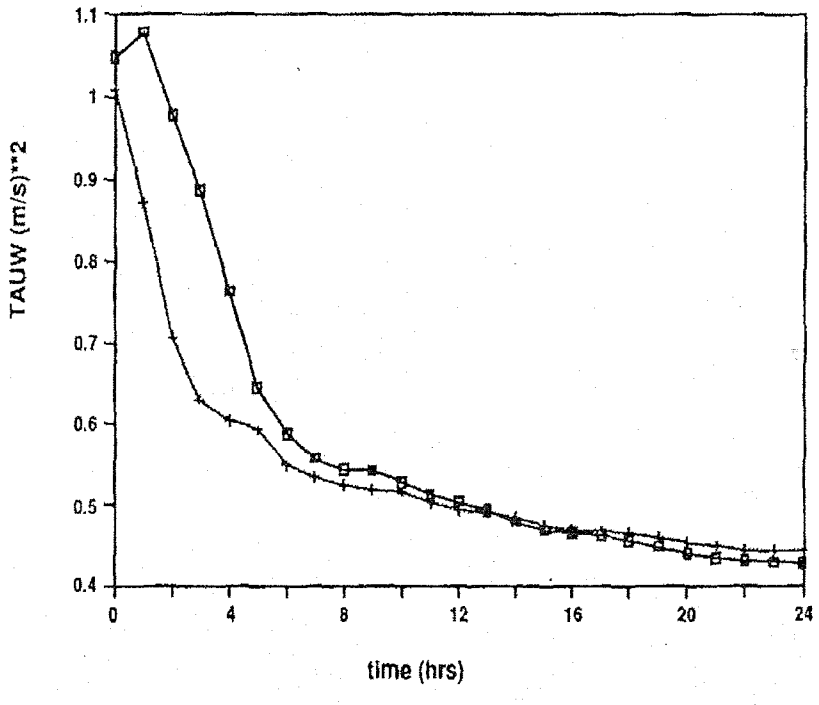

Fig. 2. 1. Wave induced stress as a function of time. Symbols: (+) uncoupled model, (□) coupled model in the case of U_{10} = 18.45m/s (Janssen 1991).

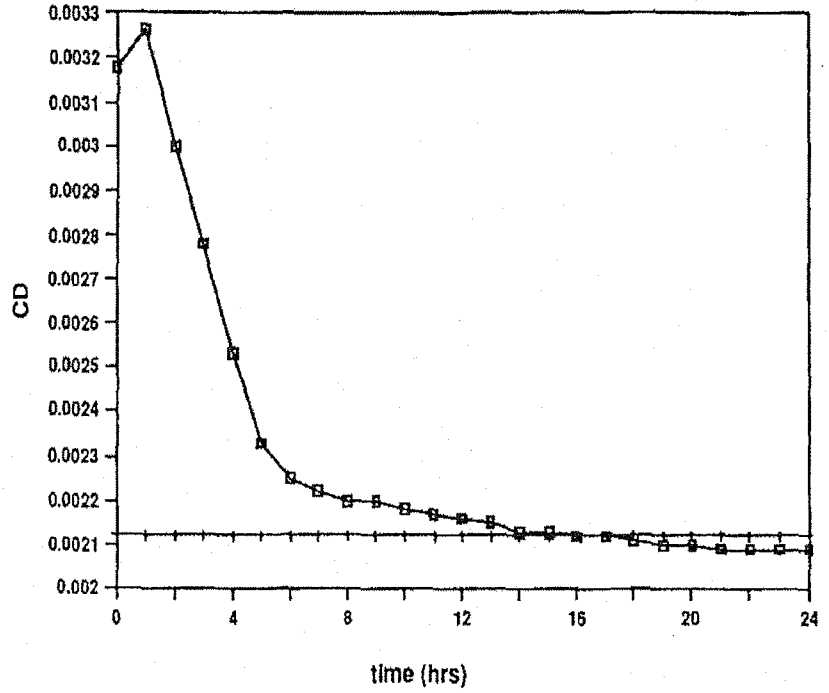

Fig. 2.2. Drag coefficient as a function of time for uncoupled model (+) and coupled model (□) in the case of U_{10} = 18.45m/s (Janssen 1991).

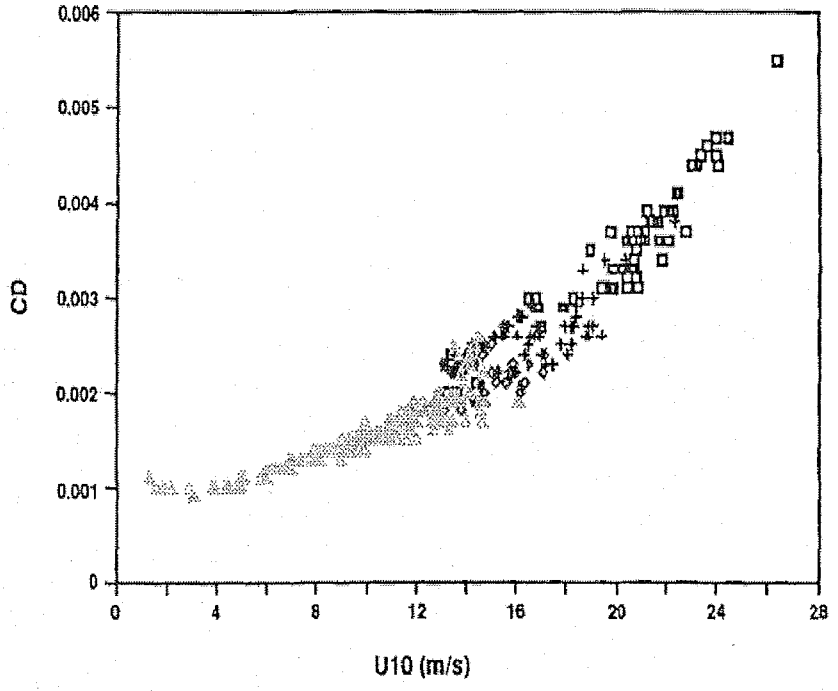

Fig. 2.3. Drag coefficient as a function of wind speed U_{10} for North Sea hindcast at DTG 89 1217:12. Results are labeled according to wave age c_p/u_*. Symbols: (□) 10< c_p/u_*<15, (+) 15<c_p/u_*<20, (◊) 20< c_p/u_*<25, (Δ) 25< c_p/u_* (Janssen 1991).

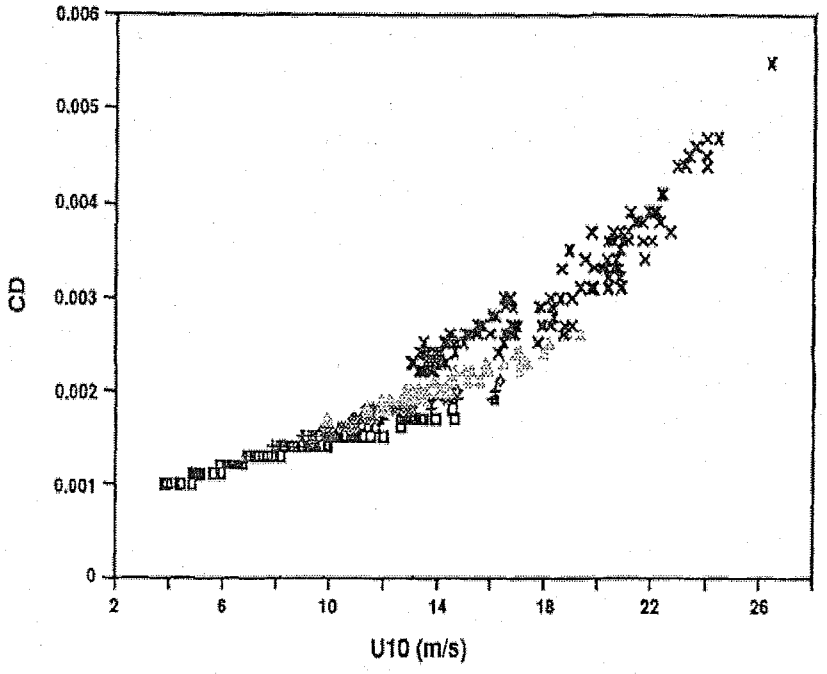

Fig. 2.4. As in Fig. 2.1 the results are labeled according to the ratio τ_w / τ. Symbols: (□) $\tau_w / \tau <$ 0.6, (+) 0.6 < τ_w / τ < 0.7, (◊) 0.7 < τ_w / τ < 0.8, (Δ) 0.8 < τ_w / τ < 0.9, (×) 0.9 < τ_w / τ < 1.0 (Janssen 1991).

2.3. Radiation stress

Waves are the prime movers for the littoral processes at the shoreline. For the most part, they are generated by the action of the wind over water. These waves transport the energy imparted to them over vast distances, for dissipative effects, such as viscosity, play only a small role. Waves are always present at coastal sites (Dean and Dalrymple 2002). Longuet-Higgins and Stewart (1962, 1964) proposed the concept of the radiation stress which represents the contribution of the wave motion to the mean flux of horizontal momentum considering the flux of momentum. Phillips (1966) and Mei (1989) deviated it from the momentum or energy equation as well.

The instantaneous horizontal flux of momentum at a given location consists of the pressure force on a vertical plane plus the transfer of momentum through that vertical plane. Dividing by the area of the vertical plane yields the momentum flux for the x direction which is

$$p + \rho u^2$$

The resulting radiation stress S_{xx} for a wave propagating in the x direction is

$$S_{xx} = \overline{\int_{-h}^{\eta} \left(p + \rho u^2\right) dz} - \int_{-h}^{0} \rho g z \, dz \tag{2.3.1}$$

where the subscript xx denotes the x directed momentum flux across a plane defined by x = constant. In the equation shown above p is the total static plus dynamic pressure so that the static pressure must be subtracted to obtain the radiation stress for the wave. The overbar denotes that the term is averaged over the wave period.

Particle velocity:

$$\begin{aligned} u &= \frac{\pi H}{T}\left[\frac{\cosh k(h+z)}{\sinh kh}\right]\cos(kx - \sigma t) \\ w &= \frac{\pi H}{T}\left[\frac{\sinh k(h+z)}{\sinh kh}\right]\sin(kx - \sigma t) \end{aligned} \tag{2.3.2}$$

Pressure filed:

$$p = -\rho g z + \frac{\rho g H}{2}\left[\frac{\cosh k(h+z)}{\cosh kh}\right]\cos(kx - \sigma t) \tag{2.3.3}$$

where H is a wave height, h the depth, z the perturbed surface water level, k the wave number, σ the wave angular frequency, g the gravity, ρ the water density. Inserting the pressure and particle velocity terms of Eq. (2.3.2) and (2.3.3) from the small amplitude theory yields

$$S_{xx} = \frac{\rho g H^2}{8}\left[\frac{1}{2} + \frac{2kh}{\sinh 2kh}\right] = E\left(2n - \frac{1}{2}\right) \tag{2.3.4}$$

with $E = \frac{\rho g H^2}{8}, n = \frac{1}{2}\left[1 + \frac{2kh}{\sinh 2kh}\right]$.

Likewise, the y directed momentum flux across a plane defined by y = constant is

$$S_{yy} = \frac{\rho g H^2}{8}\left[\frac{kh}{\sinh kh}\right] = E\left(n - \frac{1}{2}\right) \tag{2.3.5}$$

The radiation stress components S_{xy} and S_{yx} are both zero. Note, in deep water

$$S_{xx} = \frac{E}{2},\ S_{yy} = 0 \tag{2.3.6}$$

and in shallow water

$$S_{xx} = \frac{3E}{2},\ S_{yy} = \frac{E}{2} \tag{2.3.7}$$

If wave is propagating in a direction that is at an angle with the x direction the radiation stress tensor S_{ij} can be represented in terms of the wave energy spectrum E

$$S_{xx} = \rho g \int\int \left[\frac{C_g}{C}\cos^2\theta + \frac{C_g}{C} - \frac{1}{2}\right] E\, d\sigma d\theta \tag{2.3.8}$$

$$S_{xy} = S_{yx} = \rho g \int\int [\cos\theta \sin\theta] E\, d\sigma d\theta \tag{2.3.9}$$

$$S_{yx} = \rho g \int\int \left[\frac{C_g}{C}\cos^2\theta + \frac{C_g}{C} - \frac{1}{2}\right] E\, d\sigma d\theta \tag{2.3.10}$$

in which C represents the wave celerity and C_g the wave group velocity. Therefore, the wave induced forces due to radiation stress on the momentum equations (2.1.2) and (2.1.3) are as follows

$$F_x = -\frac{\partial S_{xx}}{\partial x} - \frac{\partial S_{xy}}{\partial y} \tag{2.3.11}$$

$$F_y = -\frac{\partial S_{yx}}{\partial x} - \frac{\partial S_{yy}}{\partial y} \tag{2.3.12}$$

Note that Eqs. (2.3.11) and (2.3.12) are dependent on the space. The radiation stress components presented above are useful for analyzing a number of wave phenomena, including mean water level set up in the surf zone, wave-current interaction, and the alongshore currents generated in the surf zone by waves that obliquely approach the shore (Sorensen 1993).

2.4. Typhoon model

Takayama (2002) explained the typhoon model of Fujita, Myers and Mitsuda-Fujii in detail. He described that the difference of the wind distribution calculated from three models is very small under the same condition, resulting in the similar wind distribution and wind speed. From this reason, Fujita model is employed to produce the atmospheric pressure and the wind distribution of the typhoon in the study. This section accounts for Fujita model as well as Myers and Mitsuda-Fujii model.

2.4.1. Wind distribution in the typhoon

A wind speed at a point far from a typhoon is represented

$$\frac{V_{gr}^2}{r} + fV_{gr} = \frac{1}{\rho_a}\frac{\partial p}{\partial r} \tag{2.4.1}$$

where r is the distance from the center of the typhoon, V_{gr} ; the gradient wind, f; the Coriolis force and p; the atmospheric pressure. The speed of gradient wind is calculated using Eq. (2.4.1)

$$V_{gr} = r\left[\sqrt{\frac{f^2}{4} + \frac{1}{\rho_a r}\frac{\partial p}{\partial r}} - \frac{f}{2}\right] \tag{2.4.2}$$

where f is the Coriolis force, p; the atmospheric pressure and r; the radial distance from the typhoon center. The gradient wind is modified due to the friction of the sea and land surface. The gradient wind speed experienced by the surface friction is represented

$$W_{gr}^X = -C_2\frac{X + \sqrt{3}Y}{2r}V_{gr} \tag{2.4.3}$$

$$W_{gr}^Y = C_2\frac{\sqrt{3}X + Y}{2r}V_{gr} \tag{2.4.4}$$

where, C_2 is the reduction coefficient and 0.7 is usually used as the value of C_2. The moving speed of the typhoon also influences on the wind speed. The wind speed affected by the moving speed of the typhoon is

$$V_t = C_1 V \exp\left(-\frac{\pi r}{l}\right) \tag{2.4.5}$$

where V_t is the wind speed of typhoon and the values of l is used as 500,000m to make $V_t = exp(-\pi)$ when r is chosen as 500km. The reduction coefficient, C_1, due to the friction of sea and land surface is also used and has the same value as C_2 in Eq. (2.4.3) and (2.4.4). The wind speed in x and y direction is determined by

$$V_x = V_t \cos\theta_t \tag{2.4.6}$$

$$V_y = V_t \sin\theta_t \tag{2.4.7}$$

where θ_t is at an angle with x axis on an anticlockwise rotation. Finally, the wind speeds at 10m above the sea surface is represented by the vector sum between the gradient wind speed reduced by the sea or land surface friction and the wind speed affected by the moving speed of typhoon. Those are determined by

$$W_x = C_1 V \exp\left(-\frac{\pi r}{l}\right)\cos\theta_t - C_2 V_{gr}\frac{X + \sqrt{3}Y}{2r} \tag{2.4.8}$$

$$W_y = C_1 V \exp\left(-\frac{\pi r}{l}\right)\sin\theta_t + C_2 V_{gr}\frac{\sqrt{3}X - Y}{2r} \tag{2.4.9}$$

2.4.2 Fujita model

The pressure field from the center of typhoon is determined by

$$p = p_\infty - \frac{\Delta p}{\sqrt{1 + (r / r_0)^2}} \tag{2.4.10}$$

where p_∞ and Δp represent the environmental pressure far from its center and the pressure gradient in space, and r and r_0 denote the radial distance at a station and the radius of the maximum wind speed from the typhoon center, respectively. Using Eq. (2.4.10), the gradient of

the pressure $\frac{\partial p}{\partial r}$ is obtained by

$$\frac{\partial p}{\partial r} = \frac{r\Delta p}{r_0^2}\left\{1+\left(\frac{r}{r_0}\right)^2\right\}^{-3/2} \tag{2.4.11}$$

Substituting Eqs. (2.4.11) into (2.4.2), the gradient of wind is calculated by

$$V_{gr} = r\left[\sqrt{\frac{f^2}{4}+\frac{\Delta p}{\rho_a r_0^2}\left\{1+\left(\frac{r}{r_0}\right)^2\right\}^{-3/2}} - \frac{f}{2}\right]. \tag{2.4.12}$$

Through Eqs. (2.4.3) to (2.4.7), the wind speed at 10m on the sea surface is calculated by Eqs. (2.4.8) and (2.4.9). The radius of maximum wind speed, r_0 is estimated by using the pressure data observed at meteorological station.

2.4.3. Myers model

The pressure field from the center of typhoon is determined by

$$p = p_c + \Delta p \exp\left(-\frac{r_0}{r}\right) \tag{2.4.13}$$

Using Eq. (2.4.13), the gradient of the pressure is represented by

$$\frac{\partial p}{\partial r} = \frac{r_0\Delta p}{r^2}\exp\left(-\frac{r_0}{r}\right) \tag{2.4.14}$$

Substituting Eq. (2.4.14) into (2.4.2), the gradient of wind is calculated by

$$V_{gr} = r\left[\sqrt{\frac{f^2}{4}+\frac{r_0\Delta p}{\rho_a r^3}\left(-\frac{r_0}{r}\right)} - \frac{f}{2}\right]. \tag{2.4.15}$$

Through Eq. (2.4.3) to (2.4.7), the wind speed at 10m above the sea surface is calculated by Eqs. (2.4.8) and (2.4.9).

2.4.4. Mitsuda-Fujii model

A wind speed at a point far from the center of typhoon is represented

$$\frac{V_{gr}^2}{r_t} + fV_{gr} = \frac{1}{\rho_a}\frac{\partial p}{\partial r} \tag{2.4.16}$$

where,

$$\frac{1}{r_t} = \frac{1}{r}\left(1 + \frac{V}{V_{gr}}\sin\beta\right) \tag{2.4.17}$$

Using Eq. (2.4.16) the gradient wind is obtained by

$$V_{gr} = r\left[\sqrt{\frac{f^2}{4} + \frac{r_0 \Delta p}{\rho_a r^2 r_t}\exp\left(-\frac{r_0}{r}\right)} - \frac{f}{2}\right] \tag{2.4.18}$$

From the result of measurement, it was investigated that the ratio of the wind at 10m to the gradient wind becomes larger near the only center of the typhoon. This ratio is represented by

$$\frac{W}{V_{gr}} = G(\xi) = G(\infty) + \left\{G(\xi_p) - G(\infty)\right\}\left(\frac{\xi}{\xi_p}\right)^{k-1}\exp\left[\left(1-\frac{1}{k}\right)\left\{1-\left(\frac{\xi}{\xi_p}\right)^k\right\}\right] \tag{2.4.19}$$

The ratio of the wind $G(\xi)$ is parameterized by Mitsuda-Fujii as follows:

$$k = 2.5,\ \xi_p = 0.5,\ G(\xi_p) = 1.2,\ G(\infty) = 2/3$$

where $G(\infty)$ corresponds to C_2 in Eq. (2.4.3) and (2.4.4). Therefore, the wind speed at 10m above the sea surface, which blows to the center of typhoon with 30 degrees of the gradient wind, is represented by

$$W_x = -G(\xi)V_{gr}\frac{X + \sqrt{3}Y}{2r} \tag{2.4.20}$$

$$W_y = G(\xi)V_{gr}\frac{\sqrt{3}X + Y}{2r} \tag{2.4.21}$$

2.5. Wave model

A third-generation numerical wave model (SWAN) to compute random, short-crested waves in coastal regions with shallow water and ambient current was developed and verified by Booij et al. (1999). The model can be applied to coastal regions with shallow water, islands, tidal flats and local wind as well as with horizontal scales less than 20-30*km* and water depths less than 20-30*m*. In addition, SWAN can be used on any scale relevant for wind generated surface gravity waves. However, SWAN is specifically designed for coastal applications that should actually not require such flexibility in scale. SWAN is allowed to be used from laboratory conditions to shelf seas and nested in the WAM or WAVEWATCH Ⅲmodel.

This model accounts for shoaling, refraction, generation by wind, whitecapping, triad and quadruplet wave-wave interactions, and bottom and depth-induced wave breaking. The basic equation in SWAN is the wave action balance equation and is given by

$$\frac{\partial}{\partial t}N+\frac{\partial}{\partial x}c_x N+\frac{\partial}{\partial y}c_y N+\frac{\partial}{\partial \sigma}c_\sigma N+\frac{\partial}{\partial \theta}c_\theta N=\frac{S}{\sigma} \tag{2.5.1}$$

Where,

$$S=S_{phil}+S_{in}+S_{nl4}+S_{ds}+S_{bf} \tag{2.5.2}$$

in the Cartesian coordinates (x, y). Here, $N(\sigma, \theta)$ is the action density spectrum, c_x and c_y present the group velocities in x and y direction, c_σ and c_θ also present the one in σ and θ direction and S is the source terms. t is the time, x and y present the space in geographic grid, in contrast with σ and θ are the frequency and its direction of a wave component.

The first term on the left side of Eq. (2.5.1) represents the local rate of change of the action density in time and the second and third term represent propagation of action in x and y space, respectively. The fourth term represents shifting of the relative frequency due to variation in depths and currents. The fifth term represents wave refraction induced by sea depth and current. All terms except first one include the propagation velocity in geographical, σ and θ space. The term $S(\sigma, \theta)$ at the right-hand side of Eq. (2.5.2) is the source term in terms of energy density, representing the effects of generation, nonlinear wave-wave interactions and

dissipation.

Time is discretized with a simple constant time step for the simultaneous integration of the propagation and the source terms in contrast with it in the WAM model or the WAVEWATCH model. The discrete frequencies are defined between a fixed low-frequency cutoff (typically, f_{min}=0.04Hz) and a fixed high-frequency cutoff (typically, f_{max}=1.0Hz) which are defined by the user and computed by SWAN, respectively. SWAN allows the use of nested grids to provide high-resolution results at desired locations and provides estimates of wave setup due to radiation stress.

Although the SWAN model includes various source terms and the user can optionally choose each source term to compute and apply it to the shelf or experimental sea, default values for the source terms are basically used in the study. The reason is that the purpose of the study is not focused on the validation of each source term in the study area. In addition, the theory of Jannsen (1989, 1991) is applied to the exponential growth term by the wind to compute the wave dependent drag coefficient. However, the theory of Jannsen could not accurately produce the wave height compared to the observation on SWAN. Lalbeharry (2004) modified the original limiter described by Ris (1997) and produced the accurate wave height. The source terms in SWAN are described from 2.5.1 to 2.5.3 with the priority given to the theory of Janssen. The modified part by Lalbeharry (2004) is explained at 2.5.4.

2.5.1. Input by wind (S_{in})

Wave growth by wind is described by

$$S_{in}(\sigma,\theta) = A + BE(\sigma,\theta) \tag{2.5.3}$$

in which A describes linear growth and BE exponential growth in which $E(\sigma,\theta)$ denotes the directional spectrum. For the WAM Cycle 3 formulation the transformation from U_{10} to U_* is obtained with

$$U_*^2 = C_D U_{10}^2 \tag{2.5.4}$$

in which C_D is the drag coefficient from Wu (1982)

$$C_D = \begin{cases} 1.2875\times10^{-3} & for\, U_{10} < 7.5 m/s \\ (0.8 + 0.065\times U_{10})\times10^{-3} & for\, U_{10} \geq 7.5 m/s \end{cases} \qquad (2.5.5)$$

2.5.1.1. Linear growth by wind

For the linear growth term A, the expression due to Cavaleri and Malanotte-Rizzoli (1981) is used with a filter to eliminate wave growth at frequencies lower than the Pierson-Moskowitz frequency (Tolman, 1992).

$$A = \frac{1.55\times10^{-3}}{g^2 2\Pi}\left[U_* \max[0, \cos(\theta - \theta_w)]\right]^4 H \,, \qquad (2.5.6)$$

$$H = \exp\left(-\left(\sigma / \sigma^*_{PM}\right)^{-4}\right) \qquad with \quad \sigma^*_{PM} = \frac{0.13g}{28U_*} 2\Pi \,,$$

where θ_w is the wind direction, H is the filter and σ^*_{PM} is the peak frequency of the fully developed sea state according to Pierson and Moskowitz.

2.5.1.2. Exponential growth by wind

SWAN optionally allows two kinds of expressions of Komen and Jansssen. In the paper, the expression due to Janssen (1989, 1991) is only described and used. It is based on a quasi-linear wind-wave theory and is given by

$$B = \beta \frac{\rho_a}{\rho_w}\left(\frac{U_*}{C_{ph}}\right)^2 \max[0, \cos(\theta - \theta_w)]^2 \sigma \qquad (2.5.7)$$

where β is the Miles "constant". In the theory of Janssen (1991), this Miles constant is estimated from the non-dimensional critical height λ

$$\begin{cases} \beta = \dfrac{1.2}{\kappa^2}\lambda \ln\lambda^4 & , \quad \lambda \leq 1 \\ \lambda = \dfrac{gz_e}{C_{ph}^2} e^r & , \quad r = \kappa c / |0, \cos(\theta - \theta_w)| \end{cases} \qquad (2.5.8)$$

where κ is the Von karman constant, equal to 0.41 and z_e is the effective surface roughness. Janssen (1991) assumes that the wind profile is given by Eq. (2.2.3). The effective roughness length z_e depends on the roughness length z_0 and the sea state through the wave induced stress τ_w and the total surface stress $\tau = \rho_a |U_*| U_*$ by Eqs. (2.2.5) and (2.2.6). The wave stress τ_w is given by Eq. (2.2.8).

2.5.2. Dissipation of wave energy (S_{ds})

2.5.2.1. Whitecapping

The processes of whitecapping in the SWAN model are represented by the pulse-based model of Hasselmann (1974). Reformulated in terms of wave number (rather than frequency) so as to be applicable infinite water depth (the WAMDI group, 1988), this expression is

$$S_{ds,w}(\sigma,\theta) = -\Gamma \tilde{\sigma} \frac{k}{\tilde{k}} E(\sigma,\theta), \tag{2.5.9}$$

Where, $\tilde{\sigma}$ and $\tilde{k}$ denote the mean frequency and the mean wave number respectively and the coefficient Γ depends on the overall wave steepness. This steepness dependent coefficient, as given by the WAMDI group (1988), has been adapted by Günther et al. (1992) based on Janssen (1991) :

$$\Gamma = \Gamma_{KJ} = C_{ds}\left((1-\delta)+\delta\frac{k}{\tilde{k}}\right)\left(\frac{\tilde{s}}{\tilde{s}_{PM}}\right)^P , \tag{2.5.10}$$

Where, the coefficients C_{ds}, δ and p are tunable coefficients, $\tilde{s}$ is the overall wave steepness, $\tilde{s}_{PM}$ is the value of $\tilde{s}$ for the Pierson-Moskowitz spectrum (1967; $\tilde{s}_{PM} = \left(3.02\times10^{-3}\right)$). This overall wave steepness $\tilde{s}$ is defined as:

$$\tilde{s} = \tilde{k}\sqrt{E_{tot}} \ . \tag{2.5.11}$$

The mean frequency $\tilde{\sigma}$, the mean wave number $\tilde{k}$ and the total wave energy: E_{tot} are defined as (the WAMDI group, 1988):

$$\tilde{\sigma} = \left(E_{tot}^{-1} \int_0^{2\Pi} \int_0^{\infty} \frac{1}{\sigma} E(\sigma,\theta) d\sigma \, d\theta \right)^{-1} , \tag{2.5.12}$$

$$\tilde{k} = \left(E_{tot}^{-1} \int_0^{2\Pi} \int_0^{\infty} \frac{1}{\sqrt{k}} E(\sigma,\theta) d\sigma \, d\theta \right)^{-2} , \tag{2.5.13}$$

$$E_{tot} = \int_0^{2\Pi} \int_0^{\infty} \frac{1}{\sigma} E(\sigma,\theta) d\sigma \, d\theta \ . \tag{2.5.14}$$

The values of the tunable coefficients C_{ds}, δ and exponent p in this model have been obtained by Komen et al. (1984) and Janssen (1992) by closing the energy balance of the waves in idealized wave growth conditions for deep water. This implies that coefficients in the steepness dependent coefficient Γ depend on the wind input formulation that is used. Since two different wind input formulations are used in the SWAN model, two sets of coefficients are used. For the wind input of Janssen (1992), $C_{ds} = 4.10 \times 10^{-5}$ and $\delta = 0.5$ is used (assuming p = 4) in the paper.

2.5.2.2. Bottom friction

The bottom fiction models that have been selected for SWAN are the empirical model of JONSWAP (Hasselmamn et al., 1973), the drag law model of Collins (1972) and the eddy-viscosity model of Masen et al. (1988). In this study, the empirical model of JONSWAP is selected and only described. The formulations for these bottom friction models can all be expressed in the following form:

$$S_{ds,b}(\sigma,\theta) = -C_{bottom} \frac{\sigma^2}{g^2 \sinh^2(kd)} E(\sigma,\theta) , \tag{2.5.15}$$

in which C_{bottom} is a bottom friction coefficient that generally depends on the bottom orbital motion represented by U_{rms} :

$$U_{rms}^2 = \int_0^{2\Pi} \int_0^{\infty} \frac{\sigma^2}{\sinh^2(kd)} E(\sigma,\theta) d\sigma \, d\theta \ . \tag{2.5.16}$$

Hassemann et al. (1973) found from the results of the JONSWAP experiment $C_{bottom} = C_{JON} = 0.038 m^2 s^{-3}$ for swell condition.

2.5.2.3. Depth-induced wave breaking

To model the energy dissipation in random waves due to depth-induced breaking, the bore-based model of Battjes and Janssen (1978) is used in SWAN. The mean rate of energy dissipation per unit horizontal area due to wave breaking D_{tot} is expressed as:

$$D_{tot} = -\frac{1}{4}\alpha_{BJ} Q_b \left(\frac{\overline{\sigma}}{2\Pi}\right) H_m^2 \quad , \tag{2.5.17}$$

in which $\alpha_{BJ} = 1$ in SWAN, Q_b is the fraction of breaking waves determined by:

$$\frac{1-Q_b}{\ln Q_b} = -8\frac{E_{tot}}{H_m^2} \quad , \tag{2.5.18}$$

in which H_m is the maximum wave height that can exist at the given depth and $\overline{\sigma}$ is a mean frequency defined as:

$$\overline{\sigma} = E_{tot}^{-1} \int_0^{2\Pi} \int_0^{\infty} \sigma E(\sigma,\theta)\, d\sigma\, d\theta \quad . \tag{2.5.19}$$

The fraction of depth-induced breakers (Q_b) is determined in SWAN with

$$\begin{aligned} Q_b &= 0 && \text{for } \beta \le 0.2 \\ Q_b &= Q_0 - \beta^2 \frac{Q_0 - \exp\left((Q_0-1)/\beta^2\right)}{\beta^2 - \exp\left((Q_0-1)/\beta^2\right)} && \text{for } 0.2 < \beta < 1 \text{ one step Newton-Raphson iteration} \\ Q_b &= 1 && \text{for } \beta \ge 1 \end{aligned} \tag{2.5.20}$$

where $\beta = H_{rms} / H_{max}$. For $\beta \le 0.5$, $Q_0 = 1$ and for $0.5 < \beta \le 1$, $Q_0 = (2\beta - 1)^2$. Extending the expression of Eldeberky and Battjes (1995) to include the spectral directions, the dissipation for a spectral component per unit time is calculated in SWAN with:

$$S_{ds,br}(\sigma,\theta) = D_{tot}\frac{E(\sigma,\theta)}{E_{tot}}. \qquad (2.5.21)$$

The maximum wave height H_m is determined in SWAN with $H_m=yd$, in which y is the breaker parameter and d is the total water depth.

2.5.3. Nonlinear wave-wave interactions (S_{nl})

2.5.3.1. Quadruplet wave interactions

The quadruplet wave-wave interactions are computed with the Discrete Interaction Approximation (DIA) as proposed by Hasselmann et al. (1985). Their source code has been in SWAN. In the DIA, two quadruplets of wave numbers are considered, both with frequencies.

$$\begin{aligned} \sigma_1 &= \sigma_2 &&= \sigma \\ \sigma_3 &= \sigma(1+\lambda) &&= \sigma^+ , \\ \sigma_4 &= \sigma(1-\lambda) &&= \sigma^- \end{aligned} \qquad (2.5.22)$$

where λ is a constant coefficient set equal to 0.25. To satisfy the resonance conditions for the first quadruplet, the wave number vectors with frequency σ_3 and σ_4 lie at an angle of $\theta_1 = -11.5^0$ and $\theta_2 = 33.6^0$ to the two identical wave number vectors with frequencies σ_1 and σ_2. The second quadruplet is the mirror of this first quadruplet.

Within this discrete interaction approximation, the source term $S_{nl4}(\sigma,\theta)$ is given by:

$$S_{nl4}(\sigma,\theta) = S^*_{nl4}(\sigma,\theta) + S^{**}_{nl4}(\sigma,\theta), \qquad (2.5.23)$$

where S^*_{nl4} refers to the first quadruplet and S^{**}_{nl4} to the second quadruplet and:

$$\begin{aligned} \delta S_{nl4}(\alpha_i\sigma,\theta) = C_{nl}(2\Pi)^2 g^{-4}\left(\frac{\sigma}{2\Pi}\right)^{11}\left[E^2(\sigma,\theta)\left(\frac{E(\alpha_i\sigma^+,\theta)}{(1+\lambda)^4}\right)+\left(\frac{E(\alpha_i\sigma^-,\theta)}{(1-\lambda)^4}\right)\right] \\ -2\frac{E(\alpha_i\sigma,\theta)(\alpha_i\sigma^+,\theta)(\alpha_i\sigma^-,\theta)}{(1-\lambda^2)^4} \end{aligned} \qquad (2.5.24)$$

The constant $C_{nl4} = 3\times10^7$. Following Hasselmann (1981), the quadruplet interaction in finite

water depth is taken identical to the quadruplet transfer in deep water multiplied with a scaling factor R:

$$S_{nl4,finitedepth} = R(k_p d) S_{nl4,\text{infinitedepth}} , \tag{2.5.25}$$

where R is given by

$$R(k_p d) = 1 + \frac{C_{sh1}}{k_p d}\left(1 - C_{sh2} k_p d\right)\exp\left(C_{sh3} k_p d\right), \tag{2.5.26}$$

in which k_p is the peak wave number of the JONSWAP spectrum for which the original computations were carried out. The values of the coefficients are: C_{sh1} = 5.5, C_{sh1} =6/7 and C_{sh3} = -1.25. In the shallow water limit, i.e., $k_p d \rightarrow 0$, the nonlinear transfer tends to infinity. Therefore a lower limit of $k_p d = 0$ is applied, resulting in a maximum value of $R(k_p d)$ =4.43. To increase the model robustness in case of arbitrarily shaped spectra, the peak wave number k_p is replaced by $k_p = 0.75\tilde{k}$ (Komen et al., 1994).

2.5.3.2. Triad wave-wave interactions

The Lumped Triad Approximation (LTA) of Eldeberky (1996) which is a slightly adapted version of the Discrete Triad Approximation of Eldeberky and Battjes (1995) is used in SWAN in each spectral direction:

$$S_{nl3}(\sigma,\theta) = S^{-}_{nl3}(\sigma,\theta) + S^{+}_{nl3}(\sigma,\theta) \tag{2.5.27}$$

with

$$S^{+}_{nl3}(\sigma,\theta) = \max\left\{0, \alpha_{EB} 2\Pi c c_g J^2 \left|\sin(\beta)\right| \left\{E^2(\sigma/2,\theta) - 2E(\sigma/2,\theta)E(\sigma,\theta)\right\}\right\} \tag{2.5.28}$$

and $S^{-}_{nl3}(\sigma,\theta) = -2S^{+}_{nl3}(2\sigma,\theta)$ (2.5.29)

in which α_{EB} is a tunable proportionality coefficient. The bi-phase β is approximated with

$$\beta = -\frac{\Pi}{2} + \frac{\Pi}{2}\tanh\left(\frac{0.2}{Ur}\right) \tag{2.5.30}$$

with $\overline{T} = 2\Pi/\overline{\sigma}$. Usually, the triad wave-wave interactions are calculated only for $0.1 \leq Ur \leq 10$. But for stability reasons, it is calculated for the whole range $0 \leq Ur \leq 10$. This means that both quadruplets and triads are computed at the same time. The interaction coefficient J is taken from Madsen and Sorensen (1993).

2.5.3.3. Diffraction

In a simple case, it is assumed that there are no currents. This means that $C_\sigma = 0$. Let denotes the progation velocities in geographic and spectral spaces for the situation without diffraction as: $C_{x,0}$, $C_{y,0}$ and $C_{\theta,0}$. These are given by:

$$C_{x,0} = \frac{\partial\omega}{\partial k}\cos(\theta),\quad C_{y,0} = \frac{\partial\omega}{\partial k}\sin(\theta),\quad C_{\theta,0} = \frac{\partial\omega}{\partial h}\frac{\partial h}{\partial n} \tag{2.5.31}$$

where k is the wave number and n is perpendicular to the wave ray. It is considered the following eikonal equation:

$$K^2 = k^2(1+\delta) \tag{2.5.32}$$

with δ denoting the diffraction parameter as given by:

$$\delta = \frac{\nabla\left(cc_g\nabla H_s\right)}{cc_g H_s} \tag{2.5.33}$$

Due to diffraction, the propagation velocities are given by:

$$c_x = c_{x,0}\overline{\delta},\quad c_y = c_{y,0}\overline{\delta},\quad C_\theta = C_{\theta,0}\overline{\delta} - \frac{\partial\overline{\delta}}{\partial x}c_{y,0} + \frac{\partial\overline{\delta}}{\partial y}c_{x,0} \tag{2.5.34}$$

Where $\overline{\delta} = \sqrt{1+\delta}$.

2.5.4. Modified by Lalbeharry

Lalbeharry et al. (2004) showed that the modified version of the SWAN implementation of WAM4 produces wave heights that are more accurate than those of the unmodified version by applying the wave growth limiter in the exponential wind growth source term on WAM 4.5 to one instead of the original limiter described by Ris (1997) on SWAN. The shift growth parameter Z_α=0.0011 is also included. The original limiter implemented on SWAN is

$$\left|\Delta N(\sigma,\theta)\right|_{\max} = (0.1\alpha_{PM})/(2\sigma k^3 c_g) \tag{2.5.35}$$

The limiter on WAM4.5 is

$$\left|\Delta N(\sigma,\theta)\right|_{\max} = (2\pi)^2 \times 3.0\times 10^{-7} g u_* \sigma_c \Delta t/(\sigma^3 k) \tag{2.5.36}$$

Instead of Eq.(2.5.35), Lalbeharry et al. applied Eq.(2.5.36) to SWAN. In the study, the modified limiter and the shift growth parameter is employed to improve the accuracy of the significant wave heights.

2.6. Coupling process

For the tide and storm surge simulation, the storm surge prediction is employed for the depth integrated equations, while SWAN is used for wave prediction. The typhoon model is included in the coupling model. A main coupling model is composed of the same number of sub coupling models with the number of domains used in the computation. For example, if the four computational domains from the ocean to coast region are used for the simulation, the framework of the main coupling model is composed of four sub-coupling models. Each sub-model successively runs from the coarse to fine grid by paralleling them using MPI (Message Passing Interface) developed by Argonne National Laboratory on Windows platform. The size ratio of the fine to coarse grid maintains 1/2 or 1/3 to minimize the interpolation error (Kowalik 1993).

2.6.1. Transfer of components

A domain of a storm surge model is piled up on one of wave model (SWAN) for a sub-coupling model. Fig. 2.5 depicts the scheme of the transfer for components in a coupling model. All components of wave parameters on a grid of SWAN are defined at the point of D on a grid. The currents in x and y direction are imposed at the point U and V on a grid, while the water level is defined at the point of η as shown in Fig. 2.5. The components defined by (i, j) on a grid of the storm surge model correspond to the wave parameters defined by (i, j) on a grid of the wave model. In the computation, the component of the water level, η, is directly transferred to $D_{i,j}$ on the grid of SWAN. On the other hand, the averaged current of $U_{i-1,j}$ and $U_{i,j}$ in x direction is linearly interpolated to $D_{i,j}$ on the grid of SWAN. The averaged current of $U_{i,j-1}$ and $U_{i,j}$ in y direction is linearly transferred to $D_{i,j}$ as well. For SWAN, the averaged wave dependent drag coefficient and the force induced by the radiation stress in $D_{i,j}$ and $D_{i+1,j}$ are linearly interpolated to the position of $U_{i,j}$ on the grid in the storm surge model. As described above, the averaged values of $D_{i,j}$ and $D_{i,j+1}$ are linearly transferred to the position of $V_{i,j}$ on the grid. Finally, the wind speeds in x and y direction are defined at η and D on each grid of the storm surge and wave model.

2.6.2. Framework of coupling model

The framework of the coupling model is composed of a main coupling model including sub-coupling models. A sub-coupling model consists of a wave model and a storm surge model. For example, if four domains are used in the computation, a main coupling model is constituted by four sub-coupling models. The first sub-coupling model outputs the water level or wave spectrum for the boundary of the second sub-coupling model. The second sub-coupling model conducts the computation using the values of the first sub-coupling model. After the process is continued by the final sub-coupling model, the first sub-coupling model repeats the computation. The coupling process of a main coupling model composed of K_i sub-coupling model of i=1 to N shown in Fig. 2.6 is as follows:

(1) Storm surge/tide models preliminary compute tides from domain 1 to N.
(2) The wave model in the k_1 sub-coupling model runs under currents and water level of the same sub-coupling model to obtain waves. The wave model in the k_2 sub-coupling model conducts the computation with open boundary values obtained from the k_1 sub-coupling model and currents and water level of the k_2 sub-coupling model. The process repeats by the K_N sub-coupling model.

(3) New wind stress and radiation stress of each wave model in each K_i sub-model are given to each corresponding storm surge model at the next time step.

(4) The storm surge model in the k_1 sub-coupling model is run by the wind stress and the radiation stress of the k_1 sub-coupling model. The storm surge model in the k_2 sub-coupling model carries out the computation using the water level imposed on open boundaries by the k_1 sub-coupling model, and the wind stress and radiation stress of the k_2 sub-model. The process repeats from the k_1 to k_N sub-coupling model.

(5) New currents and water surface elevation obtained from each storm surge model in each k_i sub-coupling model are transferred to each corresponding wave model at the next time step.

(6) The processes from (2) to (5) are repeated during the computation.

The typhoon model included in the storm surge model provides the wind components to the storm surge model at the same interval with its time step, but to the wave model at the same interval with the exchange of the data. The atmospheric pressure is only provided to the storm surge at the same time step of the storm surge model.

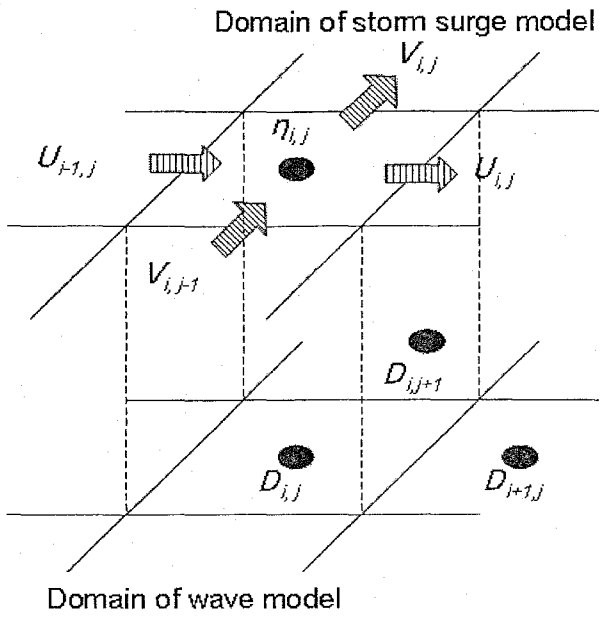

Fig. 2.5. The scheme of transfer for components in a coupling model.

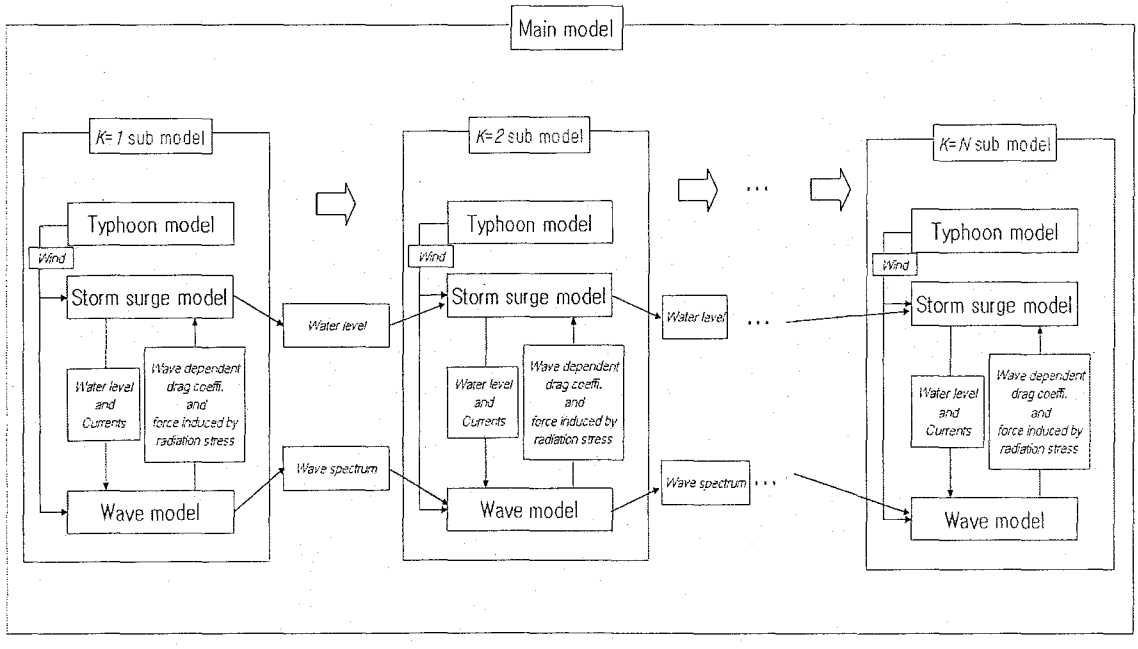

Fig. 2 6. The framework of the main coupling model.

Chapter 3

Effect of tidal magnitude in simplified sea region

Flather (1994) showed that the timing of cyclone landfall and its coincidence with high tide determine the area worst affected by flooding. In addition, he showed that the differences in track and tidal conditions are to be important in a large area of the southern delta in 1970 and along the mainland coast south of Chittagong in 1990 by the comparison with two cyclones. Hence, he carried out the computation of the storm surge using two cyclones in a large coastal region of the Bay of Bangal. In this chapter 3, the computation of the storm surge is, however, conducted in the simplified sea region using the simplified wind field in order to investigate the behavior and the magnitude of the storm surge due to the variation of various tidal phases and amplitudes in the ideal sea area.

3.1. Model description

The coupling model described at Chapter 2 is used to carry out the numerical experiment in the idealized sea region. The simplified wind and bathymetry are used, so that the coupling model is slightly modified for the simplification on the storm surge model. The time to exchange the data between the storm surge and the wave model is chosen 100 seconds. The time steps of 5 seconds and 100 seconds are employed for the storm surge and SWAN model, respectively.

The depth-integrated, nonlinear shallow water equations described at Chapter 2 are modified by

$$\frac{\partial \eta}{\partial t}+\frac{\partial M}{\partial x}+\frac{\partial N}{\partial y}=0 \tag{3.1.1}$$

$$\frac{\partial M}{\partial t}+\frac{\partial}{\partial x}\left(\frac{M^2}{d}\right)+\frac{\partial}{\partial y}\left(\frac{MN}{d}\right)+gd\frac{\partial \eta}{\partial x}=\frac{1}{\rho}\left(\tau_s^x-\tau_b^x+F_x\right)+A_h\left(\frac{\partial^2 M}{\partial x^2}+\frac{\partial^2 N}{\partial x^2}\right) \tag{3.1.2}$$

$$\frac{\partial N}{\partial t}+\frac{\partial}{\partial x}\left(\frac{NM}{d}\right)+\frac{\partial}{\partial y}\left(\frac{N^2}{d}\right)+gd\frac{\partial \eta}{\partial y}=\frac{1}{\rho}\left(\tau_s^y-\tau_b^y+F_y\right)+A_h\left(\frac{\partial^2 M}{\partial y^2}+\frac{\partial^2 N}{\partial y^2}\right) \tag{3.1.3}$$

where, η = the sea surface fluctuation, M and N = the depth integrated currents in the x and y directions, g = the gravitational acceleration, $d=\eta+h$ = the total depth, A_h = the horizontal eddy diffusion and ρ = the density of water. F_x and F_y represent the components of the wave induced force which are the function of the radiation stress in x and y directions. In the section 2.3, these were explained in details. The gradient of atmospheric pressure is ignored, because the function of the atmospheric pressure in the momentum equation is independent on the depth. It can be explained that the depression of 1hPa is approximately equal to $1cm$. The Coriolis force is also negligible in the small region.

The disturbed water surface at an open boundary to represent the sinusoidal tide is given by

$$\eta=A\sin\left(\frac{2\pi}{T}t\right) \tag{3.1.4}$$

in which A represents the amplitude of water surface, T the period of 12 hours, t the time step in the computation.

A third-generation numerical wave model (SWAN) is used to compute the radiation stress and wind drag coefficient. SWAN version 40.41 is employed to the coupling model. That is, the original limiter described by Ris (1997) is implemented instead of that modified by Lalbeharry (2004) described at 2.5.4.

3.2. Numerical experiment

The numerical experiment is carried out to examine the effect of the large tidal variation on the storm surge using the simplified wind distribution and bathymetries. Table 3.1 shows the

computational conditions for the experiments. The amplitudes of the tides are chosen as 0.5, 1.0, 2.0 and 3.0m. An illustration denotes the timing at the generation of the maximum storm surge along the tidal phase. For example, in the case of *mcb*, the maximum storm surge occurs at the moment when the tidal phase crosses the mean water level from the low to high tide. Hence, the storm surge on the low tide starts to generate, grow up and approach the maximum storm surge, at the mean water level. After its peak, it starts to decrease and disappear on the high tide. In the case of *crest*, the peak of the storm surge occurs on the crest of the spring tide. For *cb*, one generates in the middle between *mcb* and *crest*. For *mca*, one takes place when the tidal phase crosses the mean water level from the high to low tide. One occurs in the middle between *crest* and *mca* in the case of *ca*. For *trough*, one simultaneously coincides with the trough with the neap tide. Hence, *tb* and *ta* mean that one occurs in the middle between *mca* and *trough*, and *trough* and *mcb*, respectively. The interval between *mcb* and *cb* is 1 hour 30 minutes during a period of 12 hours. In addition, the coupling model represents the storm surge computation with the tide, while the non-coupling model represents the computation on the still water level.

The storm surge induced by the combination of the wind stress, the atmospheric pressure and the radiation stress for the coupling model is evaluated by

$$\eta_{st} = \eta_{tide+ws+rs} - \eta_{tide} \tag{3.1.5}$$

where *st* represents the storm surge, *ws*; the wind stress, *rs*; the radiation stress. For the non-coupling model, the storm surge on the still water level is represented by

$$\eta_{st} = \eta_{ws+rs} \tag{3.1.6}$$

For the coupling model, the set-up induced by the radiation stress is evaluated by

$$\eta_{rs} = \eta_{tide+ws+rs} - \eta_{tide+ws} \tag{3.1.7}$$

For the non-coupling model on the still water level, one is computed by

$$\eta_{rs} = \eta_{ws+rs} - \eta_{ws} \cdot \tag{3.1.8}$$

In order to compute the maximum water level of the non-coupling model, the tidal level is

linearly added to Eq. (3.1.6)

$$\eta_{wl}(t) = \eta_{ws+rs}(t) + \eta_{tide}(t) \tag{3.1.9}$$

where *wl* represents the water level., t; time.

Here, the terminology should be defined to avoid the confusion as follows:

Coupling model (CR): the computation with the tide.
Non-coupling model (NCR): the computation without the tide.
Storm surge: the surge induced by the combination of the wind stress and radiation stress.
Set-up: the surge induced by the only radiation stress.
Maximum storm surge (MSW): the peak of the storm surge induced by the combination of the wind and the radiation stress.
Maximum set-up (MSR): the peak of the surge induced by the only radiation stress.
Maximum sea surface level (MSSL): the maximum water level induced by the combination of the wind and the radiation stress.

From now on, the terminology described above will be used to describe the result of the computation. For exampled, MSR-NCR refers to the maximum set-up induced by the radiation stress in the non-coupling model. Then, MSW-CR is evaluated by Eq. (3.1.5), MSR-CR; Eq. (3.1.7), MSW-NCR; Eq. (3.1.6), MSR-NCR; (Eq. 3.1.8), MSSL-CR; $\eta_{tide+ws+rs}$ and MSSL-NCR; η_{ws+rs}.

Table 3. 1. Experimental cases of tidal amplitudes and phases encountering the maximum storm surge.

Tidal phase at the maximum storm surge	Tidal amplitude (m)	Case
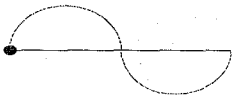	0.5m	mcb
	1.0m	
	2.0m	
	3.0m	
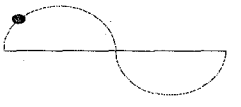	0.5m	cb
	1.0m	
	2.0m	
	3.0m	
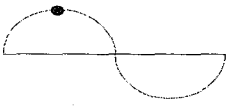	0.5m	crest
	1.0m	
	2.0m	
	3.0m	
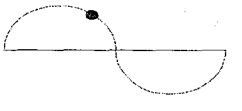	0.5m	ca
	1.0m	
	2.0m	
	3.0m	
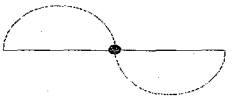	0.5m	mca
	1.0m	
	2.0m	
	3.0m	
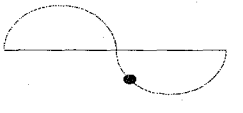	0.5m	tb
	1.0m	
	2.0m	
	3.0m	
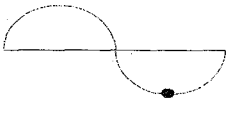	0.5m	trough
	1.0m	
	2.0m	
	3.0m	
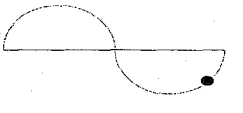	0.5m	ta
	1.0m	
	2.0m	
	3.0m	

3.2.1. Wind profile and bathymetry

The horizontal distribution of wind in a typhoon depicts the asymmetric circle centering its eye. Its wind blows into its center with the anti-clockwise rotation, because the pressure is low at the center of the typhoon, but high around its center. The observed wind direction is dependent on the track of a typhoon. The wind observed at a station of a ground near a coast, which is located in the right side of its track, tends to blow from the sea to the land during the storm event. The wind direction might be opposite at a station on the left side of its track. In general, the higher storm surge level occurs in the case of the former. Therefore, it is assumed that the wind direction is constant from the sea to land for the simplification of the analysis in the study.

The wind speed profile prescribed by Gaussian distribution is followed by

$$W_x = \frac{\alpha}{\sigma\sqrt{2\pi}} \exp\left(\frac{(x-\mu)^2}{2\sigma^2}\right) \tag{3.1.10}$$

$$W_y = 0 \tag{3.1.11}$$

where σ is 0.4 and α represents the maximum wind speed of 40 m/s for 6 hours. The simplified bathymetry which is the equilibrium sea bottom profile (Dean and Dalrymple 2002) is depicted by

$$h = -\varepsilon x^{2/3} \tag{3.1.12}$$

in which ε is the bottom slope, x the distance from the shore line at the cross profile. For the part of the land, $h = \varepsilon x^{2/3}$ yields the ground level.

Figure 3.1 and 3.2 show the cross shore profiles of four bathymetries with ε = 0.2, 0.1, 0.05 and 0.01. The mean water level, the spring tidal level of 3.0m and the neap tidal level of -3.0m are depicted in Fig. 3.1.The bottom slopes of (a) and (b) are steep, while those of (c) and (d) are gentle. The tidal flat will be widely exposed at (c) and (d), because of the very gentle slope and shallow depth. The part represented by the negative distance means the land, on the other side, the rest denotes the sea. Table 3.2 shows bottom slopes, grid sizes and domains used in the computation. The nested scheme is applied to the numerical experiment using four domains. The grid sizes are changeable in the x direction, but constant in the y direction. The grid sizes in x direction are decreased from 2700m in the domain 1 to 30m in the domain 4 as maintaining the

ratio of 1/3 of the fine grid size to coarse one. The number of grids in all domains is 100×100. Fig. 3.3 shows the computation grid of domain 1 to 4. The wind blows from the offshore to the onshore. The storm surge and water level in the computation will be observed at the point of 150m far from the shoreline in the domain 4 as shown in Fig. 3.1. The water depths at each observation point were 8.96, 4.48, 2.24 and 0.75m for $\varepsilon = 0.2$, 0.1, 0.05 and 0.01, respectively.

3.3. Result in simulation

Storm surges were computed during the wind event on simplified slopes based on Table. 3.1. First, the computation of the only tide was conducted for 48 hours to achieve the steady state. After distributing the tide sufficiently, the computation of the storm surge was carried out to obtain $\eta_{tide+ws+rs}$ in Eq. (3.1.5). Alternatively, the computation of the only tide, η_{tide}, was carried out so as to evaluate the storm surge represented by η_{st} of Eq. (3.1.5). In the section 3.3.1, The result of the computation at the observation point will be explained in the case of the tidal amplitude of 3.0m and the tidal phase of *crest*. In the section 3.3.2, the result of the computation for the spatial distributions and the cross profiles will be described in the same case with the section 3.3.1.

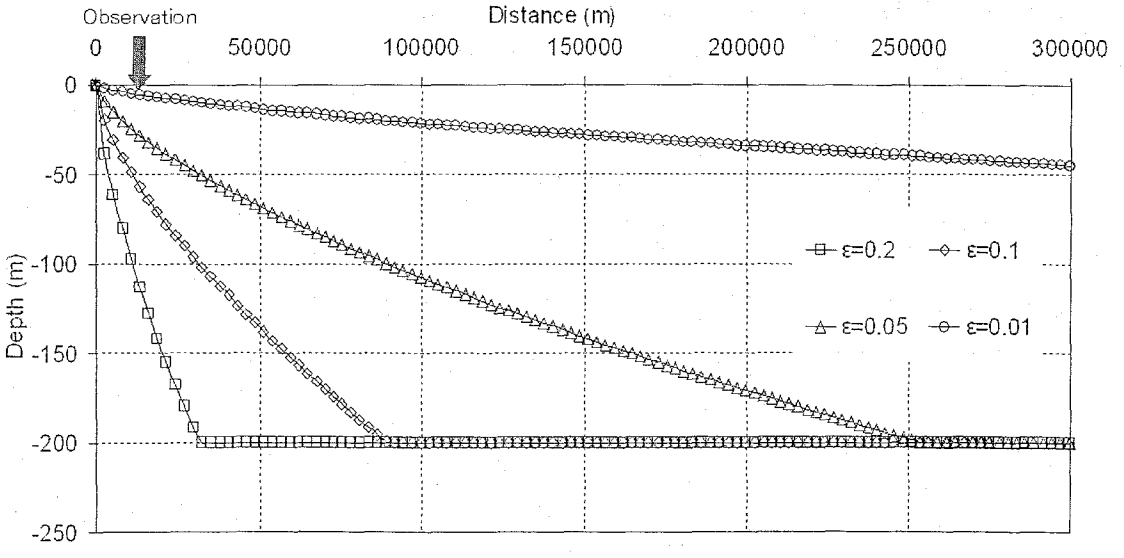

Fig. 3.1. The bottom slope by 300,000m.

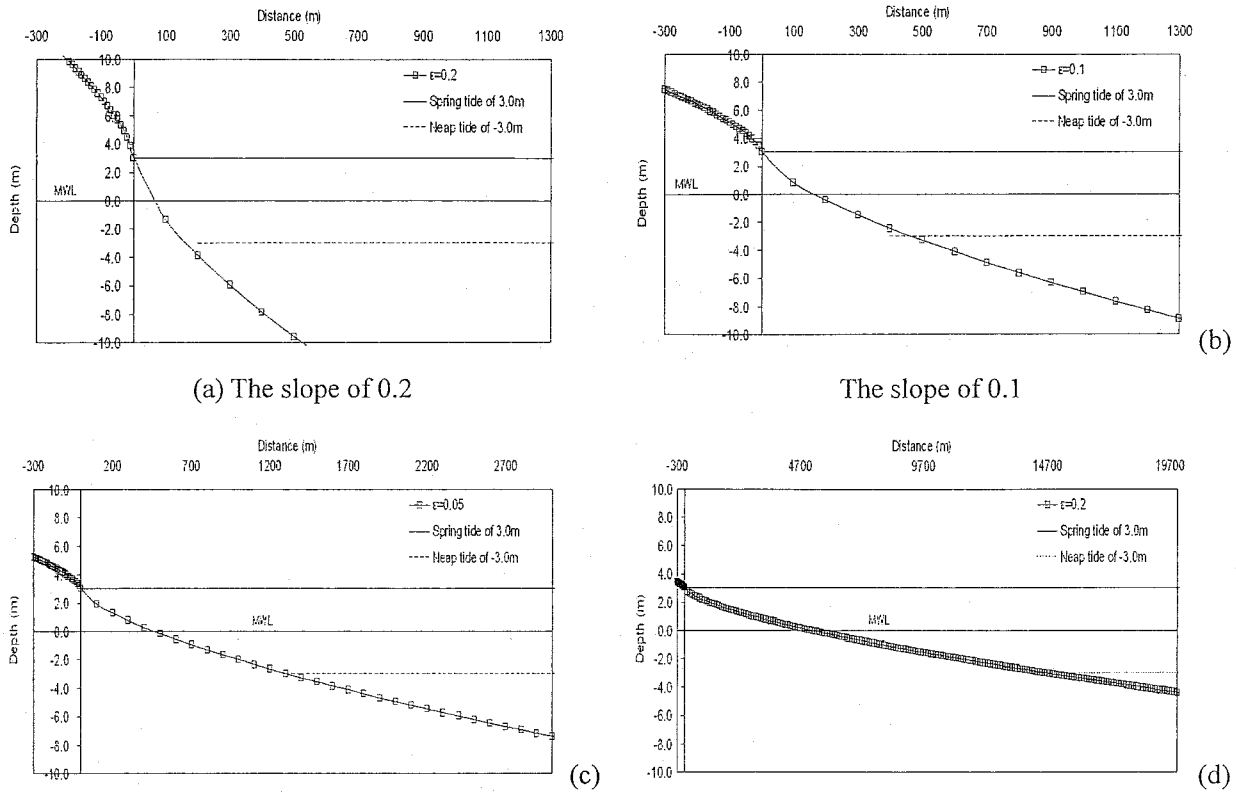

Fig. 3.2. Cross-shore profiles on the slopes of 0.2, 0.1, 0.05 and 0.01 with the mean water level (MWL), the spring tide (the amplitude; 3.0m) and the neap tide (the amplitude; -3.0m).

Table 3. 2. Domains used in the study.

Slope	Domain No.	Grid size (m)	Num. of grid
0.2	1	2700×1000	100×100
0.1	2	900×1000	100×100
0.05	3	300×1000	100×100
0.01	4	30×1000	100×100

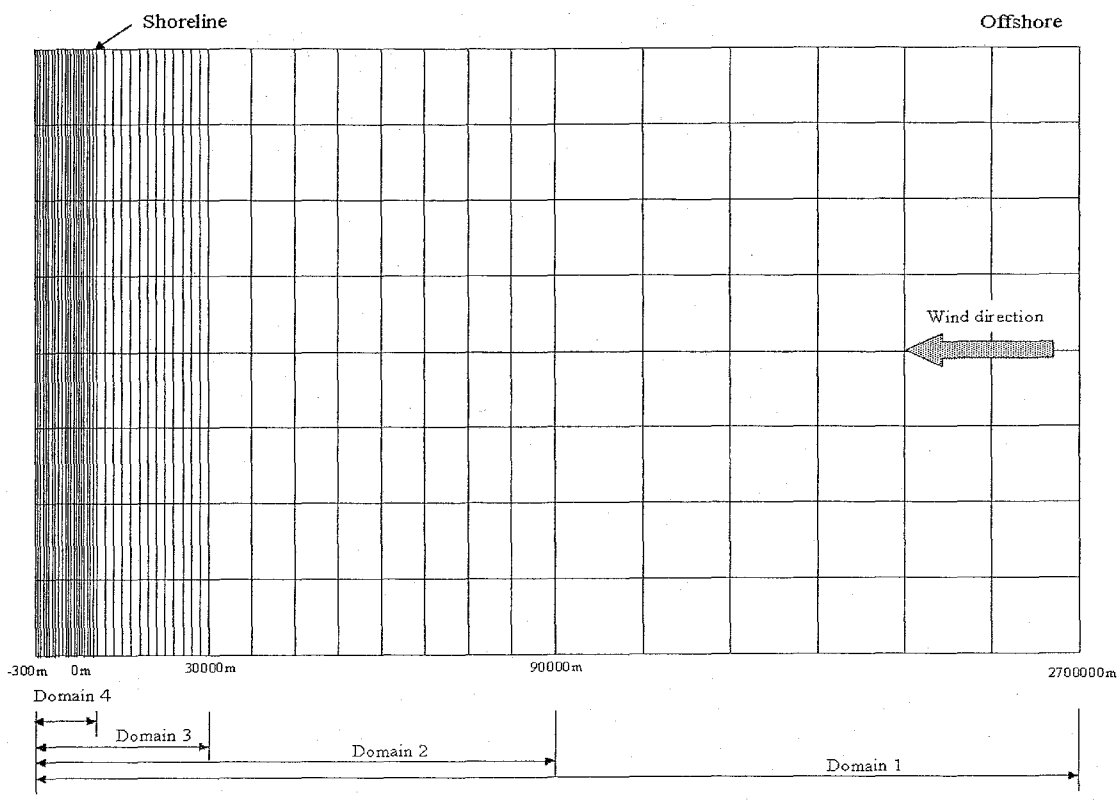

Fig. 3.3. Computational domains and wind direction.

3.3.1. Time histories

Figure 3.4 depicts one of experimental results at the observation point, when the maximum storm surge (MSW) encountered the crest of the tidal phase and the tidal amplitude of 3.0m on the slope of 0.1. It is shown that the wind speed produced by Eq. (3.1.10) blew during the wind event of approximately 6 hours. Hence, the storm surge started to generate at 55 hours and then, the peak of the storm surge occurred around 58 hours when the wind speed was the maximum. After 58 hours, the wind speed decreased and the storm surge also started to be reduced. The storm surge was also computed on the still water level and its peak was evaluated as 0.85m. Fig. 3.5 shows the time series of the water levels computed by the coupling model (CR) at the observation point under the same tidal condition with Fig. 3.4. The water depths were 8.96, 4.48, 2.24 and 0.75m for ε = 0.2, 0.1, 0.05 and 0.01, respectively. The highest water level occurred in the case of ε = 0.01, while the lowest water level occurred in the slope of 0.2. Therefore, it was expected that the magnitude of the rise in the water level became lager, when the water depth was shallow and the bottom slope was gentle. It was also confirmed that the tidal flats were exposed on the slope of 0.01 and 0.05 when the tidal phase was on the neap tide in the case of the tidal amplitude of 3.0m, because the water depths were very shallow. Fig. 3.6

describes the storm surges computed by the non-coupling model (NCR), that is, without the tide at the same point with Fig. 3.4. The magnitudes of the storm surges induced by the wind were approximately 0.8m and showed the similar heights in the case of the slope of 0.2, 0.1 and 0.05, while it was the largest storm surge in the slope of 0.01. Therefore, the magnitude of the storm surge on the slope of 0.01 became larger than those on the slope of 0.2 and 0.1 and 0.05, because the water depth of 0.75m on the slope of 0.01 was very shallow compared to the others.

Figure 3.7 shows significant wave heights computed by CR during the wind event under the same tidal condition with Fig. 3.4. The significant wave height of 6m approached to the shoreline on the slope of 0.2, while that of about 2 m propagated on the slope of 0.01. The peak of the significant wave height became higher, when the bottom slope was steeper. The time of the generation in the maximum significant wave height indicated around 58 hours when the peak in the storm surge occurred. Figs. 3.8 and 3.9 show time histories of the set-ups yielded by Eq. (3.1.7) in the case of *crest* and the tidal amplitude of 3.0m, and Eq. (3.1.8) on the still water level. The magnitude of the set-up on each slope was computed as less than 0.05 by the coupling model, while as more than 0.05m by the non-coupling model except in the slope of 0.01.

The timings of the generations in the maximum set-ups on all slopes were different each other. The maximum set-ups computed by the coupling model on the slopes of 0.1 and 0.05 occurred around 58 hours, while the set-ups on the slopes of 0.2 and 0.01 was not the maximum at the same time as shown in Fig. 3.8.

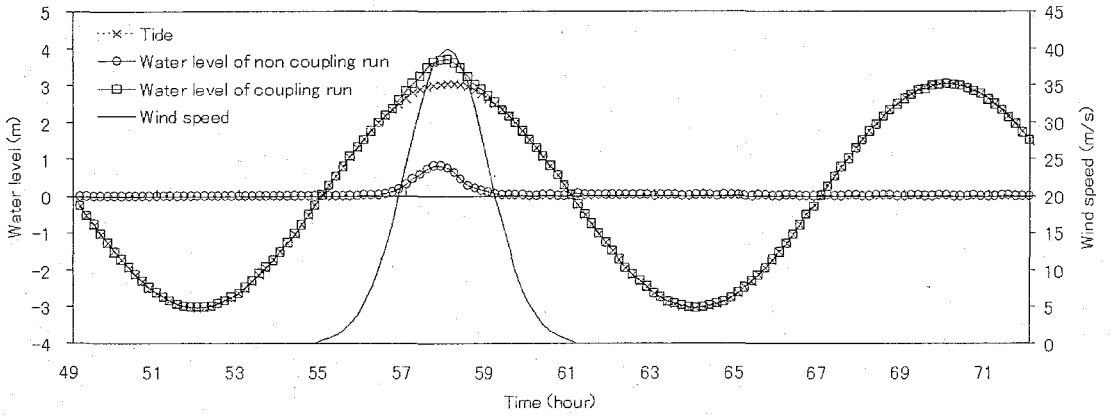

Fig. 3.4. Time series of the wind speed, tide and water levels of NCR and CR at the observation point, when the MSW encounters the crest of the tidal phase (The slope; 0.1, the tidal amplitude; 3.0m, the tidal phase; crest).

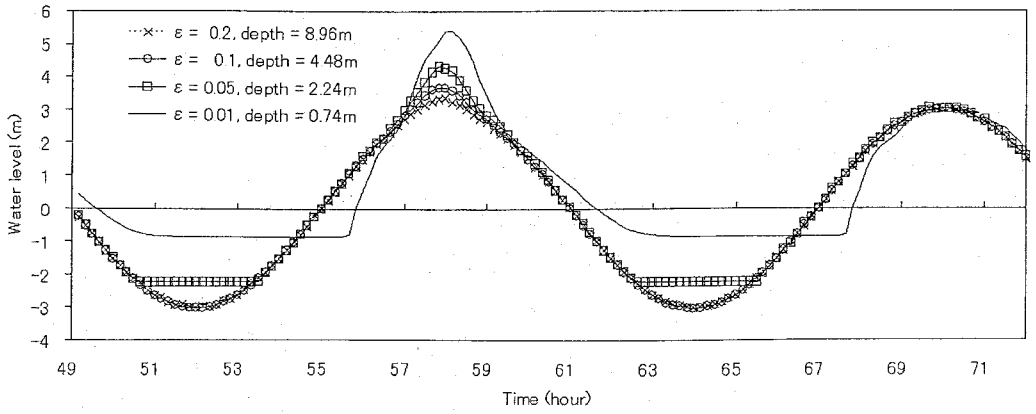

Fig. 3.5. Time series of water levels computed by CR at the observation point, when the MSW encounters the crest of the tidal phase (The tidal amplitude; 3.0m, the tidal phase; crest).

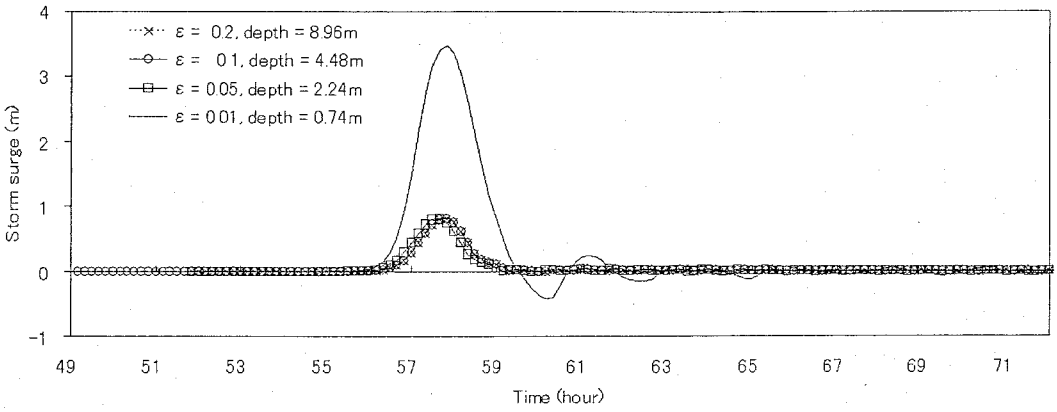

Fig. 3.6. Time series of the storm surges on the still water level computed by the non-coupling model at the observation point.

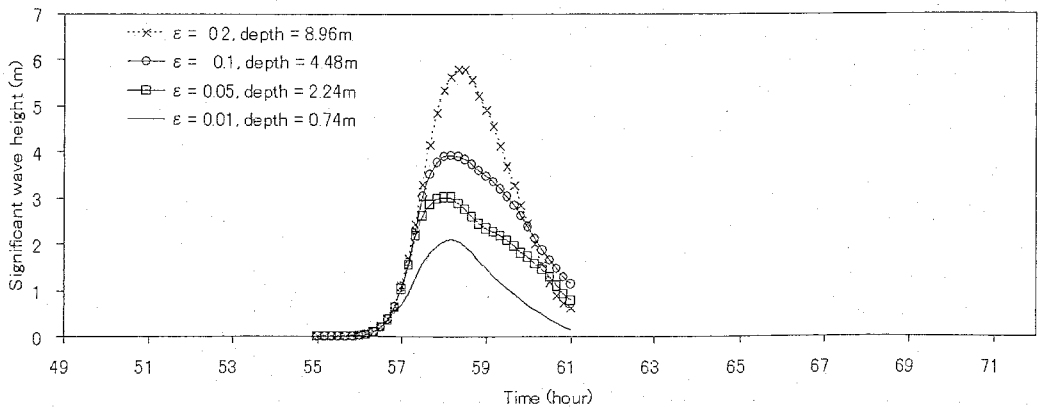

Fig. 3.7. Time series of the significant wave heights computed by CR at observation point (The tidal amplitude: 3.0m, the tidal phase: *crest*).

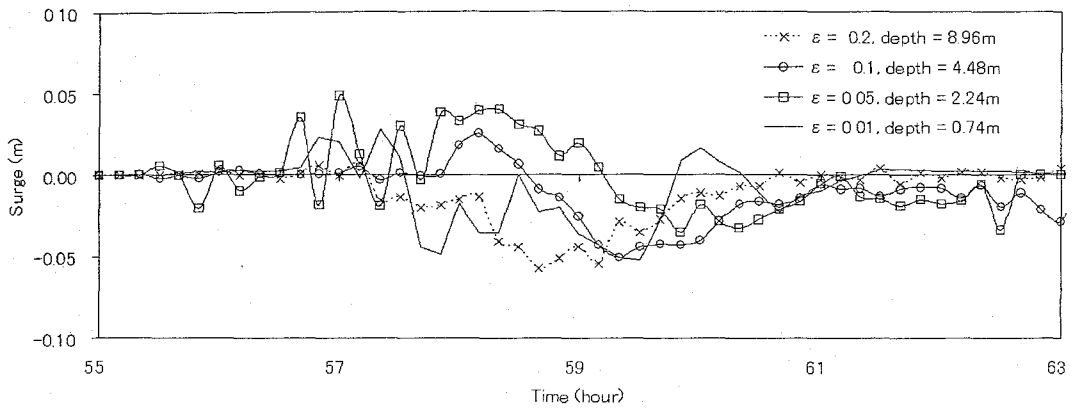

Fig. 3.8. Time histories of the set-ups induced by the radiation stress computed by CR at the observation point (The tidal amplitude: 3.0m, the tidal phase: crest).

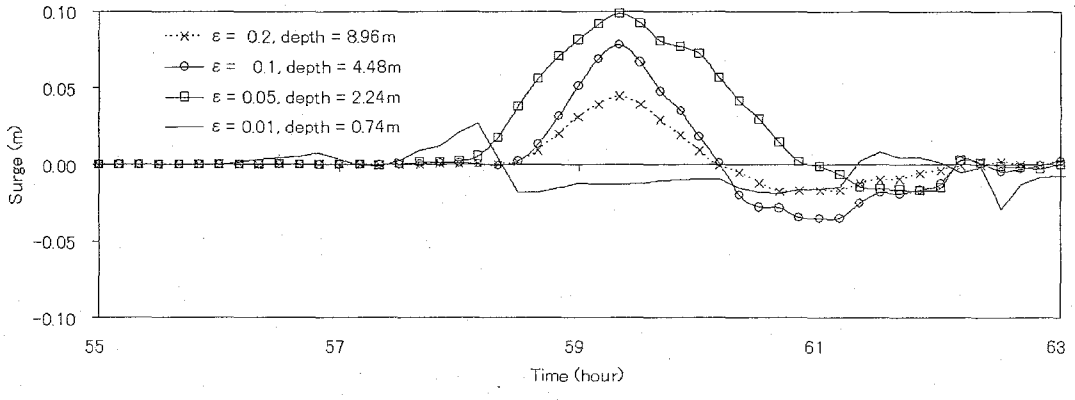

Fig. 3.9. Time histories of the set-ups induced by the radiation stress computed by NCR at the observation point.

The magnitudes of the set-ups computed by the non-coupling model on the slopes of 0.2, 0.1 and 0.05 were the maximum after 59 hours, its maximum on the slope of 0.01 occurred before 59 hours. The highest surge occurred on the slope of 0.05, while the lowest surge occurred on the slope of 0.01. It was expected that the various bottom slopes and the tidal variation caused the change of the magnitude and the generation timing in the set-up.

3.3.2. Spatial distribution and cross profile

Figure 3.10 represents the horizontal distribution of the maximum wind velocity with about 40 m/s in the domain 4 at 58 hours. As mentioned in Eqs. (3.1.10) and (3.1.11), the wind component in x direction was only considered so as to simplify the computation condition, but the wind speed in y direction was assumed as the zero. In addition, the wind component in

alongshore direction was constant.

Figure 3.11 shows the horizontal distribution of the maximum water level which was computed by the coupling model at 58 hours in the domain 4 of $\varepsilon = 0.01$ in the case of tidal amplitude of 3.0m and the tidal phase of *crest*. The gradually increased water levels were distributed from 4.5 to 5.0m on the sea surface. Hence, from the Fig.3.12, it was expected that the storm surge computed by the coupling model (MSW-CR) occurred more than 2.2m at 58 hours at the observation point under the condition of the slope of 0.01, the tidal amplitude of 3.0m and the tidal phase of *crest*. Fig. 3.13 show the horizontal distribution of the maximum storm surge computed by the non-coupling model (MSW-NCR) which generated more than 2.7m at 58 hours at the observation point under the same condition with Fig. 3.12. In the part of the sea, MSW-CR was lower than MSW-NCR. That is to say, the maximum storm surge computed by the coupling model became lower than that calculated by the non-coupling model at the observation point. However, MSW-CR was higher than MSW-NCR in the part of the land. The reason was that the storm surge coinciding with the spring tide of 3.0m ran up the land for MSW-NCR, on the other hand, it was not able to sufficiently up the land on the still water level for MSW-NCR.

Figure 3.14 depicts the horizontal distribution of the significant wave height which was computed by the coupling model in the domain 4 at 58 hours under the same computational condition with Fig. 3.10. Waves generated by the wind were developed from the offshore and propagated to the onshore. After experiencing the bottom friction, they broke in front of the shoreline. The significant wave height of about 3.0m on the offshore propagated to the onshore and started to break near 600m and then, that of about 1.0m approached to the shoreline. Fig. 3.15 shows the horizontal distribution of the significant wave height which was calculated by the non-coupling model on the still water level under the same domain and condition with Fig. 3.14. The peak of the significant wave height computed by the non-coupling model was about 3.5m, but 3.9m evaluated by the coupling model.

Figure 3.16 shows the comparisons of the cross profiles between the storm surge computed by CR and NCR at 58 hours on each slope, when the case of the tidal phase is *crest* and the tidal amplitude is 3.0m. MSW-CRs were generally smaller than MSW-NCR near the shoreline.

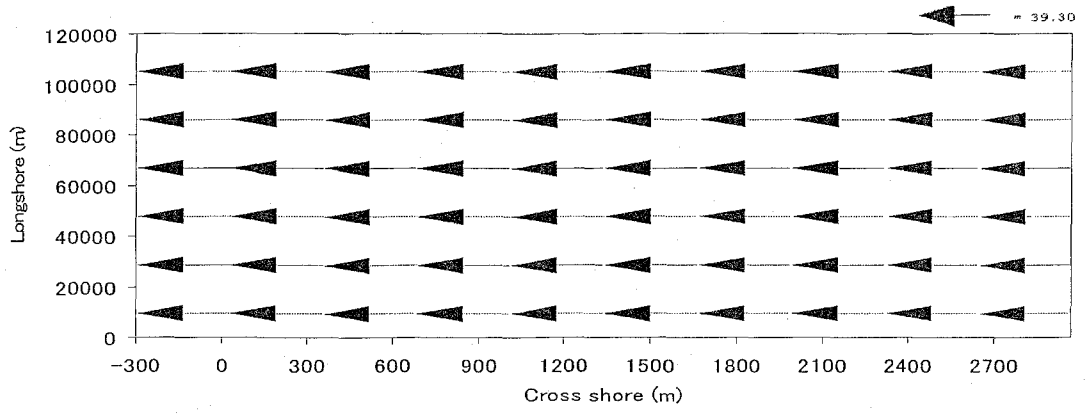

Fig. 3.10. The horizontal distribution of the maximum wind velocity in the domain 4 at 58 hours

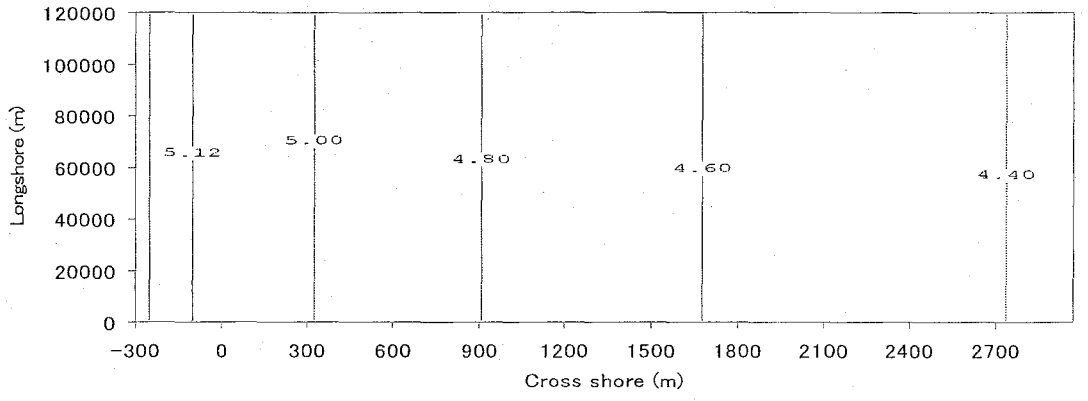

Fig. 3.11. The horizontal distribution of the maximum water level computed by CR at 58 hours in the domain 4 (The slope; 0.01, the tidal amplitude; 3.0m, the tidal phase; *crest*).

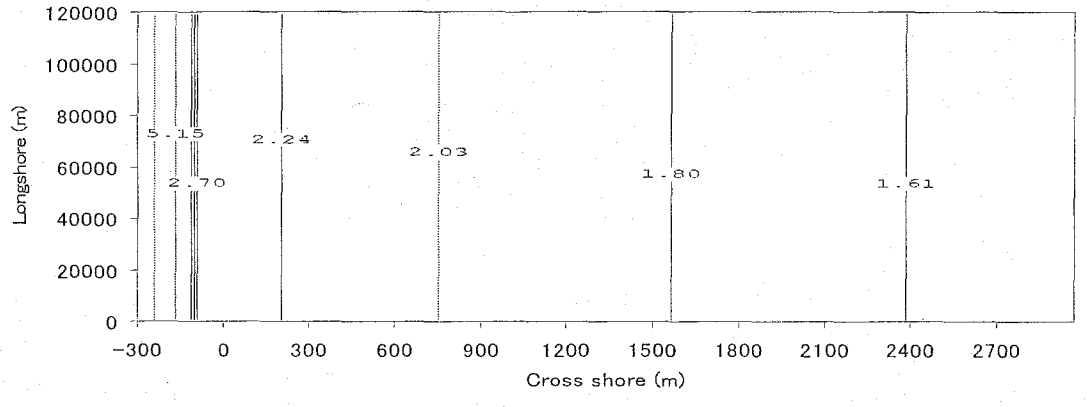

Fig. 3.12. The horizontal distribution of MSW-CR in the domain 4 at 58 hours (The slope; 0.01, the tidal amplitude; 3.0m, the tidal phase; *crest*).

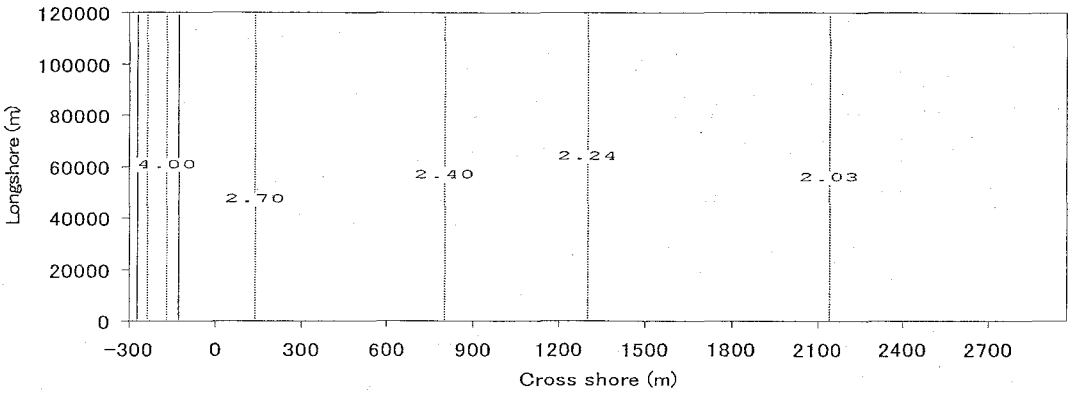

Fig. 3.13. The horizontal distribution of MSW-NCR in the domain 4 at 58 hours (The slope; 0.01, the tidal amplitude; 3.0m, the tidal phase; *crest*).

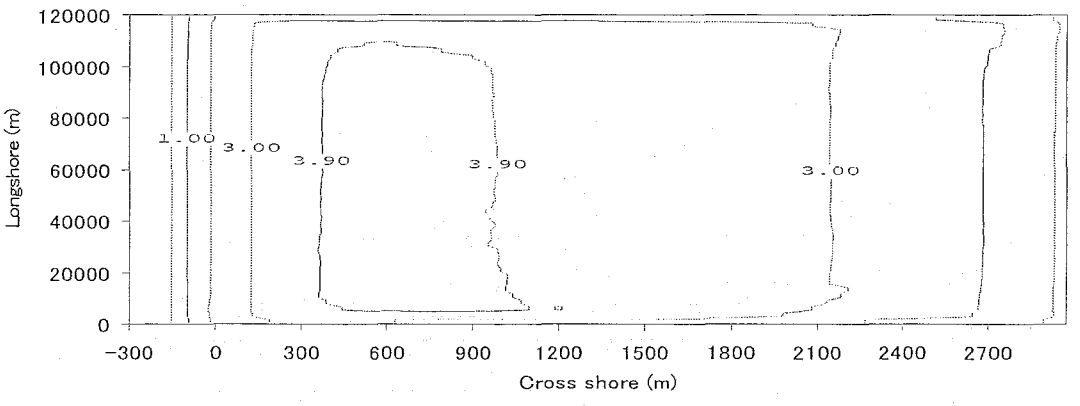

Fig. 3.14. The horizontal distribution of the significant wave height in the domain 4 at 58 hours (The slope; 0.1, the tidal amplitude; 3.0m, the tidal phase; *crest*).

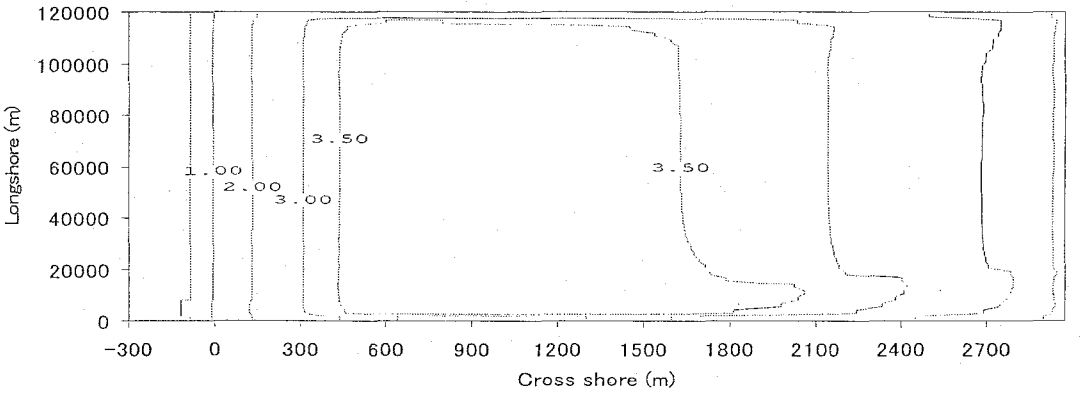

Fig. 3.15. The horizontal distribution of the significant wave height on the still water level in the domain 4 at 58 hours (The slope; 0.1, the tidal amplitude; 3.0m).

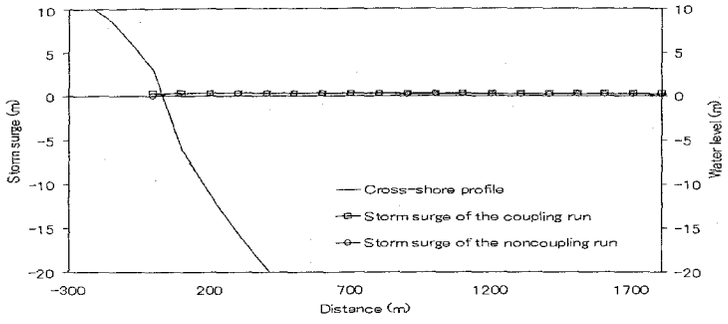

(a) The slope of 0.2

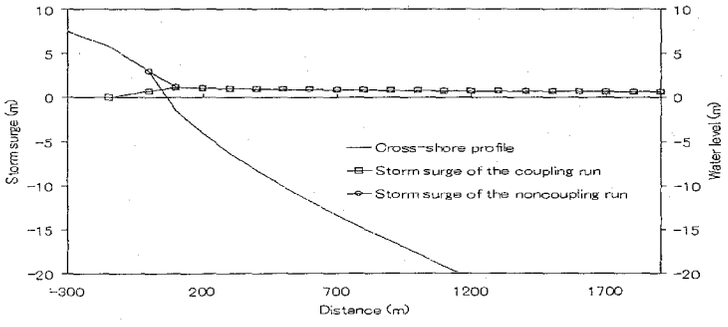

(b) The slope of 0.1

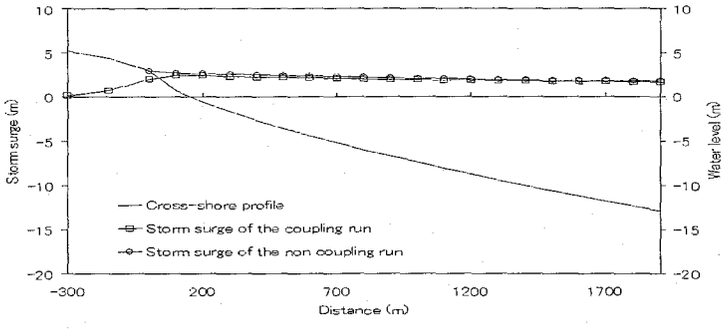

(c) The slope of 0.05

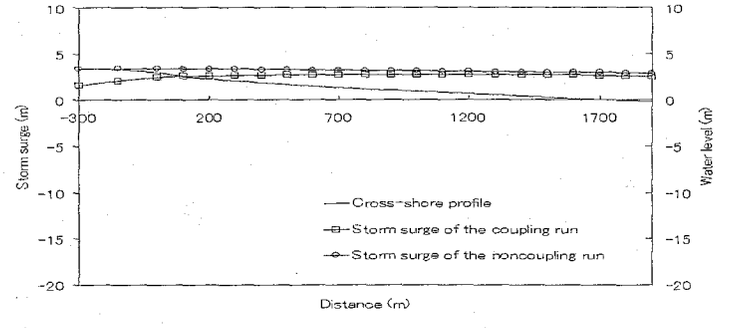

(d) The slope of 0.01

Fig. 3.16. The comparisons of cross profiles between the storm surge computed by CR and NCR on each slope at 58 hours, when the maximum storm surge occurred (The tidal amplitude; 3.0m, the tidal phase; *crest*).

3.4. Discussion

In the previous section 3.3, the numerical conditions in the experiments were described in details and one of results was briefly explained in the case of *crest* and the tidal amplitude of 3.0m on the slope of 0.01. From the result of *crest*, it was convinced that the bottom slope and tidal variation caused the change of the magnitude in the water level induced by the wind. From now on, in this section 3.4, MSW-CR, MSR-CR and MSSL-CR will be compared with MSW-NCR, MSR-NCR and MSSL-NCR in respect to the tidal variation and the bottom slope. In addition, the result of the numerical experiment will be discussed in order to understand how the large tidal variation influences on the storm surge associated with the maximum magnitude of the disturbed sea surface due to the wind. Note that the water depths of the observation points were 8.96 4.48, 2.24 and 0.75m for each slope of 0.2, 0.1, 0.05 and 0.01, respectively. The terminology defined at previous section 3.2 will be continuously used in this section.

3.4.1. Effect of tide on storm surge

Figure 3.17 shows the comparison of the variation of MSWs that was occurred at each tidal amplitude and slope associated with the tidal phase. An illustration makes you understand the timing of the generation in the maximum storm surge encountering each tidal phase. From now on, the magnitudes of MSWs for all cases will be explained individually. The magnitude of MSW-NCR on each slope of 0.2, 0.1, 0.05 and 0.01 generated as 0.4, 0.8, 1.5 and 3.5m, respectively. In the case of (a) *mcb*, MSW-CR generated coinciding with the tidal phase crossing the mean water level from the low to high tide. The variation of the magnitudes of MSW-CRs on the slopes of 0.2, 0.1 and 0.05 were similar to those of MSW-NCRs when the tidal amplitude increases. On the contrary, the magnitude of MSW on the slope of 0.01 was irregularly decreased as increasing the tidal amplitude. The magnitude of MSW for *2.0m* (the tidal amplitude in the transverse axis in Fig. 3.17) increased, but for *3.0m* decreased compared to the magnitude of MSW-NCR. In the case of (b) *cb*, the magnitudes of MSW-CRs did not significantly vary yet on the slope of 0.2, 0.1 and 0.05, but slightly decreased as increasing the tidal amplitude. However, for the slope of 0.01 MSW-CRs significantly decreased, then the difference of the magnitude between MSW-CRs in the case of. *3.0m* and *no tide* (computed by the non-coupling model in the transverse axis) as more than 1.2m. The patterns of the variation in MSW-CRs on all slopes for *crest* were similar to those for (b) *cb*. The magnitudes of MSW-CRs in the case of (c) *crest* were slightly changed on the slopes of 0.2, 0.1 and 0.05, while the magnitude of MSW-CR in (c) *crest* was significantly changed on the slope of 0.01 such as *cb*. For *ca*, the patterns of variation in MSW-CRs were similar to (c) *crest*. However, the

variation of the magnitude in MSW-CRs on the slope of 0.01 in (d) *ca* became smaller than that in (c) *crest*. In the case of (e) *mca,* the variations of the magnitudes in MSW-CRs seemed to be constant at all cases. In the cases of (f) *tb*, (g) *trough* and (h) *ta*, the changes of the magnitudes in MSW-CRs seemed to be insignificant on the slopes of 0.2, 0.1 and 0.05. However, the magnitudes of MSW-CRs on the slope of 0.01 slightly increased from *no tide* to *1.0m* in the transverse axis of (f), (g) and (h), while those decreased from *1.0m* to *3.0m*. In addition, in the case of (g) *trough*, the magnitude of MSW-CR on the slope of 0.05 slightly increased from *0.5m* to *0.2m* in the horizontal axis and then, that decreased at *3.0m*. It was estimated that the bottom slope and the tidal variation caused the phenomenon described above, because the bottom slope was shallow and the tidal flat was exposed when the tidal phase was on the neap tide with the tidal amplitude of 3.0m. For example, the water depths at the observation points on two slopes of 0.01 and 0.05 were 2.24 and 0.75m described previously. On other words, the actual shoreline should move to the offshore when the water level drops below the mean water level. On the other hand, MSW, generated on the tidal phase below the mean water level, was dragged by the wind and approached to the shoreline. As a consequently, the descent of the tidal phase below the mean water level resulted in the reduction of the magnitude in MSW-CR compared to MSW-NCR. However, the variations of the magnitudes in MSW-CR on the slope of 0.2 and 0.1 were insignificant because their bottom slopes were steeper than the others.

Figure 3.18 shows the comparison of the MSW-CRs and –NCRs versus the variation of tidal phase on each slope of 0.2, 0.1, 0.05 and 0.01, respectively. From (a), the difference of the magnitudes between MSW-CR and -NCR was insignificant. Hence, the effect of the large tidal variation was small when the bottom slope was steep. In the case of (b), the variation of the magnitudes in MSW-CRs started to appear on the slope of 0.1 when the tidal amplitude became larger. In the case of (c), the variations of the magnitudes in MSW-CRs were significant as varying the tidal phase in the horizontal axis. It was clear that the magnitudes of MSW-CRs widely changed on the slope of 0.01 in (d) when the tidal phase varied in the transverse axis. In addition, the difference of the magnitudes in between MSW-CRs and -NCR became larger when the tidal amplitude became higer on slopes of 0.05 and 0.01. Finally, for all slopes, the magnitudes of MSW-CRs encountering the tidal phases above the mean water level were smaller than the magnitude of MSW-NCR, while those coinciding the tidal phases below the mean water level were not only larger but also smaller than the magnitude of MSW-NCR.

Evidently, it could be confirmed the variations of the magnitudes in MSW-CRs associated with tidal levels shown in Fig. 3.19 as described at previous paragraph. A horizontal axis means the tidal level yielded by the computation of the only tide. A vertical axis represents the maximum

storm surge level as MSW-CR. The tidal level and the storm surge level are the function of time, it could be, therefore, assumed that both correspond to each other at the same time. For example, the computation of the storm surge is carried out with the tidal amplitude of 1.0m for 100 hours and the maximum storm surge generates at 50 hours. In addition to that, the tidal computation is conducted under the same condition with the computation of the storm surge. From both computations, the maximum storm surge generated at 50 hours in the storm surge simulation corresponds to the tidal level at the same time in the tidal simulation. See Fig. 3.19. The scatter of the magnitudes in MSW-CRs corresponding to the tidal level is precisely divided at the center of the zero tidal level in the case of slope of 0.2, 0.1 and 0.05. The relation of MSW-CR versus the tidal level was found compared to MSW-NCR. On the comparatively steeper slopes of 0.2 in (a) and 0.1 in (b), it was estimated that the effect of large tidal variation was insignificant on the storm surge computed by the coupling model compared to the non-coupling model. On the other hand, the large tidal variation relatively influences on the storm surge in the case of the slope of 0.05 in (c) based on the scatter in the relation of MSW-CR versus the tidal level. Hence, its difference of MSW-CR and –NCR became larger as the tidal level approached +3m or -2m in (c). It was found that the large tidal variation significantly caused the various magnitudes of MSW-CR on the slope of 0.01 of (d). Especially, the difference of the magnitude between MSW-CR and -NCR was widely induced less than 1.0m due to the tidal variation in (d). The maximum increased difference of MSW-CR to MSW-NCR was estimated as approximately 0.4m in which MSW-CR and MSW-NCR were 3.8 and 3.4, respectively for the slope of 0.01 in (d), while the maximum decreasing difference between both was about 1.1m where MSW-CR was 2.3m on the same slope. The maximum increasing and decreasing difference of MSW-CR to MSW-NCR were approximately 0.3 ~ 0.4m on the slope of 0.05 in (c), which the maximum and minimum of MSW-CR, and MSW-NCR were 2.0, 1.3 and 1.6m, respectively.

As a consequence, the magnitude of the maximum storm surge induced by the wind became larger on the shallower water. In addition, the large disturbance of the maximum storm surge was caused by the large tidal variation. The magnitude of the maximum storm surge decreased in coinciding with the tidal phase above the mean water level, while it increased in encountering the tidal phase below the mean water level.

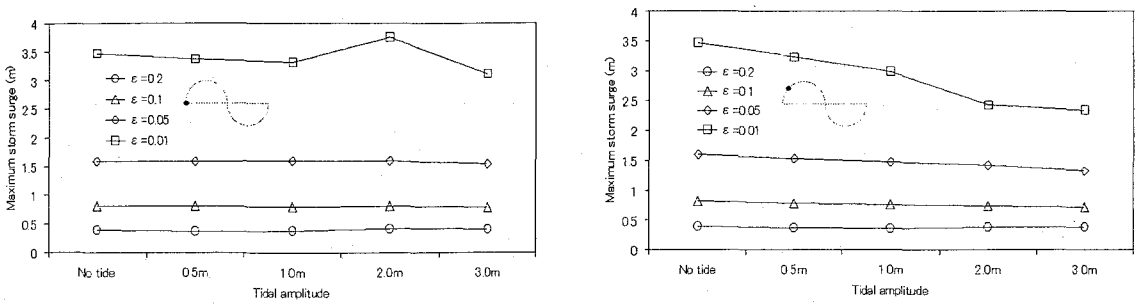

(a) mcb (b) cb

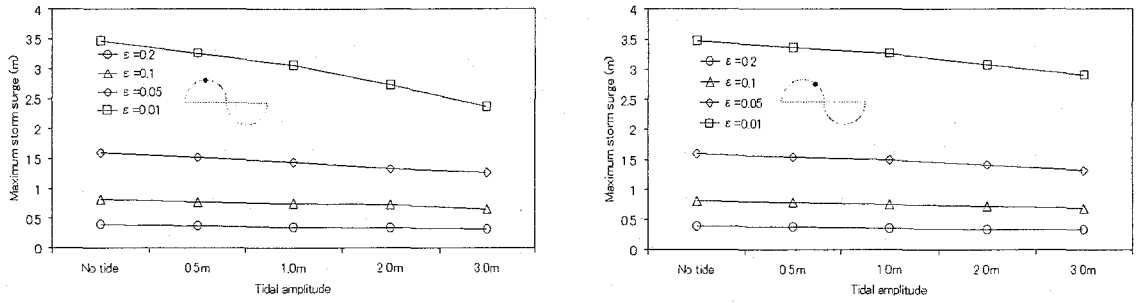

(c) crest (d) ca

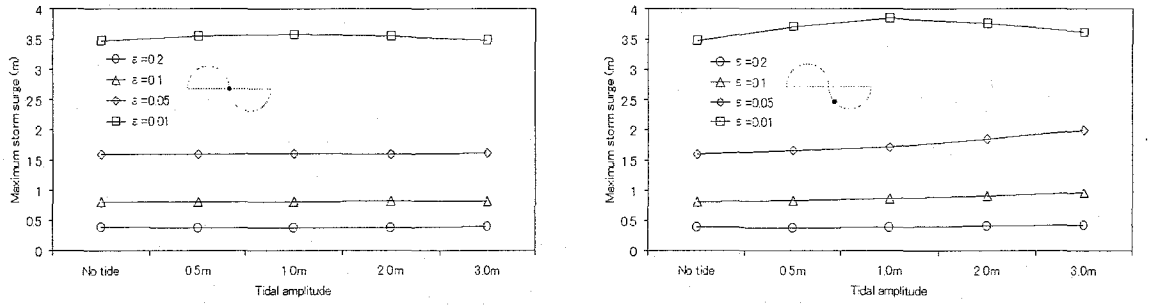

(e) mca (f) tb

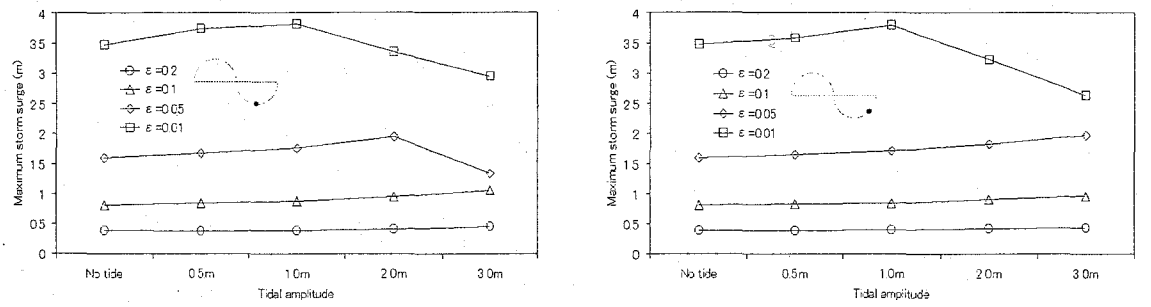

(g) trough (h) ta

Fig. 3.17. The comparison of the variation of MSW occurred at each tidal amplitude and slope associated with the tidal phase (MSW; the maximum storm surge, no tide; non-coupling model).

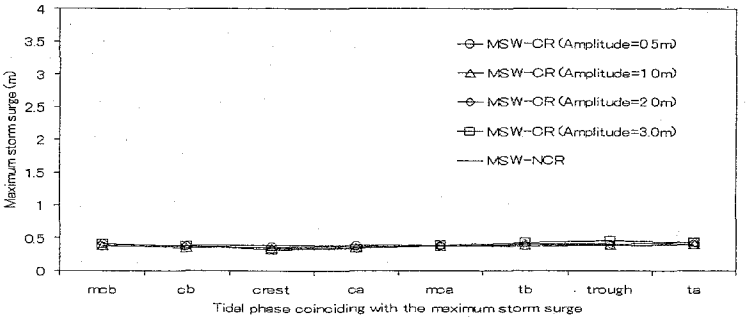

(a) The slope of 0.2

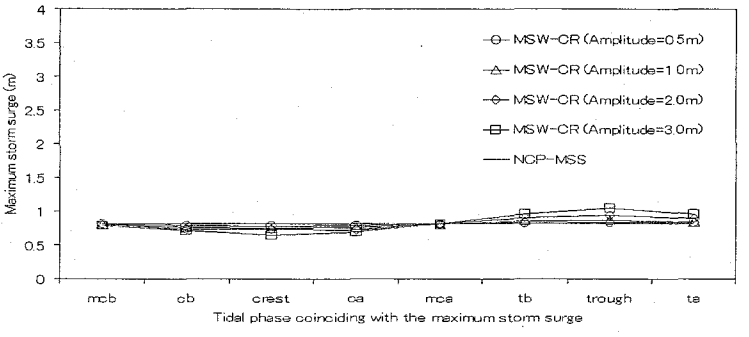

(b) The slope of 0.1

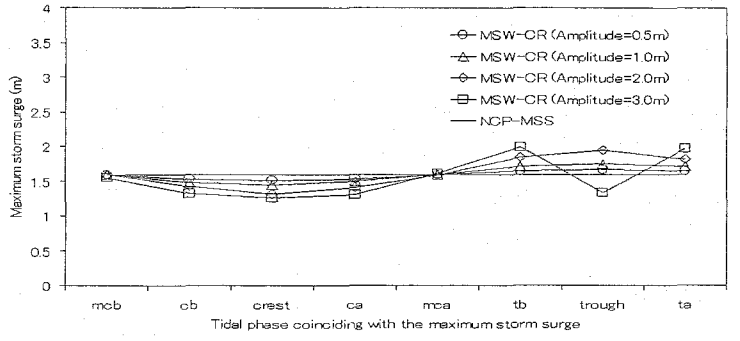

(c) The slope of 0.05

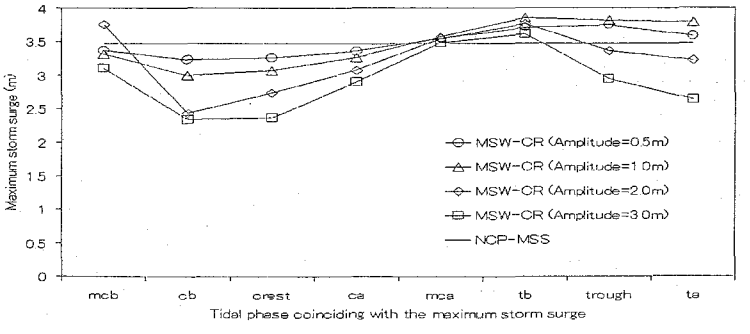

(d) The slope of 0.01

Fig. 3.18. The comparisons of MSW-CRs and –NCR versus the tidal phase on each slope.

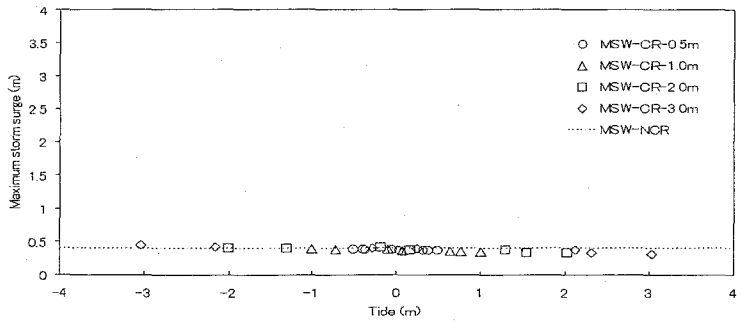

(a) The slope of 0.2

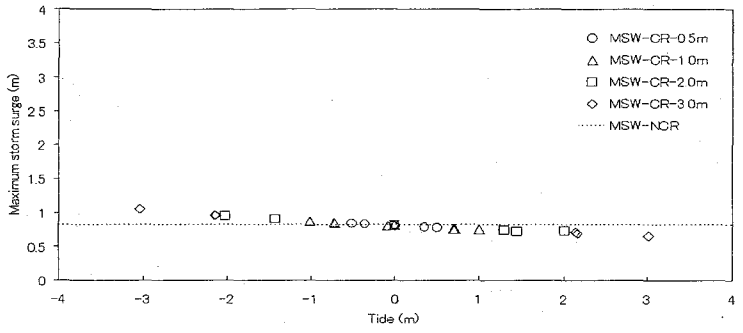

(b) The slope of 0.1

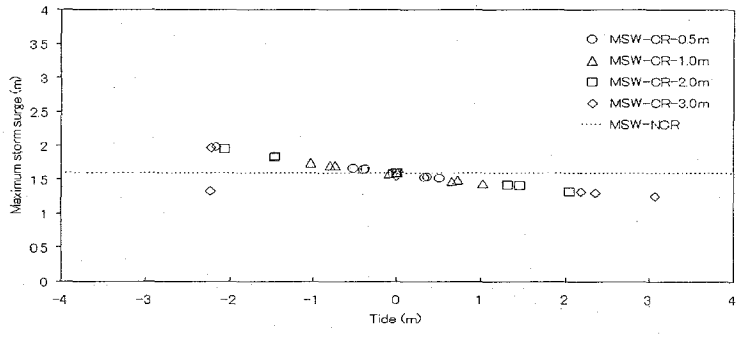

(c) The slope of 0.05

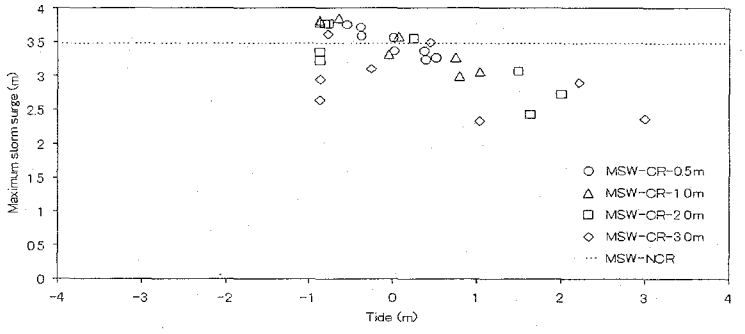

(d) The slope of 0.01

Fig. 3.19. Scatter of maximum storm surges versus the tidal level at each slope

3.4.2. Effect of tide on set-up

In the previous section 3.4.1, it was investigated how the large tidal variation influences on the storm surge through the comparison of the maximum set-ups computed by the coupling model (MSR-CR) with the non-coupling model (-NCR). It was confirmed that the bottom slope resulted in the variation of the magnitude in the storm surge coinciding with the various tidal phases and amplitudes. In addition, when the tidal amplitude became higher, the difference of the magnitudes between MSW-CR and -NCR became larger in general. Using the same way described at 3.4.1, how the large tidal variation affects on the wave set-up, which is the surge induced by the only radiation stress, will be investigated in this section 3.4.2. The magnitudes of MSR-CR and -NCR were computed by Eq. (3.1.7) and (3.1.8). The maximum wave set-up was determined among the set-ups for 6 hours.

Figure 3.20 shows the comparison of the variation in MSR which occurred at each tidal amplitude and slope associated with the tidal phase. The highest MSR-NCR was computed as 0.1m on the slope of 0.05 and the lowest MSW-NCR was computed as 0.03m on the slope of 0.01. When the tidal amplitude became higher, the variation of magnitude in MSR-CR became larger on the slope of 0.01 in the case of (a) *mcb*. On the other hand, the magnitude of MSR-CR was disappeared as the tidal amplitude became larger. Furthermore, the magnitude of MSR-CR was so small that it could be negligible for all cases on the slope of 0.2. For the case of (b) *cb*, the patterns of the variations in the magnitudes of MSR-CRs were similar to the case of (a) *mcb*. However, the magnitude of MSR-CR started to decrease except the slope of 0.01, when the tidal variation became larger. The irregularity was also found in the pattern of the variation for MSR-CR in cases of (a) *mcb* and (b) *cb*. For the cases of (c) *crest* and (d) *ca*, the similarity of the pattern in the variation of MSR-CRs was found as the decay of MSR-CR, when the tidal amplitude became larger. It was also found that the magnitudes of MSR-CRs on the slope of 0.01 significantly varied due to the large tidal variation in cases of (e) *mca*, (f) *tb*, (g) *trough* and (h) *ta*, while the variations of the magnitudes in each MSR-CR on the slope of 0.1 and 0.05 were similar each otheder the same cases. Especially, the highest MSR-CR occurred more than 0.18m on the slope of 0.01 in the case of (c) *crest*, when the tidal amplitude was 3.0m. From the result described above, it could be understood that the bottom slope affected on the magnitude of MSR-CR. The large tidal variation caused the various magnitude in MSR-CR as well.

Figure 3.21 shows the comparison of MSR-CRs and –NCR versus the tidal phase on each slope. The large tidal variation resulted in the decay of the magnitude in all MSR-CRs and then, the magnitudes of MSR-CRs on the slope of 2.0 in (a) were so small that those were negligible. The

maximum increasing difference between MSR-CR and -NCR was 0.17m on the slope of 0.01, which MSR-CR and -NCR were 0.19 and 0.02m, respectively. Its value was found in the case of *trough* in the transverse axis of (d). On the other hand, the maximum decreasing difference between MSR-CR and –NCR was 0.01m and was found in the case of *crest* in horizontal axis of (d), which MSR-CR was 0.01m. The variation of the magnitudes in MSR-CRs on the slope of 0.05 showed the similar pattern to that on the slope of 0.1 over all. Additionally, the maximum increasing difference between MSR-CR and -NCR was 0.04m on the slope of 0.05 in (c). The maximum decreasing difference between both was 0.04m as well on the same slope. MSR-CR for the former was 0.14m but for the latter was 0.06m. MSR-NCR was 0.1m. The maximum increasing and decreasing difference between both were 0.08 and 0.05m on the slope of 0.1 in (b), respectively. The MSR-CR for the former was 0.15m, while for the latter was 0.02m. MSR-NCR was 0.07m. It was found that the maximum variation of MSR-CR occurred on the slope of 0.01. Hence, the large tidal variation and the bottom slope should affect on the wave set-up.

Using the same way explained as Fig. 3.19 at the previous section 3.4.1, the relations of the maximum set-up level induced by the wave radiation stress versus the tidal level were investigated shown in Fig. 3.22. On the slope of 0.2 in (a), the magnitudes of MSR-CRs became smaller than that of MSR-NCR at all tidal phases due to the large tidal variation. On the other hand, the scatter of the magnitudes in MSR-CRs was clearly stratified by the parts of the negative and positive tidal level on the slopes of 0.1 in (b) and 0.05 in (c). The magnitudes of MSR-CRs became smaller than that of MSR-NCR at the positive tidal level, but larger at the negative tidal level. In addition, the difference of the magnitude between MSR-CR and -NCR increased, as the tidal level approached ±3m or -2m. For the slope of 0.01 in (d), the magnitudes of MSR-CRs were distributed above that of MSR-NCR. As mentioned at the previous paragraph, the highest difference between MSR-CR and -NCR generated more than 0.17m on the slope of 0.01 in (d). As a consequence, the large tidal variation sensitively influences on the magnitude of the wave set-up.

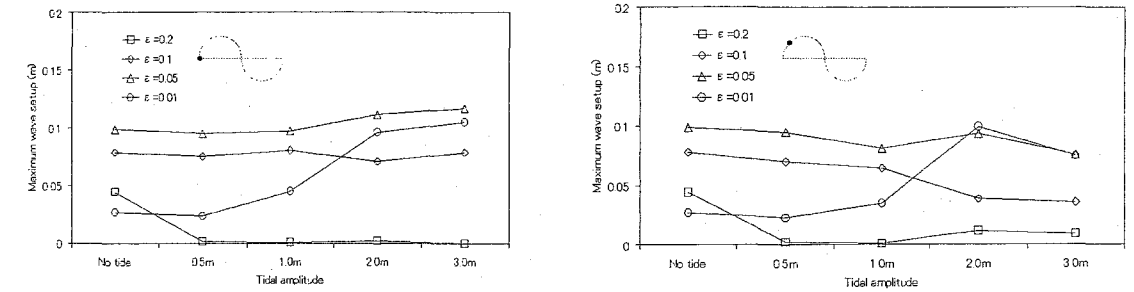

(a) mcb

(b) cb

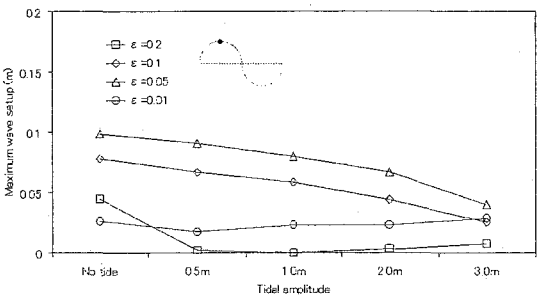

(c) crest

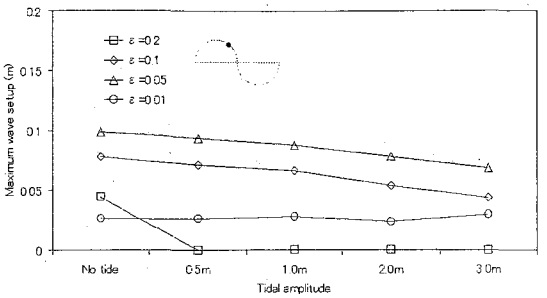

(d) ca

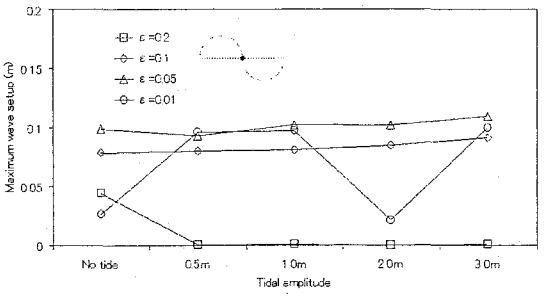

(e) mca

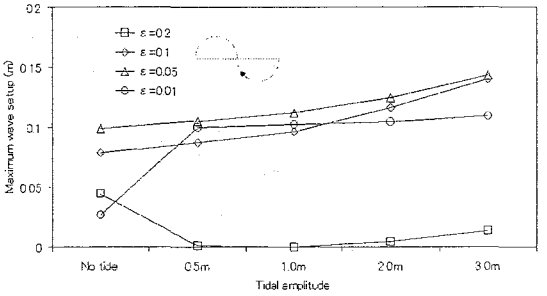

(f) tb

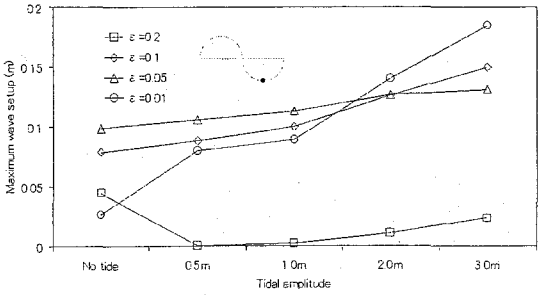

(g) trough

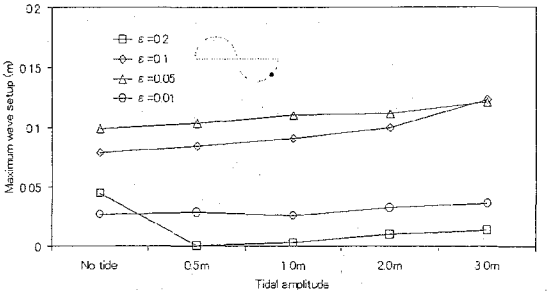

(h) ta

Fig. 3.20. The comparisons of the variations of MSRs occurred at each tidal amplitude and slope associated with the tidal phase (MSR; set-up, no tide; non-coupling model).

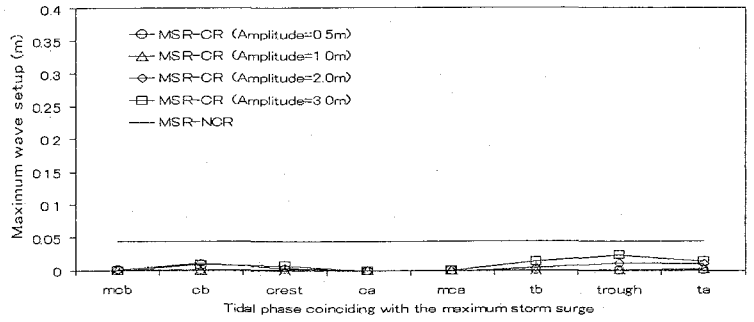

(a) The slope of 0.2

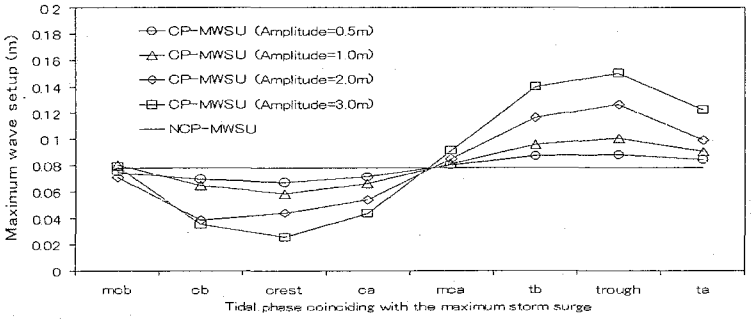

(b) The slope of 0.1

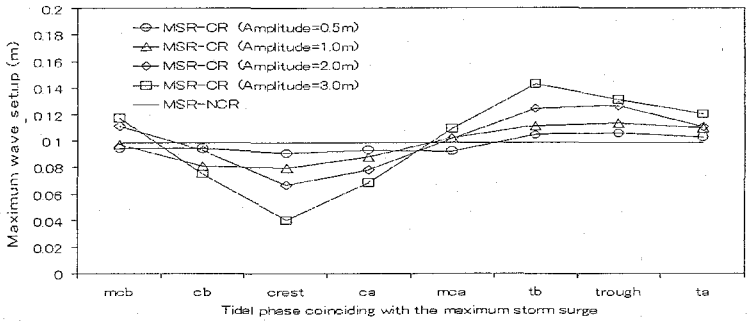

(c) The slope of 0.05

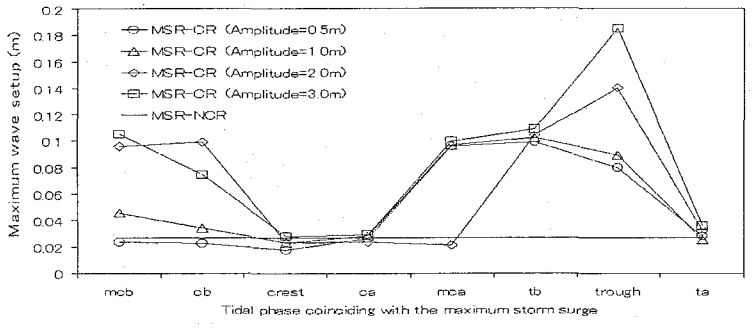

(d) The slope of 0.01

Fig. 3.21. The comparisons of MSR-CRs and –NCR versus the tidal phase on each slope.

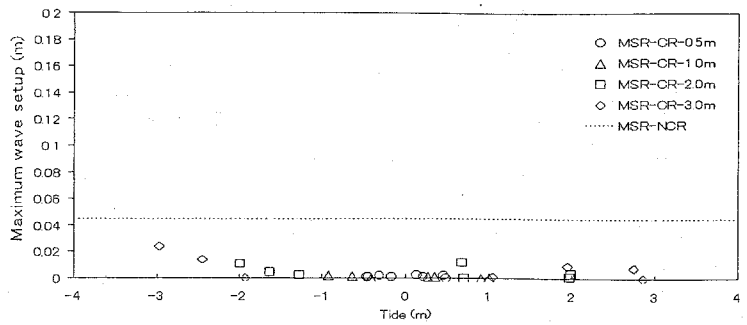

(a) The slope of 0.2

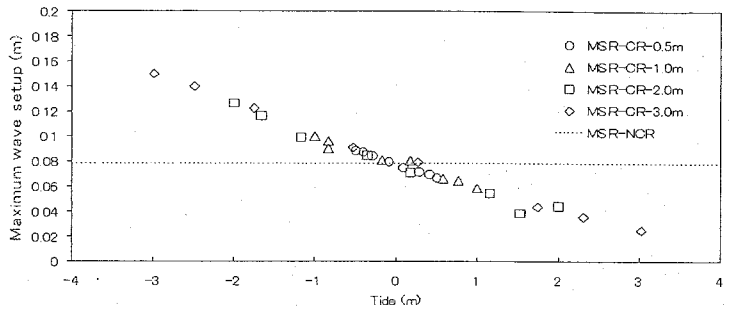

(b) The slope of 0.1

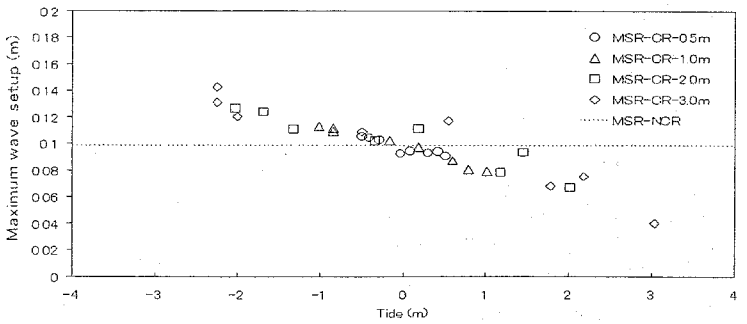

(c) The slope of 0.05

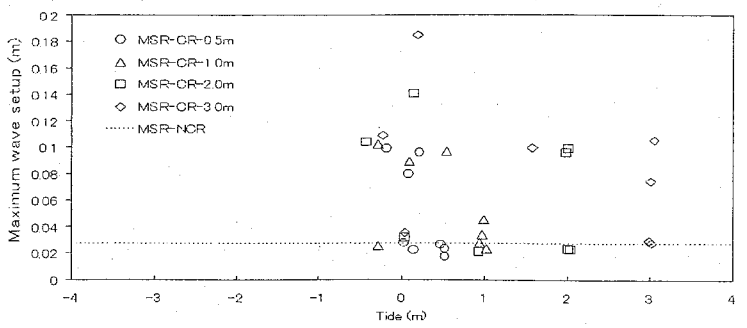

(d) The slope of 0.01

Fig. 3.22. Scatter of the maximum storm surges versus the tidal level at each slope

3.4.3. Effect of tide on water level

In terms of the water level, the effect of the tidal variation on the maximum water level (MSSL) will be examined by the comparison of MSSL-CR of $\eta_{tide+ws+rs}$ with -NCR of Eq. (3.1.9). Note that the magnitude of MSSL-NCR was linearly added MSW-NCR to η_{tide}.

Figure 3.23 shows that the comparison of MSSL-CRs with -NCR relating to the tidal amplitude at each tidal phase on the slope of 0.2. Comparing MSSL-CR with -NCR at each tidal phase, it was found that the difference of them was insignificant at all tidal phases. Fig. 3.24 shows that the comparison of MSSL-CR and -NCR relating to the tidal phase at each tidal amplitude on the slope of 0.2. The highest maximum water level occurred at *crest* in (d) among all maximum water levels as shown in Fig. 3.24, when the tidal amplitude was 3.0m.

In addition, it was found that the difference of MSSL-CRs and -NCR on the tidal amplitude of 3.0m started to appear at all tidal phases on the slope of 0.01 as shown in Fig. 3.25. The magnitude of MSSL-NCR was larger than that of MSSL-CR in (b), (c) and (d) in Fig. 3.25, the discrepancy of them was, however, negligible on the slope of 0.1. The highest maximum water level generated at *crest* in the horizontal axis of (d) in Fig. 3.26 when the tidal amplitude was 3.0m and then, its variation was similar to that on the slope of 0.2.

Figure 3.27 depicts that the comparison of MSSL-CRs and -NCR relating to the tidal amplitude at each tidal phase on the slope of 0.05. The discrepancy of them significantly appeared when the tidal amplitude became higher. The magnitudes of MSSL-CRs decreased compared to that of MSSL-NCR in (b) *cb*, (c) *crest* and (d) *ca*, when the tidal amplitude became larger. However, the magnitudes of MSSL-CRs became slightly higher in (f) *tb*, (g) *trough* and (h) *ta* as the variation of the tidal amplitude was large. On the slope of 0.05, the highest maximum water level occurred at *crest* and (d) when the tidal amplitude was 3.0m as shown in Fig. 3. 28. Especially, it was clearly confirmed that the difference of MSSL-CR and –NCR decreased at all cases on the slope of 0.01 in Fig. 3.29, even if the tidal amplitude was 0.5m. The occurrence of the difference between both was particularly more apparent, when the tidal amplitude was 3.0m as shown in Fig. 3.29. The apparent difference of the magnitude between both was represented with respect to the tidal amplitude in Fig. 3.30. As the tidal amplitude became larger, the magnitude of MSSL-CR decreased compared to that of MSSL-NCR.

Although all maximum water levels were investigated at the observation point near the shoreline, the confirmation is conducted for the cross shore profile in the maximum water level

generated in the case of *crest* and (d) of the tidal amplitude of 3.0 on each slope. Fig. 3.31 shows the comparisons of the cross profiles in the water level under the conditions for the tidal phase of *crest* and the tidal amplitude of 3.0m on each slope of 0.2, 0.1, 0.05 and 0.01. As shown in Fig. 3.31, the maximum water level computed by the non-coupling model (MSSL-NCR) was higher than that computed by $\eta_{tide+ws+rs}$ (MSSL-CR) on all slopes at the moment, when the peak of the storm surge occurred. Especially, the difference of magnitude between both became larger on the portion of the land.

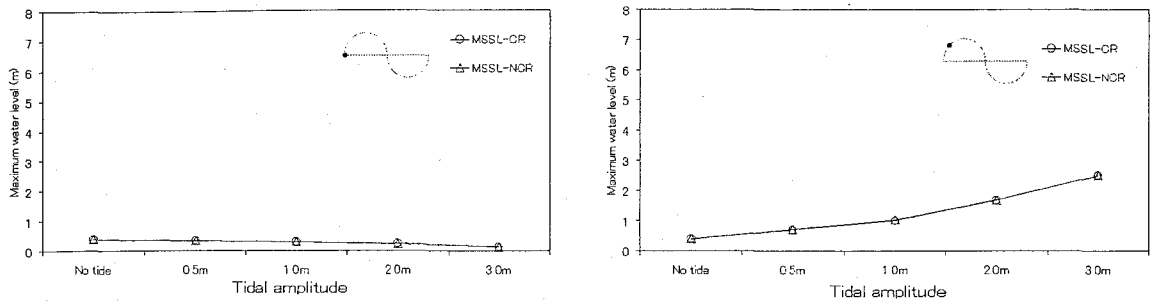

(a) mcb

(b) cb

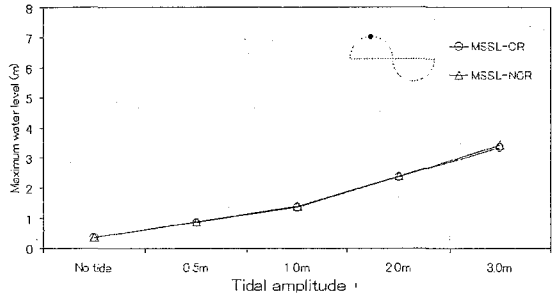

(c) crest

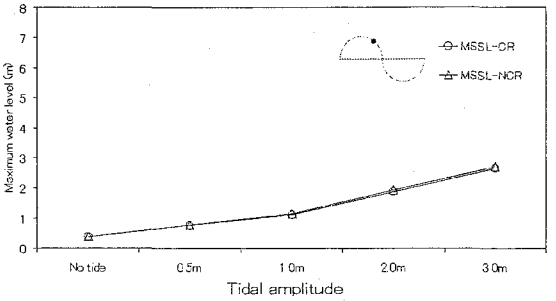

(d) ca

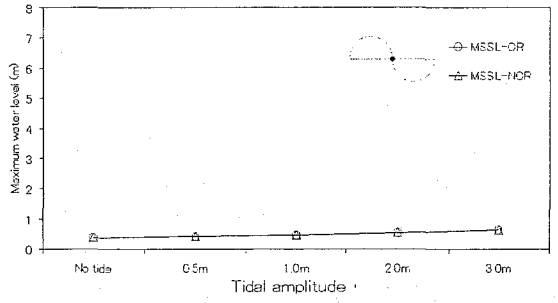

(e) mca

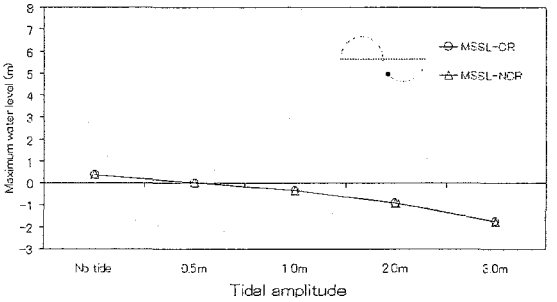

(f) tb

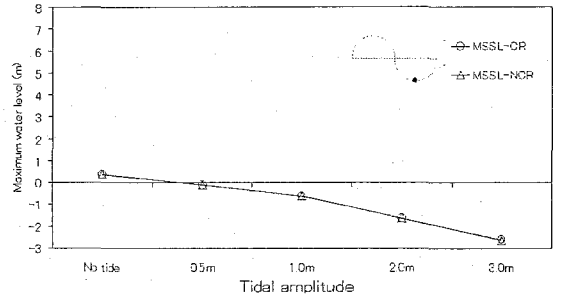

(g) trough

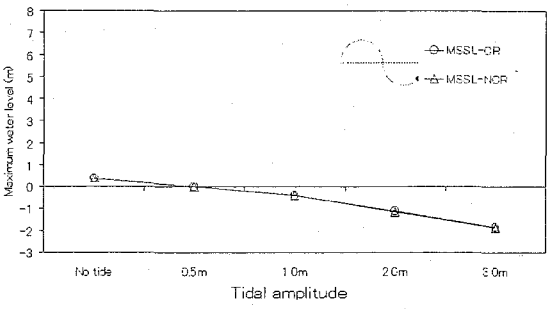

(h) ta

Fig. 3.23. The comparisons of MSSL-CR and MSSL-NCR associated with the tidal amplitude at each tidal phase on the slope of 0.2 (MSSL-CR: the coupling model, -NCR: the non-coupling model).

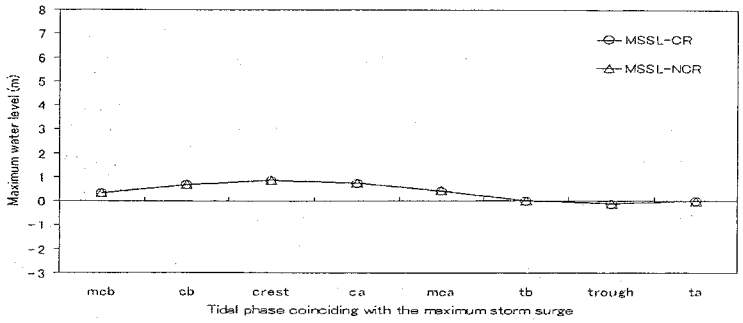

(a) The tidal amplitude of 0.5m

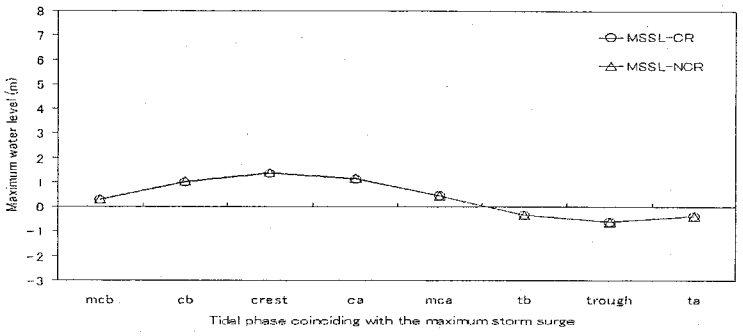

(b) The tidal amplitude of 1.0m

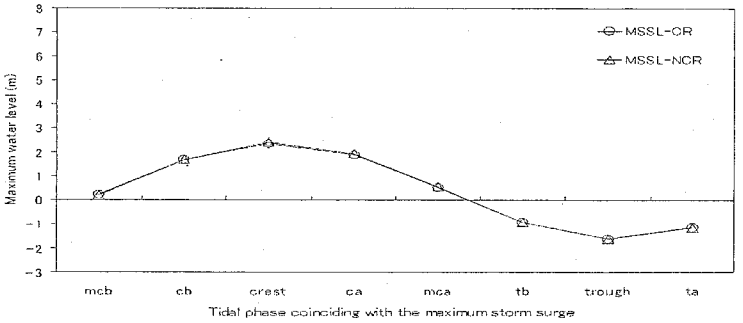

(c) The tidal amplitude of 2.0m

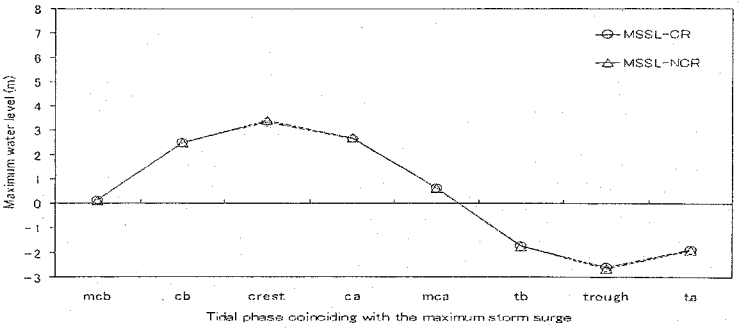

(d) The tidal amplitude of 3.0m

Fig. 3.24. The comparison of MSSL-CR and MSSL-NCR associated with the tidal phase on slope of 0.2 (MSSL-CR: the coupling model, -NCR: the non-coupling model).

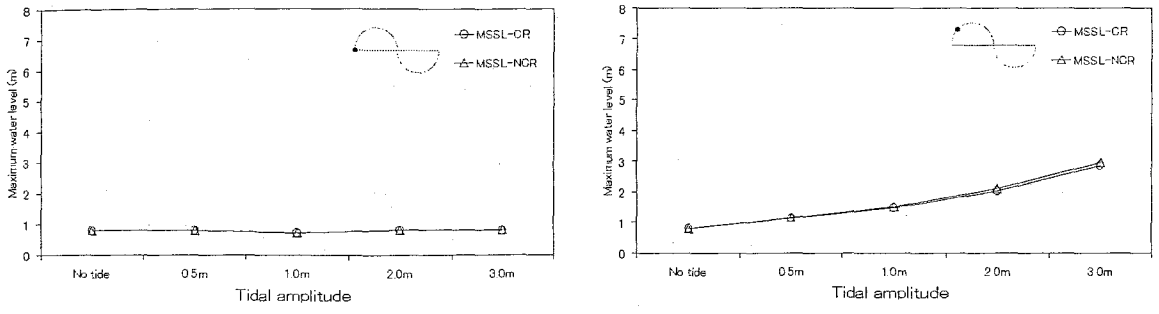

(a) mcb

(b) cb

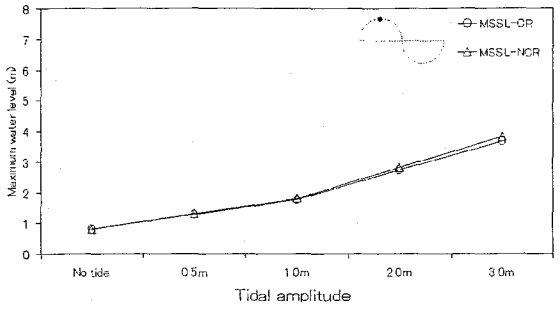

(c) crest

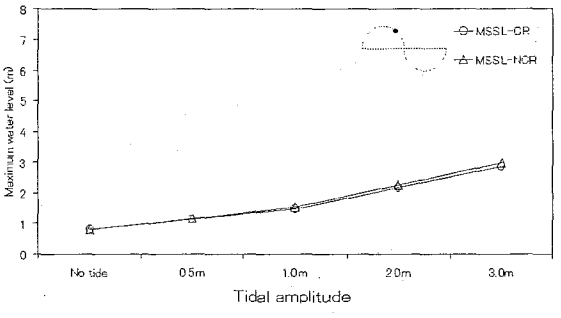

(d) ca

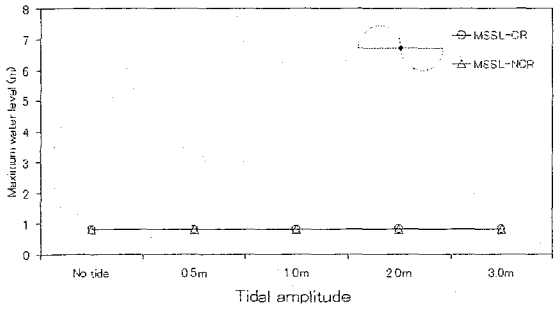

(e) mca

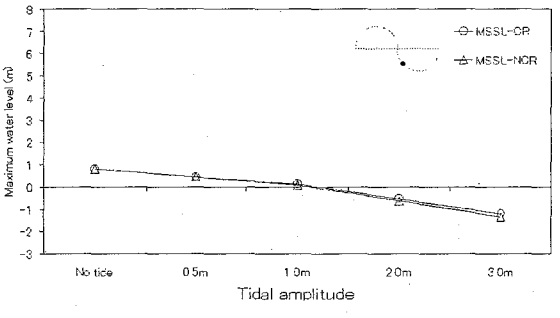

(f) tb

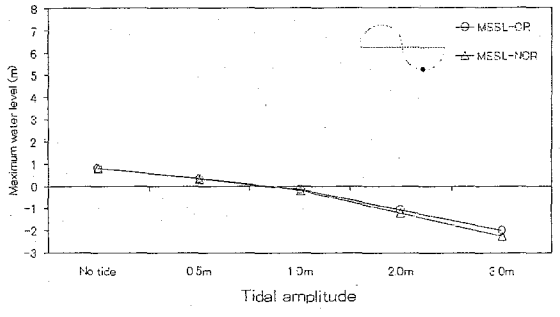

(g) trough

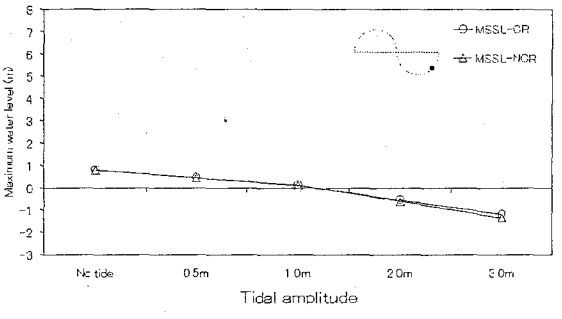

(h) ta

Fig. 3.25. The comparison of MSSL-CR and MSSL-NCR associated with the tidal amplitude on the slope of 0.1 (MSSL-CR: the coupling model, -NCR: the non-coupling model).

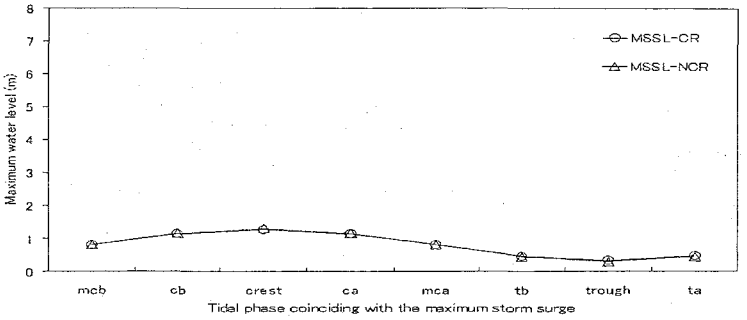

(a)The tidal amplitude of 0.5m

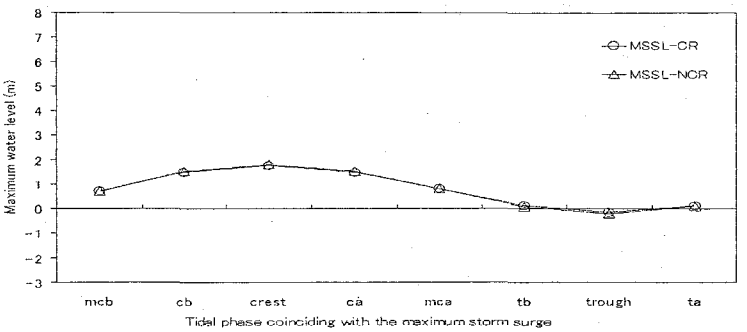

(b) The tidal amplitude of 1.0m

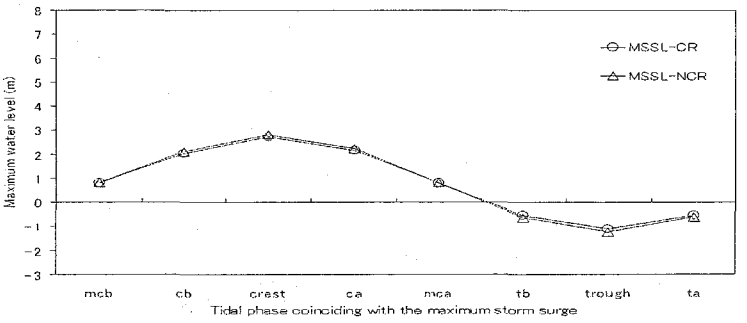

(c) The tidal amplitude of 2.0m

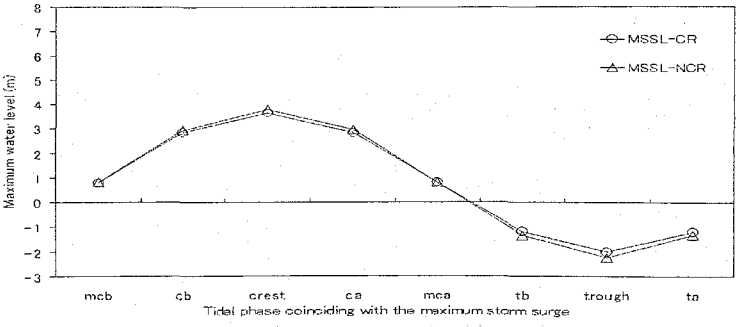

(d) The tidal amplitude of 3.0m

Fig. 3.26. The comparison of MSSL-CR and MSSL-NCR associated with the tidal phase on the slope of 0.1 (MSSL-CR: the coupling model, -NCR: the non-coupling model).

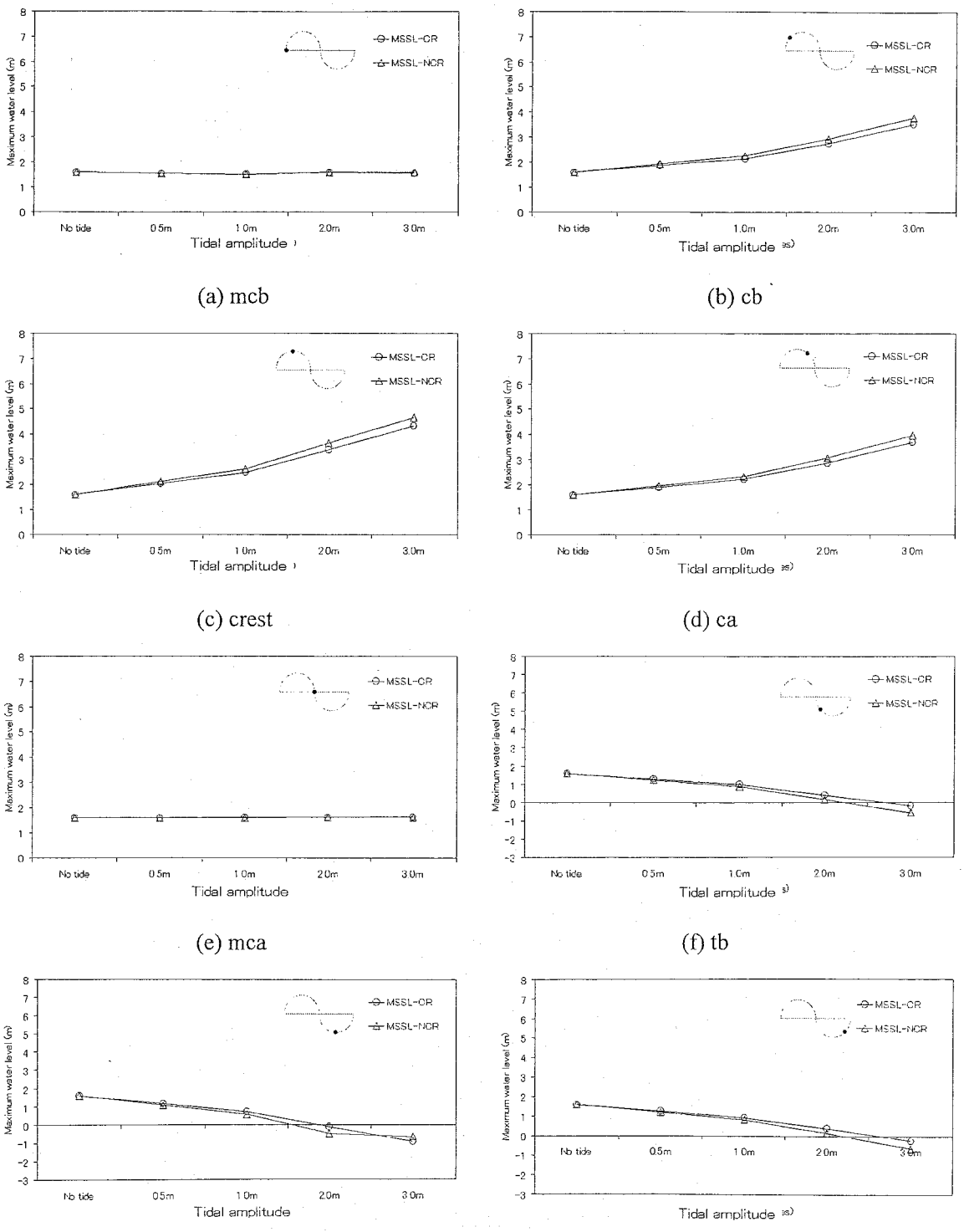

Fig. 3.27. The comparison of MSSL-CR and MSSL-NCR associated with the tidal amplitude on the slope of 0.05 (MSSL-CR: the coupling model, -NCR: the non-coupling model).

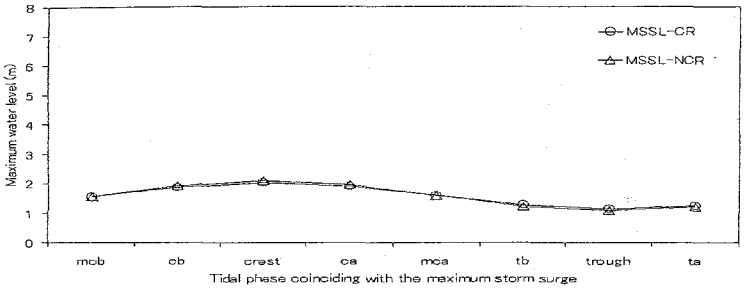

(a) The tidal amplitude of 0.5m

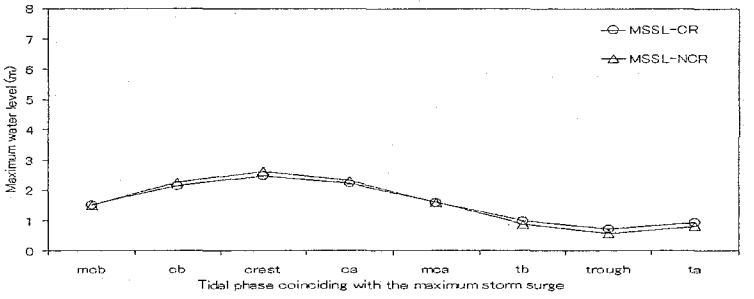

(b) The tidal amplitude of 1.0m

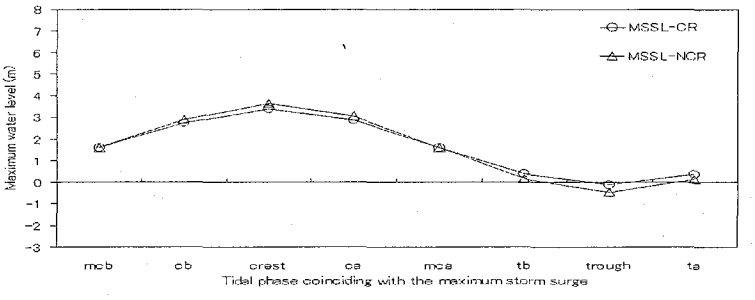

(c) The tidal amplitude of 2.0m

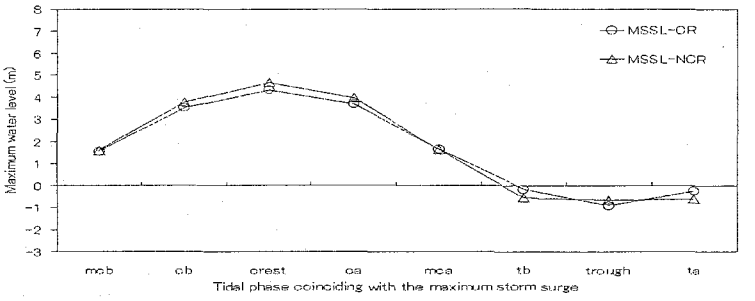

(d) The tidal amplitude of 3.0m

Fig. 3.28. The comparison of MSSL-CR and MSSL-NCR associated with the tidal phase on the slope of 0.05 (MSSL-CR: the coupling model, -NCR: the non-coupling model).

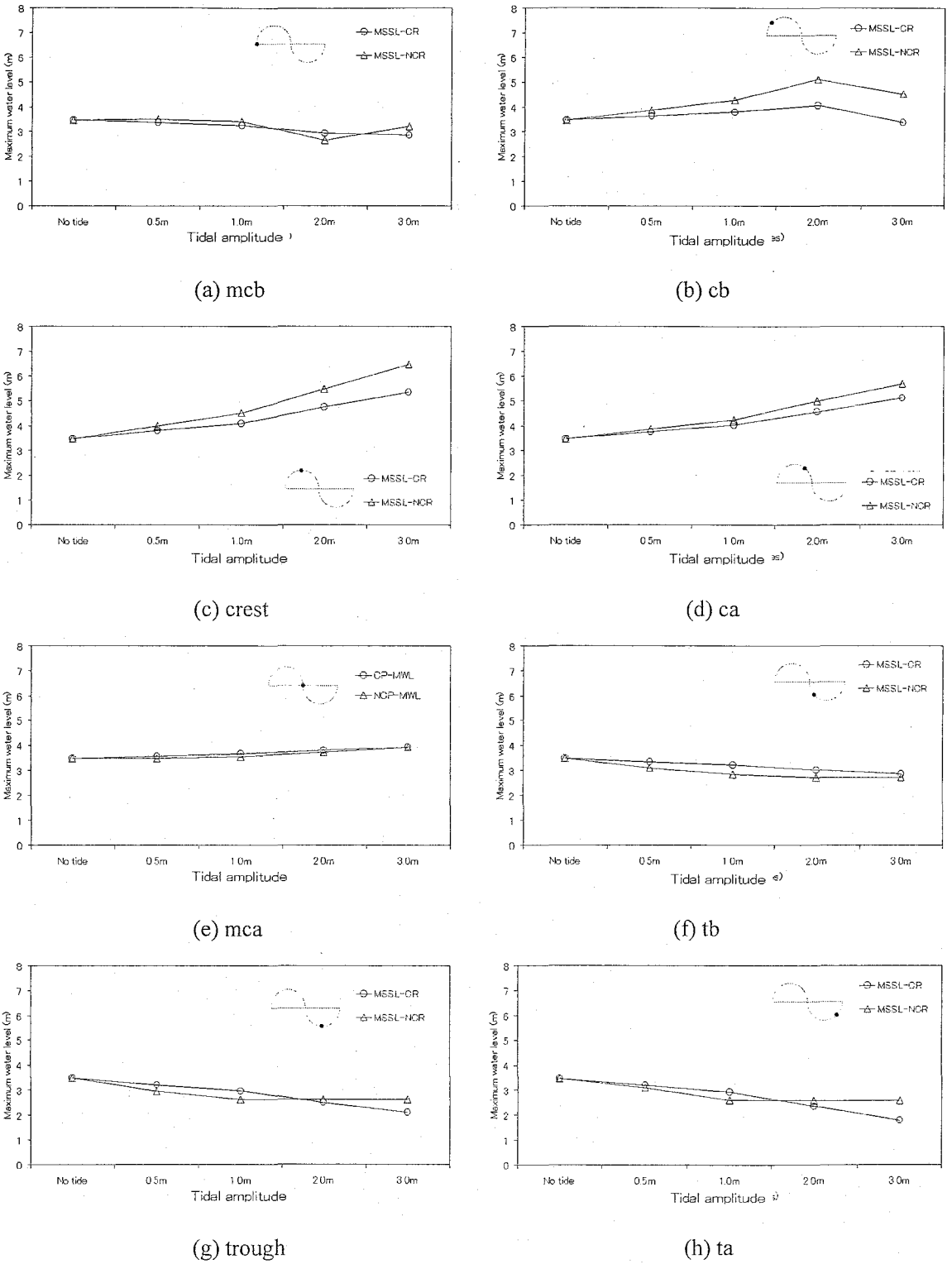

(a) mcb (b) cb

(c) crest (d) ca

(e) mca (f) tb

(g) trough (h) ta

Fig. 3.29. The comparison of MSSL-CR and MSSL-NCR associated with the tidal amplitude on the slope of 0.01 (MSSL-CR: the coupling model, -NCR: the non-coupling model).

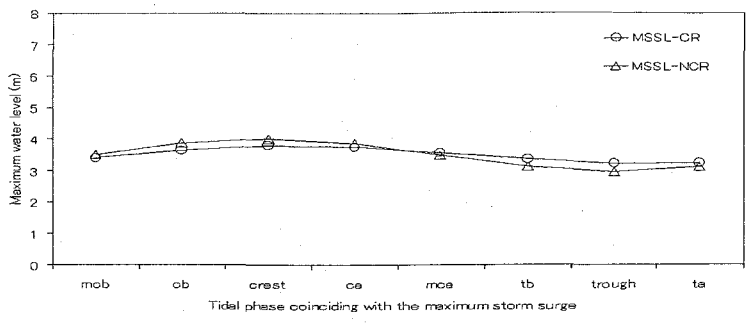

(a) The tidal amplitude of 0.5m

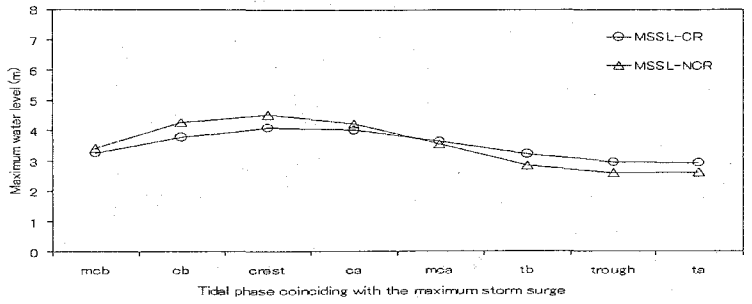

(b) The tidal amplitude of 1.0m

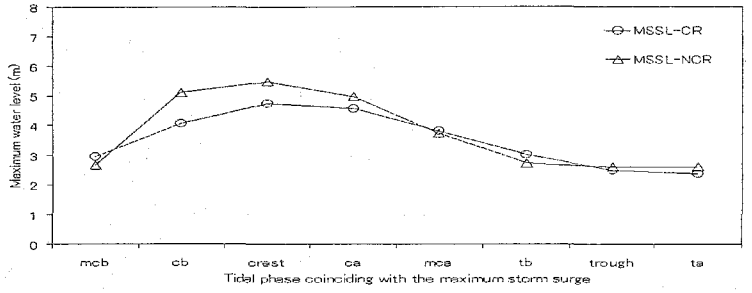

(c) The tidal amplitude of 2.0m

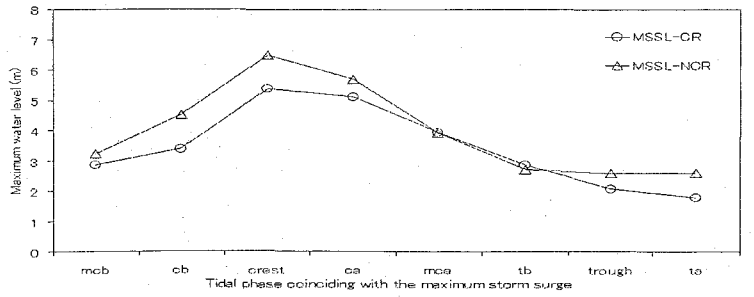

(d) The tidal amplitude of 3.0m

Fig. 3.30. The comparison of MSSL-CR and MSSL-NCR associated with the tidal phase on the slope of 0.01 (MSSL-CR: the coupling model, -NCR: the non-coupling model).

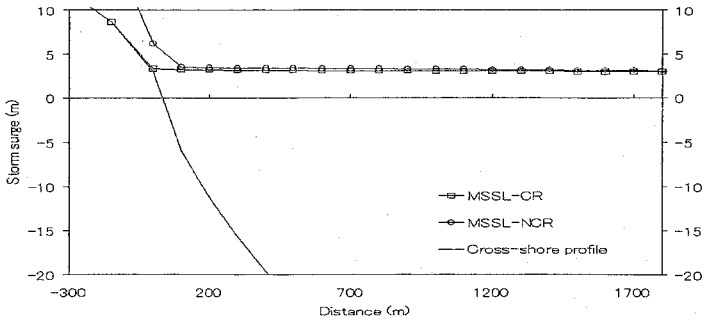

(a) The slope of 0.2

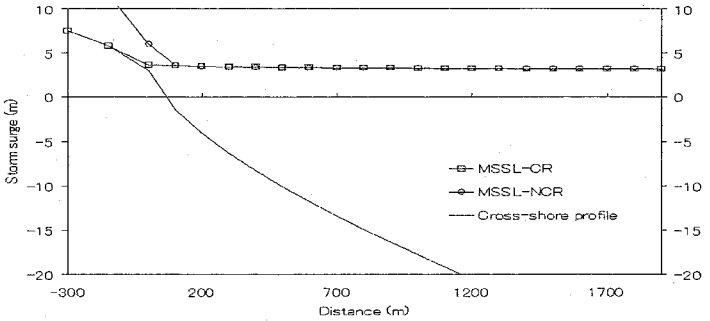

(b) The slope of 0.1

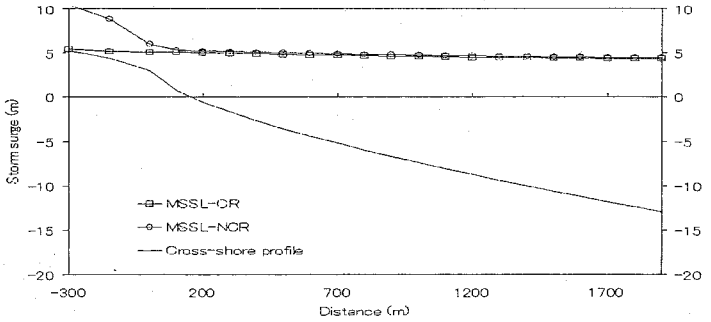

(c) The slope of 0.05

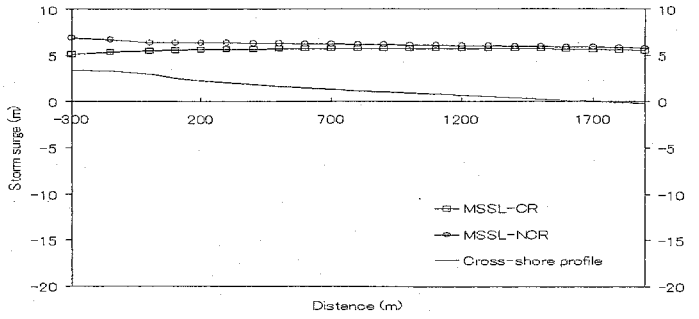

(d) The slope of 0.01

Fig. 3.31. The comparison of cross profile in the storm surge computed by CR and NCR on each slope, when the maximum storm surge occurred at the observation point (The tidal amplitude; 3.0m, the tidal phase; *crest*).

Chapter 4

Application to western coastal sea of Korea

The Chapter 3 investigated the characteristics of the behavior of the storm surge induced by the combination of the wind stress and the radiation stress, and the set-up induced by the only radiation stress on the various slopes and tidal amplitudes under the simplified assumption. In chapter 4, the hindcast of the modeled typhoon was conducted by applying the coupling model to the west coast of Korea so as to study the characteristic of the behavior of the storm surge and the set-up on the four subsequent levels of computational domains. As the modeled typhoon, Typhoon 0314 (Maemi), which hit the Korean Peninsula with the severest magnitude, was selected to hindcast the server situation in the coastal sea. In addition, the western coastal region of Korea has been well known as the area of the large tidal variation. Especially, the tidal amplitude of up to 4.0m has been recorded on the spring tide at Gunsan for the study. Therefore, the hindcast of the simulation will provide the information of the storm surge due to the modeled typhoon identical to the magnitude of Typhoon 0314.

4.1. Geographical feature

The case studies provide the hindcast of the storm surge level with respect to the tidal variation along the western coastal area of Korea resulting from the modeled typhoon. The typhoon track

and the study location provide the necessary information to define the model regions and resolution. Fig. 4.1 and Table 4.1 show the computational domains and bathymetry at the four levels of geographical regions. The modeled regions and resolution was selected to consider the large tidal variation and to investigate the storm surge levels.

Figure 4.1 (a) shows the ocean region, which extends from 20°N to 42°N and from 117°E to 132°E with a resolution of about 10 km. The computational domain covers whole Yellow Sea including Taiwan and Kyushu of Japan to allow sufficient time and fetch for the development of the storm surge and waves through the numerical simulation (Kim, 2006b). The water depth in Yellow sea and South Sea of Korea is fairly shallow less than 300m, but the water depth in the east of Taiwan and the south of Kyushu is deep. This resolution is needed for proper transition to the more resolved coastal region around Gunsan. The high resolution of costal region in Fig. 4.1 (d) is nested through two intermediate regions of Fig. 4.1 (b) and (c) to maintain the rate of the fine to coarse grid which is 1/2 or 1/3. The water depth in Fig. 4.1 (b) shows under 80m in offshore and its domain regions extends from 35.02°N to 36.26°N and from 125.23°E to 127.05°E resolved by averaged 3.3km. The intermediate depth of Fig. 4.1 (c) decreases from 50m toward shoreline and extends from 35.29°N to 36.11°N and from 125.51°E to 126.49°E to cover the coastal region for the information of the storm surge. Fig. 4.1 (d) provides the shallow area with the high resolution of about 350m. Its water depth is shallow and its region includes breakwaters, islands and head land. The water depth around island on offshore is relatively deep compared to the water depth near 20m. In the right side of the breakwater below the head land, the reclaiming work has been done to recover the land from the sea. The station marked by the triangle represents the harbor and the tidal observation has been set up. The break water above the head land is to protect the harbor from waves propagated from northwest. The station of *B* provides the information of the storm surge level in the simulation. More detail is listed on Table 4.1. The sea marked by the star has been isolated from the vicinity by the breakwater and the flow has been supplied through the gate at the south of the domain 4. But the gate is not represented in Fig. 4.1. In addition, the water depth is very shallow at the sea marked by the star.

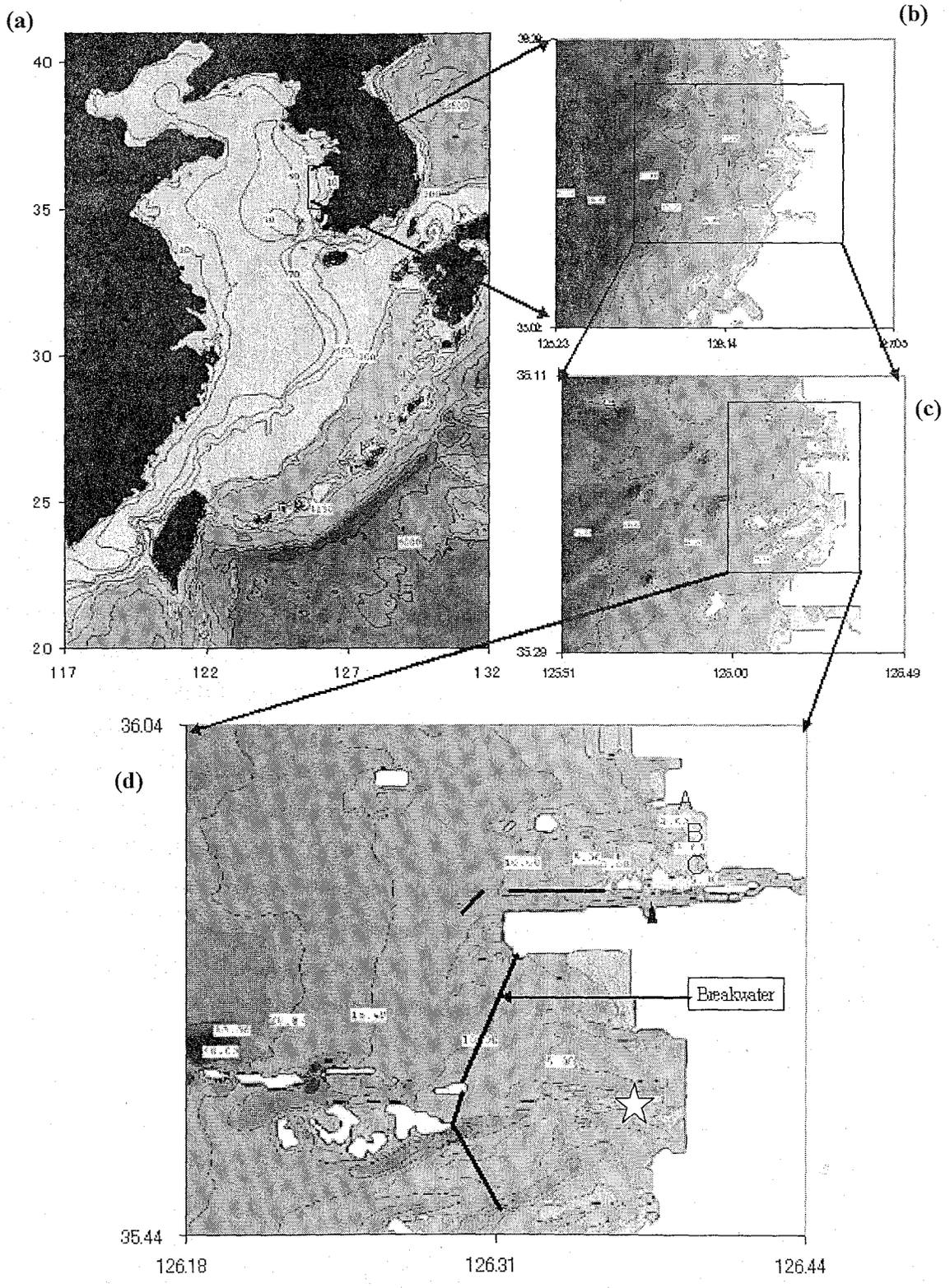

Fig. 4.1. The four levels of geographic regions.

The bathymetries were discretized on the computational domains by digitizing the sea charts published by the National Oceanographic Research Institute, Ministry of Maritime Affairs and Fisheries(MMAF), Republic of Korea. In Fig. 4.1 the depths are 10.1 and 1.17m at the station of ▲ and *B*, respectively.

Table 4.1. The four levels of computational domains.

Domain	The range of domain	The grid size	Num. grids
1	117E – 132E, 20N – 41N	Δx = 9,392.7m Δy = 11,035.4m	151×211
2	125.23E–127.05E, 35.02N – 36.26N	Δx = 3,130.9m Δy = 3,678.5m	52×42
3	125.51E – 126.494E 35.29N – 36.1140N	Δx = 1,044.0m Δy = 1,266.0m	88×64
4	126.1820E – 126.4353E 35.4420N – 36.0353N	Δx = 348.0m Δy = 408.7m	115×101

4.2. Simulation condition

The hindcast of the modeled typhoon provides the information of the storm surge level on the domain 4. The case studies provide the various storm surge level, which the timing of the generation in the maximum storm surge level is changeable on the tidal phase with the interval of about 1 hour 30 minutes.

Table 4.2 shows experimental cases of the tidal phases and amplitudes for the simulation. The tidal amplitude was chosen as four cases of 1.0, 2.0, 3.0 and 4.0m and the tidal phase encountering the peak of the storm surge was selected as eight cases listed in Table 4.2 to provide the storm surge level influenced by the tidal variation. In addition, the simulation was conducted in the case of the storm surge on the still water level to compare with the experimental cases with the tidal variation. An illustration denotes the timing of the generation of he maximum storm surge encountering the tidal phase. For example, in the case of *mcb*, the maximum storm surge occurs at the moment when the tidal phase crosses the mean water level from the low to high tide. Hence, the storm surge on the low tide starts to generate, grow up and approach the maximum storm surge at the mean water level. After its peak, it starts to decrease

and disappear on the high tide. In the case of *crest*, the peak of the storm surge occurs on the crest of the spring tide. For *cb*, the peak generates in the middle between *mcb* and *crest*. For *mca*, one takes place when the tidal phase crosses the mean water level from the high to low tide. The peak occurs in the middle between *crest* and *mca* in the case of *ca*. For *trough*, it simultaneously coincides with the trough with the neap tide. Therefore, *tb* and *ta* mean that the maximum occurs in the middle between *mca* and *trough*, and *trough* and *mcb*, respectively. The interval between *mcb* and *cb* was about 1 hour 30 minutes during a period of approximately 12 hours in the tide. On the other hand, the tidal amplitudes were selected as 1.0, 2.0, 3.0 and 4.0m because the tidal range has been recorded more than 8.0m at the observation marked by the triangle in the domain 4.

In general, the storm surge simulation on the still water level is conducted by considering the combination of the wind stress, the radiation stress and the atmospheric pressure resulting in the inundation at the coastal region. However, it was expected that the tidal variation should highly influence on the storm surge in the west coast of Korea from the result of chapter 3 described. Therefore, the hindcast of storm surge was conducted with imposing the tide on the simulation. Additionally, the tide simulation was conducted without any forces to yield the storm surge represented by

$$\eta_{st} = \eta_{tide+ws+rs+pr} - \eta_{tide} \tag{4.1}$$

where *st* represents the storm surge, *ws*; the wind stress, *rs*; the radiation stress and *pr*; the atmospheric pressure.

In order to compare with the magnitude of the storm surge above, the storm surge on the still water level for the reference is computed by

$$\eta_{st,rf} = \eta_{ws+rs+pr} \tag{4.2}$$

where *rf* denotes the reference.

For the set-up induced by the radiation stress, all components are first considered on the simulation and it is subtracted by the simulation considering the wind stress, atmospheric pressure and tide as follows:

$$\eta_{rs} = \eta_{tide+ws+rs+pr} - \eta_{tide+ws+pr} \tag{4.3}$$

For the reference of the set-up on the still water level, it is represented by

$$\eta_{rs,rf} = \eta_{ws+rs+pr} - \eta_{ws+pr} \tag{4.4}$$

Here, the terminology should be used to avoid the confusion as follows:

Coupling model (CR): the simulation with the tide.
Non-coupling model (NCR): the simulation without the tide.
Storm surge: the surge induced by the combination of the wind stress, the atmospheric pressur and radiation stress.
Set-up: the surge induced by the only radiation stress.
Maximum storm surge (MSW): the highest storm surge level occurred due to a typhoon.
Maximum set-up (MSR): the highest set-up level occurred due to a typhoon.
Maximum sea surface level (MSSL): the highest water level occurred due to a typhoon.

From now on, the terminology described above will be used to describe the result of the simulation. For example, *MSR-NCR* refers to the maximum set-up induced by the radiation stress in the non-coupling model. Therefore, MSW-CR is evaluated by Eq. (4.1), MSR-CR; Eq. (4.3), MSW-NCR; Eq. (4.2), MSR-NCR; Eq. (4.4), MSSL-CR; $\eta_{tide+ws+rs+pr}$ and MSSL-NCR; $\eta_{ws+rs+pr}$.

Table 4. 2. Experimental cases of the tidal phases and amplitudes.

Tidal phase at the maximum storm surge	Tidal amplitude (m)	Case
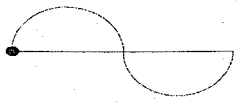	1.0m	mcb
	2.0m	
	3.0m	
	4.0m	
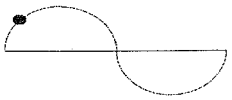	1.0m	cb
	2.0m	
	3.0m	
	4.0m	
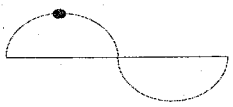	1.0m	crest
	2.0m	
	3.0m	
	4.0m	
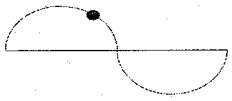	1.0m	ca
	2.0m	
	3.0m	
	4.0m	
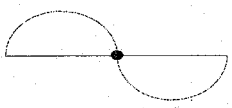	1.0m	mca
	2.0m	
	3.0m	
	4.0m	
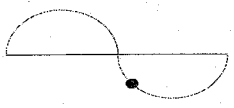	1.0m	tb
	2.0m	
	3.0m	
	4.0m	
	1.0m	trough
	2.0m	
	3.0m	
	4.0m	
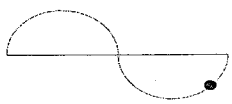	1.0m	ta
	2.0m	
	3.0m	
	4.0m	

4.3. Modeled typhoon

Recently, one of the most severe typhoons was Typhoon 0314 (Maemi) in 2003which caused the life loss and missing of 117 persons and property damage of about 5,138,000,000 USD in Korea. Takayama et al. (2004) surveyed and described the storm surge and wave disasters caused by Typhoon 0314. The maximum storm surge of 2.5m was observed at Masan Bay, while that of 0.6m was observed at the Pusan Port due to Typhoon 0314 (Maemi) in 2003. As listed in Table 4.2, the typhoon was born near 140°E 25°N at 6 September 2003 and it passed near 125.1°E 25.2°N at 11 September with the central pressure of about 910 hPa and started to turn northeast (Fig. 4.2). It later moved to northeast and hit Sachun with the central atmospheric pressure of 950 hPa and wind speed of 40m/s at 12 September. After the landfall, it passed through Uljin with the pressure of 970 hPa and wind speed of 31 m/s at 13 September. In the study, the data of Typhoon 0314 (Maemi) used by Takayama et al. (2004) was reused modifying its track and the modeled typhoon has the same wind speed and atmospheric pressure with Typhoon 0314. The track of modeled typhoon is established to pass through the study region of Gunsan as shown in Fig. 4.2. Hence, the modeled typhoon hits Gunsan with the atmospheric pressure of 950 hPa similar to Typhoon 0314.

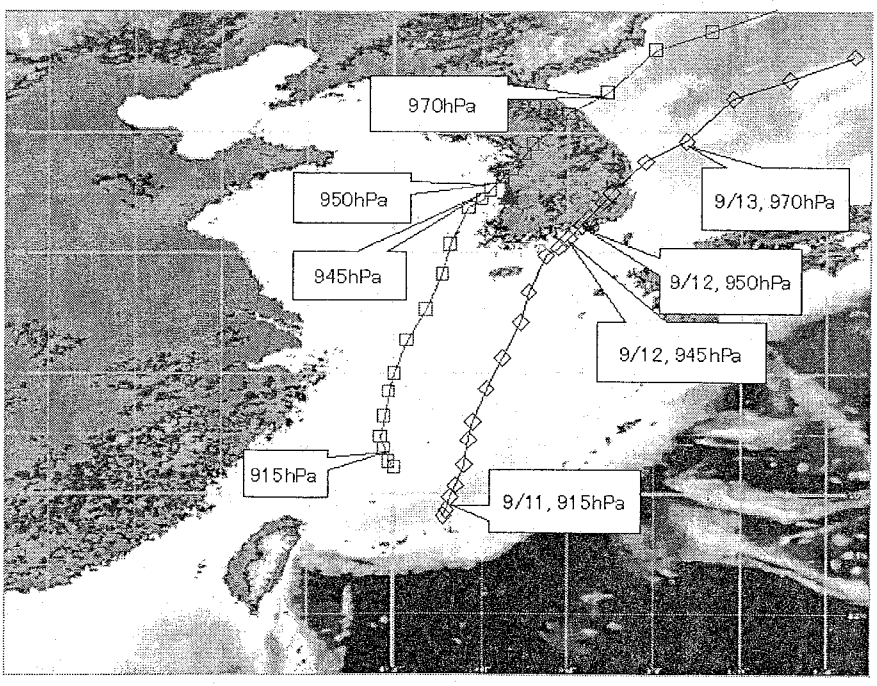

Fig. 4.2. Tracks of Typhoons 0314 (Maemi) and modeled typhoon (Diamond, Typhoon 0314; square, modeled typhoon; triangle, Gunsan).

Table 4. 3. The track of Typhoon 0314.

TIME(UTC)	Latitude(°N)	Longitude(°E)	Pressure(hPa)
2003091100	252	1251	910
2003091103	255	1252	920
2003091106	259	1253	920
2003091109	263	1254	925
2003091112	270	1256	930
2003091115	278	1257	935
2003091118	284	1258	935
2003091121	295	1261	935
2003091200	305	1265	930
2003091206	327	1271	935
2003091209	339	1275	945
2003091212	349	1283	955
2003091218	370	1298	970
2003091300	391	1318	975
2003091306	405	1346	980
2003091309	415	1369	980
2003091312	423	1381	980
2003091315	432	1400	980
2003091318	447	1412	980
2003091321	460	1435	984
2003091400	452	1457	984

4.4. Hindcast simulation for numerical experiment

4.4.1 Wind and atmospheric pressure

Figure 4.3 shows the time history of the atmospheric pressure in the simulation at the station of *B*. When the modeled typhoon passed through the study area, the lowest pressure was simulated as 960 hPa and then, it was similar to that of 950 hPa observed at Sachun due to Typhoon 0314. Therefore, the modeled typhoon fairly produced the atmospheric pressure of Typhoon 0314 (Maemi) in the storm surge simulation. Fig. 4.5 shows the pressure field of averaged 950 hPa distributed spatially at the computational domain 4 at 37 hours. Fig. 4.4 shows the time histories of the wind speed and direction produced by the modeled typhoon at the station of *B*. The

modeled typhoon produced slightly the wind speed of 35m/s smaller than that of 40m/s when Typhoon 0314 (Maemi) actually landed on Sachun. However, the difference between both was so small that the modeled typhoon could reproduce the wind and atmospheric field close to their observations induced by Typhoon 0314. The wind direction changed from the east toward the west around 37 hours, when the modeled typhoon passed through at Gunsan on the computational domain 4. The wind, which changed the direction, is spatially distributed in the domain 4 at 37 hours as shown in Fig. 4.6. The wind direction indicated the northeast at 37 hours.

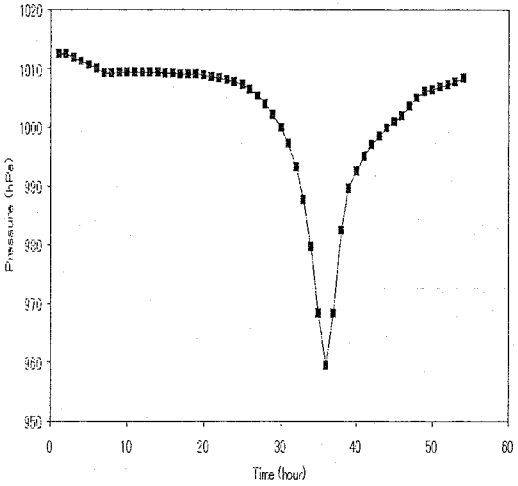

Fig. 4.3. The time history of the atmospheric pressure at the station of B.

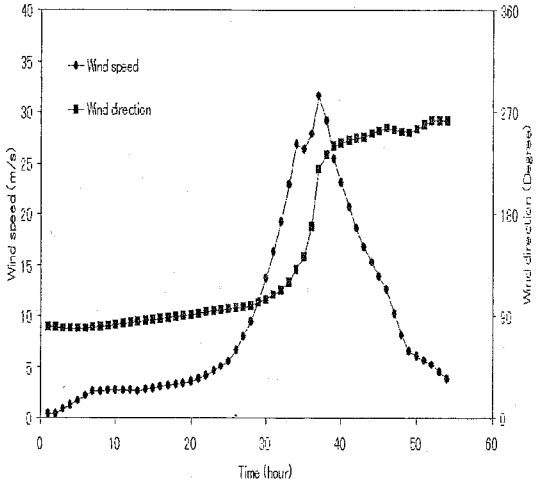

Fig. 4.4. The time history of the wind speed and direction at the station of B.

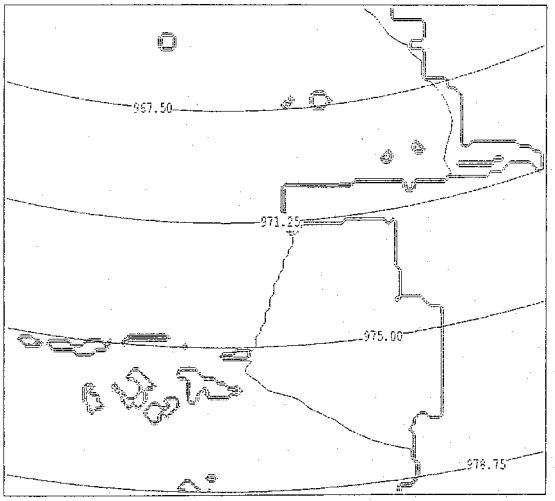

Fig. 4.5. The spatial distribution of the atmospheric pressure at 37 hours.

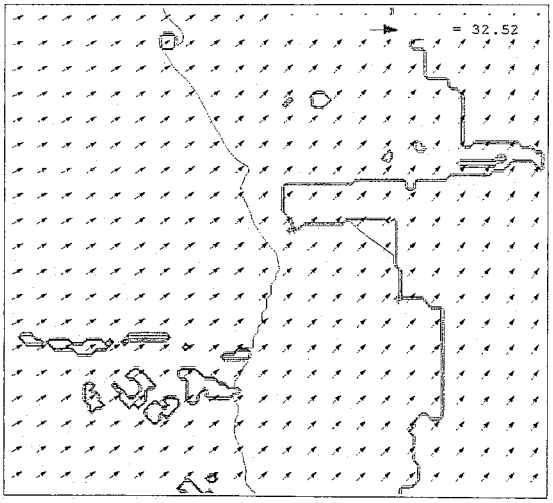

Fig. 4.6. The spatial distribution of the wind field in the domain 4 at 37 hours.

4.4.2. Sea surface level

The hindcast simulation provides the water level generated by the modeled typhoon in the computational domain 4. The water level will be briefly described in the cases of the amplitude of 1.0 and 4.0m and compared with that on the still water level, when the modeled typhoon passed through Gunsan with the tidal phase of *crest* around 37 hours.

On the still water level, the water level occurred more than 3.0m near the shoreline, on the other hand, it generated more than 1.4m in offshore as shown in Fig. 4.7. The water level became 3.5m at the point of the star and 3.9m at the most coastal lines for the non-coupling model. It was confirmed that the higher water level occurred on the coastal line comparing with the offshore. On the other hand, it was investigated that in the case of *crest*, the storm surge occurred on the shoreline for the coupling model in encountering the crest of the spring tide when tidal amplitudes were 1.0 and 4.0m. The maximum water level occurred more than 4.39m in Fig 4.8 for the tidal amplitude of 1.0m and it generated more than 5.99m in Fig. 4.9 for that of 4.0m. The water level on the still water level in Fig. 4.7 + the tidal amplitude of 1.0 was 4.98m larger than the maximum water level of 4.39m in the former. The water level on the still water level in Fig. 4.7 + the tidal amplitude of 4.0m was 7.98m larger than the maximum water level of 6.25m. From Figs. 4.7, 8 and 9, it was expected that the relation of the tide and the storm surge might not be independent any more.

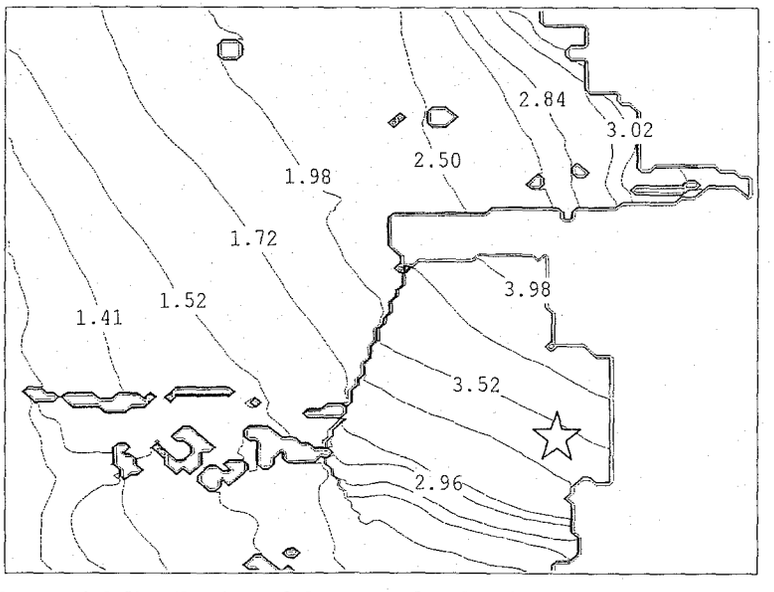

Fig. 4.7. The spatial distribution of the water level at 37 hours on the still water level.

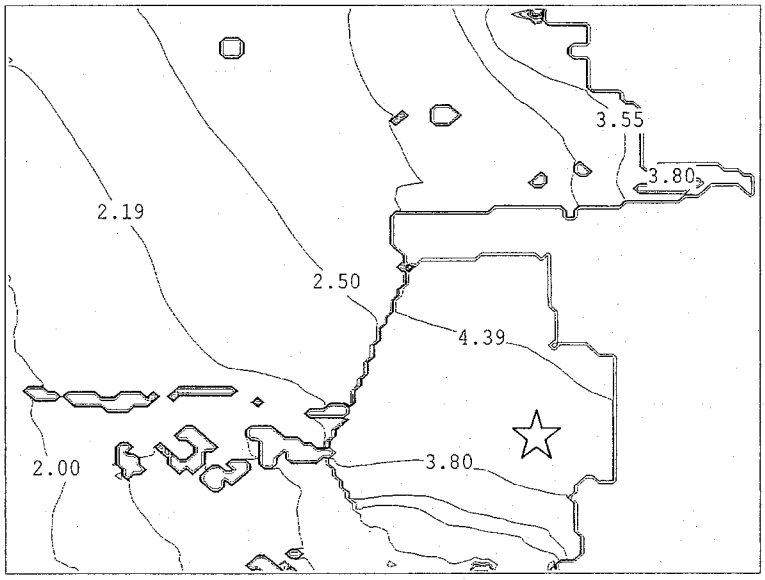

Fig. 4.8. The spatial distribution of the water level at 37 hours (the tidal amplitude; 1.0m, the tidal phase; *crest*).

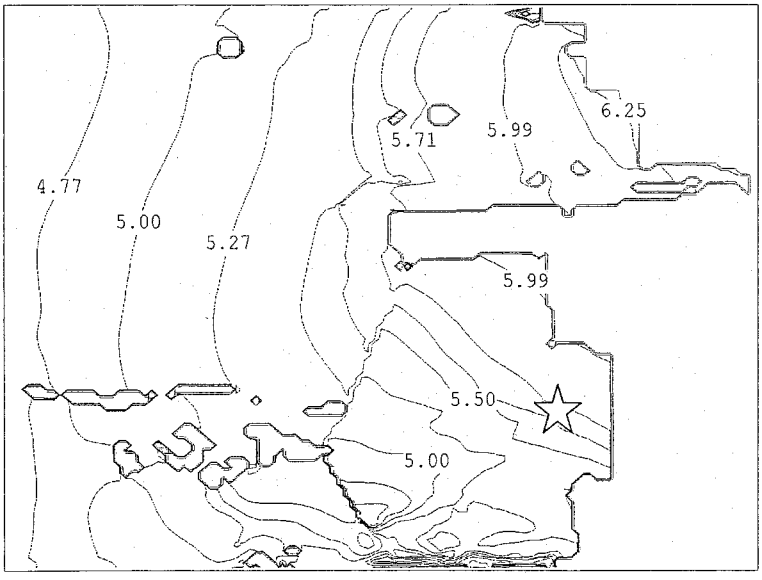

Fig. 4.9. The spatial distribution of the water level at 37 hours (the tidal amplitude; 4.0m, the tidal phase; *crest*).

4.4.3. Storm surge and set-up

The storm surge generated during the storm event is yielded by Eqs. (4.1) or (4.2) and the set-up is also computed by Eqs. (4.3) or (4.4). The storm surge level was estimated to apprehend the relation of the storm surge and the tide. In this section, the storm surge and set-up produced by the modeled typhoon will be described for some cases. Furthermore, the spatial distribution of the storm surge in some cases will be explained to understand its characteristic around Gunsan.

Figure 4.10 shows the time histories of set-up and storm surge in some cases. At first, it is mentioned why the negative value in the storm surge profile appeared, before the peak of the storm surge generated. In general, the negative value occurs after a typhoon passes through a station. In this case, the wind blew from the sea to the land. However, the modeled typhoon produced that the wind blew from the land to the sea before the typhoon passed through Gunsan. Therefore the negative value occurred around 34 hours. In addition, the profiles of the set-ups indicated that the timing of generation in the set-up did not coincide with that of the storm surge.

The storm surge was computed more than 3.0m by the non-coupling model at the station of *B* as shown in Fig 4.7. However, the smaller storm surges were calculated more than 2.6 and 2.2m by the coupling model around the station of *B* as shown in Fig. 4.11 and 4.12, and they were smaller than the storm surge level of 3.0m in Fig. 4.7.

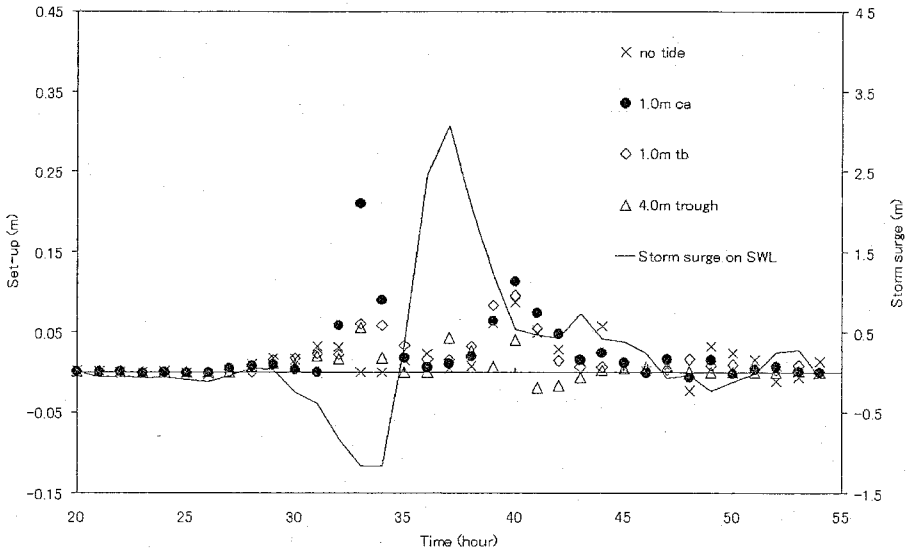

Fig. 4.10. The time histories of set-ups and storm surge at the station of *B*.

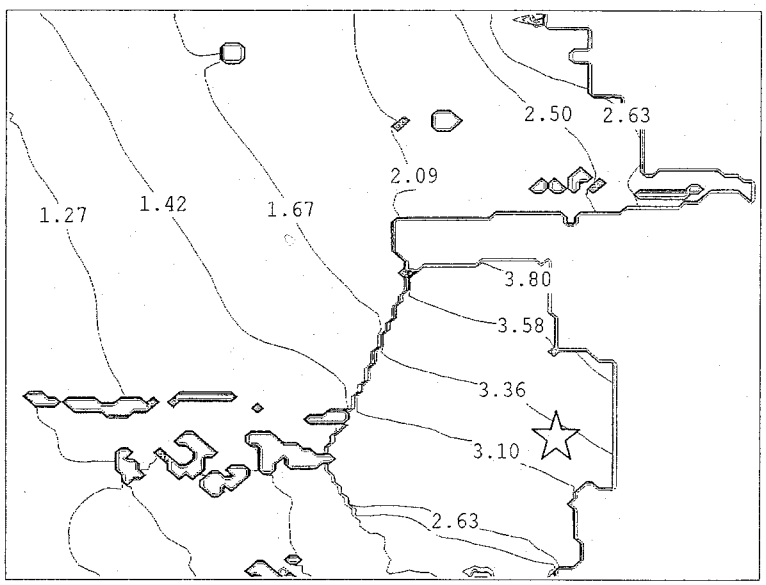

Fig. 4.11. The spatial distribution of the storm surge at 37 hours (the tidal amplitude; 1.0m, the tidal phase; *crest*).

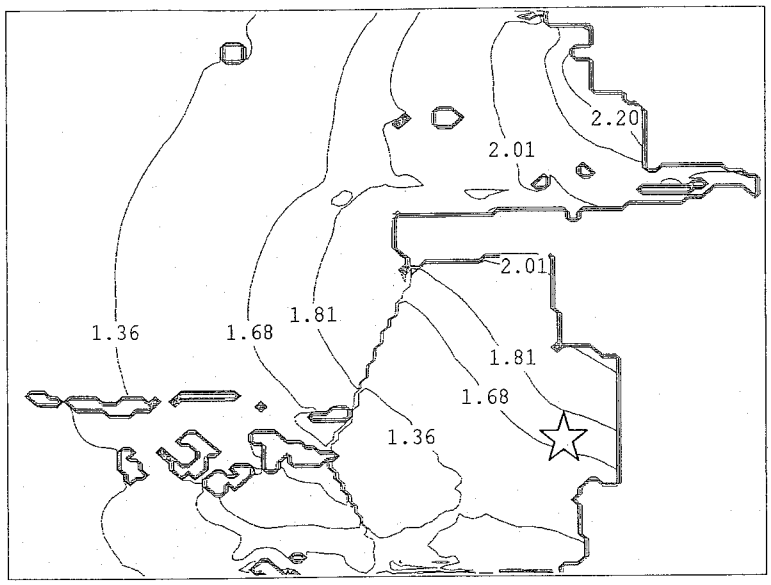

Fig. 4.12. The spatial distribution of the storm surge at 37 hours (the tidal amplitude; 4.0m, the tidal phase; *crest*).

4.4.4. Significant wave height

Although the relation of the storm surge and tide due to a typhoon was focused at the western coastal region of Korea which the water depth was shallow in the study, the development of waves were also one of the most important factors. Therefore, the spatial distributions and profiles of waves are briefly introduced from the hindcast simulation of the modeled typhoon.

From Fig. 4.13 and 14, the time histories of the significant wave heights show the tidal modulation with a period of 12 hours such as the sinusoidal wave. The significant wave height became larger around 37 hours, however, it became smaller around 40 hours. In addition, the significant wave height occurred more than 3.0m and propagated to the shoreline as shown in Fig. 4.16, while it generated approximately 2.0m and approached to the coastal line as shown in Fig. 4. 15. In addition, the peaks of the significant wave heights varied as changing tidal amplitudes and tidal phases.

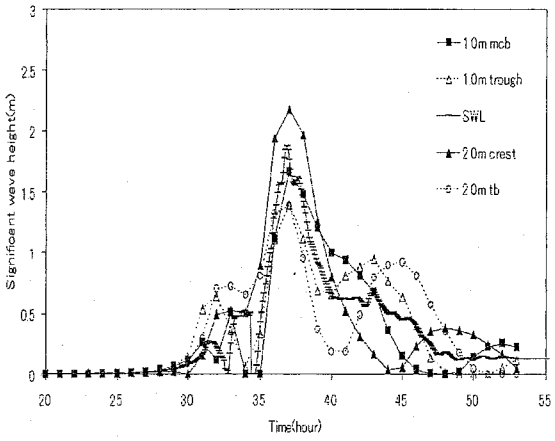

Fig. 4.13. The time history of the significant wave height at the station of *B*.

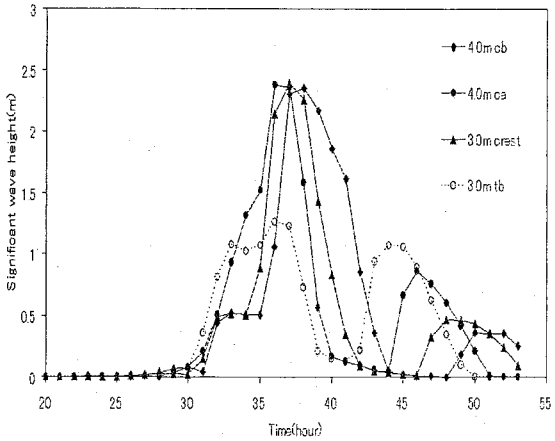

Fig. 4.14. The time history of the significant wave height at the station of *B*.

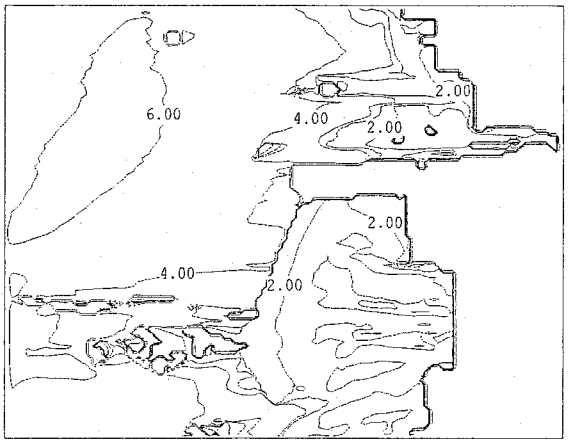

Fig. 4.15. The spatial distribution of the significant wave height at 37 hours (the still water level).

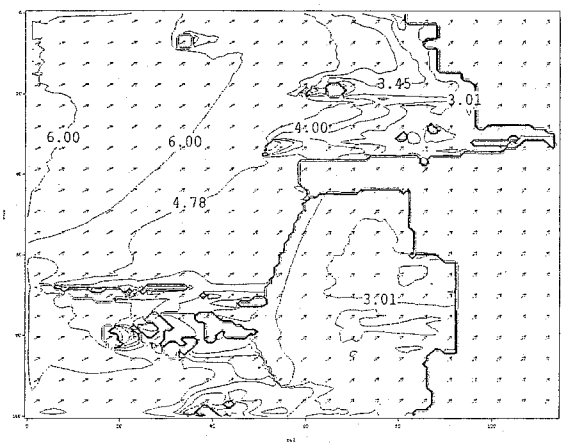

Fig. 4.16. The spatial distribution of significant wave height and wind at 37 hours (the tidal amplitude; 4.0m, the tidal phase; *crest*).

4.5. Discussion

4.5.1. Effect of tide on storm surge

The storm surges induced by the combination of the wind, atmospheric pressure and radiation stress are computed by the coupling and non-coupling model. Fig. 4.17 shows the comparison of the maximum storm surges between the coupling model (MSW-CR) and the non-coupling model (MSW-NCR). The magnitude of MSW-CR was higher than that of MSW-NCR in cases of *mcb* (Amplitude = 4.0m), *trough* (Amplitude = 1.0m) and *ta* (Amplitude = 1.0, 2.0 and 4.0m) of the

transverse axis. However, it was estimated that MSW-CR became lower than MSW-NCR over all from the result of the coupling model. For Amplitude = 2.0, 3.0 and 4.0m, the magnitude of MSW-CR decreased on the spring tide as well as on the neap tide, but for Amplitude = 1.0m it increased. All maximum storm surges computed by the coupling model except cases of '*mcb* and *ta*' for Amplitude = 2.0, 3.0 and 4.0m became lower than those computed by the non-coupling model. As the tidal amplitude became higher, the difference of storm surges between the coupling and non-coupling model became larger. Hence, the large tidal variation highly affected the storm surge. The relation between both should be dependent as well.

The maximum storm surge at each case was examined during the storm event and plotted in Fig. 4.18. The illustration was inserted in each graph to indicate the tidal phase encountering the maximum storm surge. In the case of (a) *mcb*, the maximum storm surge level for Amplitude = 4.0m was particularly higher than the others. In the cases of (b) *cb*, (d) *ca*, (e) *mca* and (h) *ta*, the magnitudes of MSW-CRs were almost identical to MSW-NCR. In cases of (c) *crest*, (f) *tb* and (g) *trough*, MSW-CRs, however, tended to decrease as the tidal amplitude became higher. The highest MSW-CR was produced 3.91m high for Amplitude = 4.0m in (a) *mcb* of Fig. 4.18, while MSW-NCR was 3.06m. Its change ratio of MSW-CR to MSW-NCR was 1.28 times. Therefore, the large tidal variation significantly affected on the storm surge level. However, the relation between both should result in the decay of the magnitude in the storm surge.

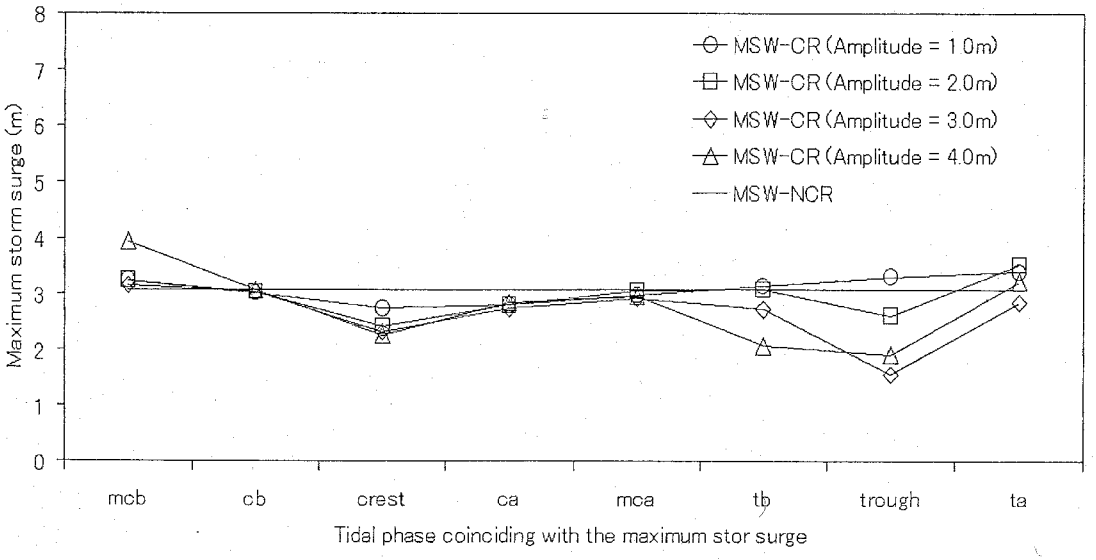

Fig. 4.17. The comparison of the magnitudes in the maximum storm surges relating to tidal phases at the station of *B* (MSW; the maximum storm surge, CR; the coupling model, NCR; the non-coupling model).

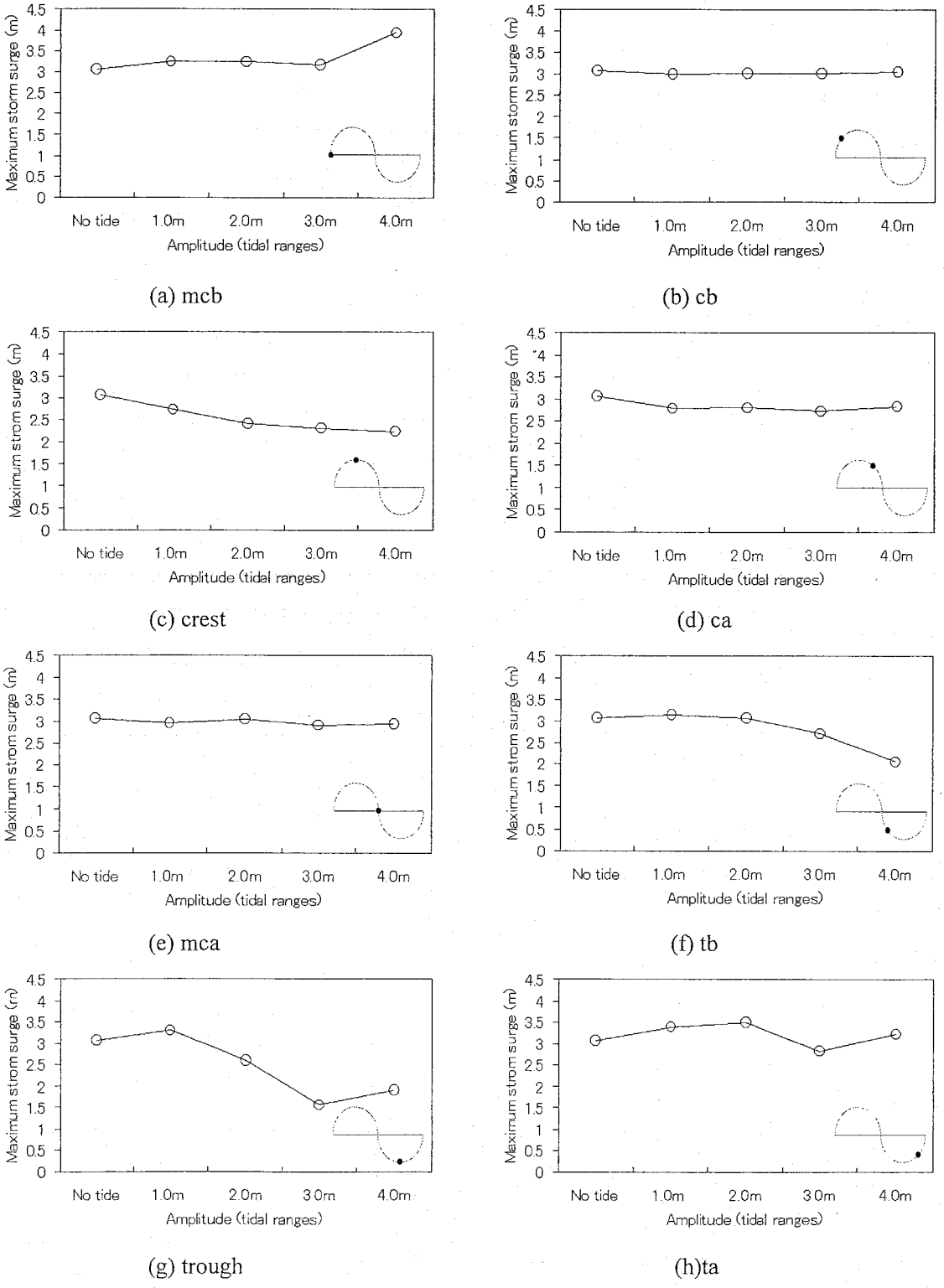

Fig. 4.18. The comparison of the variation of MSW occurred at each tidal amplitude associated with the tidal phase (MSW; the maximum storm surge, no tide; non-coupling model).

4.5.2. Effect of tide on set-up

In this section how the tidal variation affects on the set-up induced by the radiation stress will be examined. As described at section 4.4.3, the timing of the occurrence in the maximum set-up induced by the only radiation stress may be different from that in the maximum storm surge induced by the combination of the wind, atmospheric pressure and radiation stress at the station of *B* in Fig. 4.10. The wave set-up was calculated by Eqs. (4.3) and (4.4) with the tidal variation and on still water level, respectively.

Fig. 4.19 shows the comparison of the maximum set-up computed by the non-coupling and coupling model. The maximum set-up computed by the coupling model (MSR-CR) became lower than that of non-coupling model (MSR-NCR) except cases of '*ca* and *mca*' for Amplitude = 1.0 and 2.0m, and '*tb*' for Amplitude = 1.0m. The decay of the maximum wave set-up should be significant at Amplitude = 3.0 and 4.0m as shown in Fig. 4.19. The highest maximum set-up was computed as about 0.2m in the case of '*ca*' for Amplitude = 1.0m. Fig. 4.20 shows the comparisons of the variations in the maximum set-ups at each tidal amplitude associated with the tidal phase. It was clearly shown that the maximum set-up level occurred as 2.0m in (d) *ca* for Amplitude = 1.0m. But the magnitudes of the others decreased as the tidal amplitude became higher at each tidal phase. The highest MSR-CR and MSR-NCR were evaluated as 0.2 and 0.08m, respectively. The difference of both was 0.12m. Although the magnitude of the peak in the wave set-up was smaller compared to that in the storm surge, its change ratio of 1.5 times for the set-up became larger than 1.27 times for the storm surge. Therefore, it was expected that the tidal variation significantly influenced on the magnitude of the set-up level.

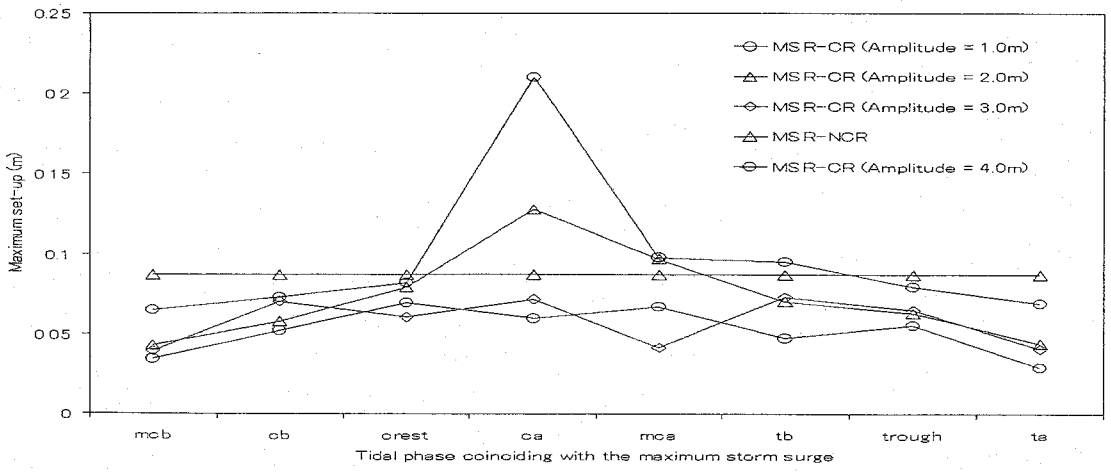

Fig. 4. 19. The comparison of the magnitudes in the maximum set-ups relating to tidal phases at the station of *B* (MSR-CR; the coupling model, -NCR; the non-coupling model).

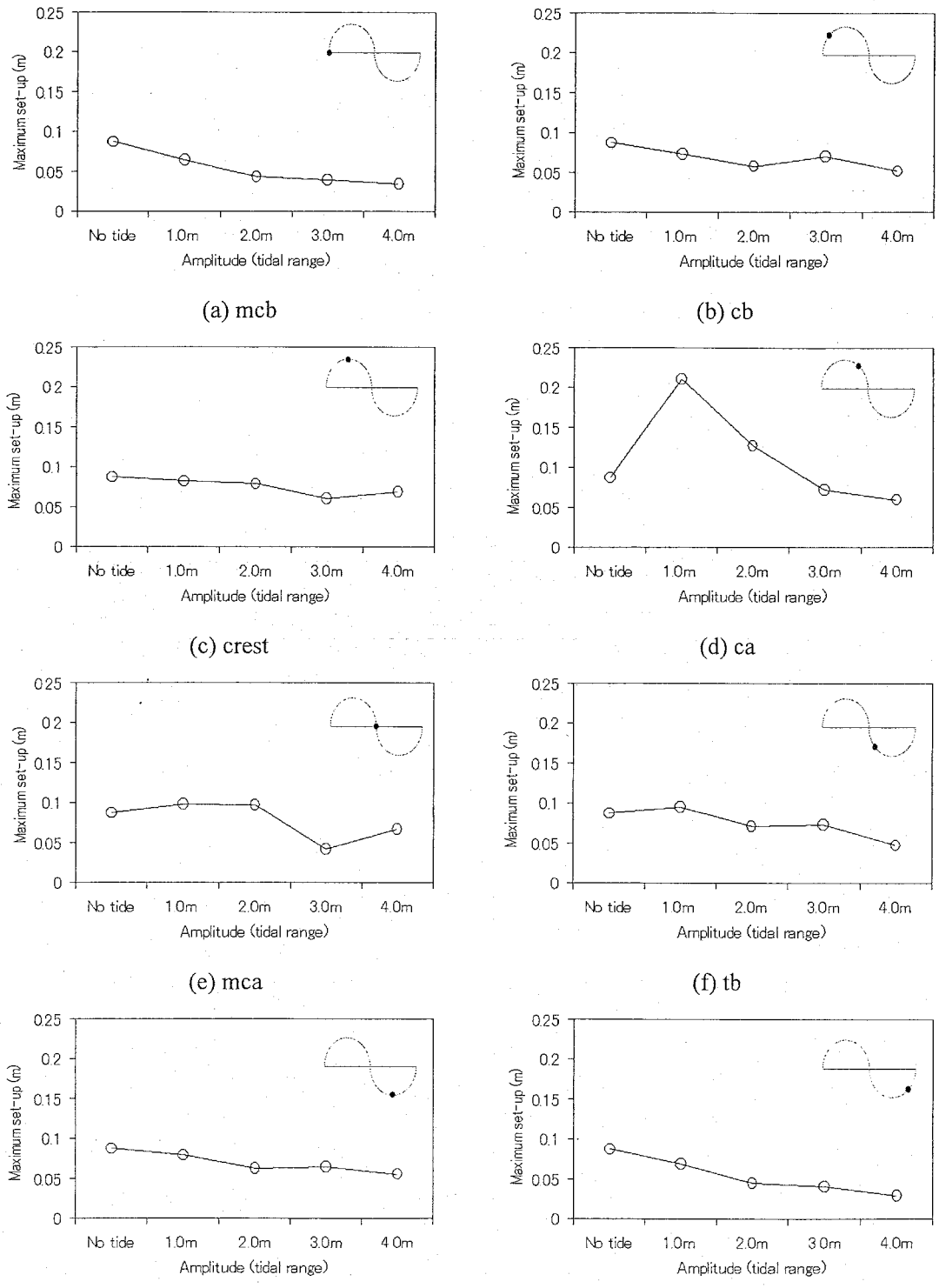

Fig. 4. 20. The comparison of the variation in MSR occurred at each tidal amplitude associated with the tidal phase (MSR; the maximum set-up, no tide; the non-coupling model).

4.5.3. Worst case due to large tidal variation

In the section 4.5.1 and 4.5.2, the maximum storm surge and wave set-up computed by the coupling model were investigated and significantly affected by the large tidal variation in the comparison with the non-coupling model. In addition, the timing of the generation in the peak of the storm surge may not coincide with that of the set-up from the result of the computation. In this section, it is investigated when the worst case occurs, which is explained by the generation of the maximum water level during the typhoon event In order to examine it, the coupling model, the coupling model and the non-coupling model were carried out as follows:

$\eta_{tide+ws+rs+pr}$: the maximum water level computed by the coupling model (WSCP).
$\eta_{ws+rs+pr} + \eta_{tide}$: the storm surge computed by the non-coupling model + the tide computed by the tidal simulation (WSNCP)

where the WSNCP is computed such a way that the storm surge computed by the non-coupling model adds to the tide as a function of time. For the resident near the coast, it is necessary that the information of the worst case should be provided in order to save and protect the property against the inundation and wave model-up.

From now on, the worst case will be discussed comparing WSCP with WSNCP as mentioning its storm surge at the station of *B*, which the water depth is 1.17m. *No tide* in the transverse axis of Fig. 4.21 represents the non-coupling model. The illustration was inserted to indicate the timing of the generation in the maximum storm surge coinciding with the tidal phase. WSNCP was overestimated than WSCP overall in the case of the tidal amplitude of 4.0m shown in Fig. 4.21. In addition, the difference between WSCP and WSNCP became larger when the tidal amplitude became higher. Especially, it is shown that the maximum difference of both appeared in the case of the tidal amplitude of 4.0m in (c), which the tidal phase was the crest of the spring tide. However, in this case, the maximum storm surge was smaller than the others. On the other hand, although the variation of maximum storm surge was not shown as changing the tidal amplitude, the difference between WSCP and WSNCP appeared in (a), (b), (d) and (e). The pattern of the increase in the difference between WSCP and WSNCP was apparently shown, when tidal phases indicated above or on the mean water level as shown in (a), (b), (c) and (d).

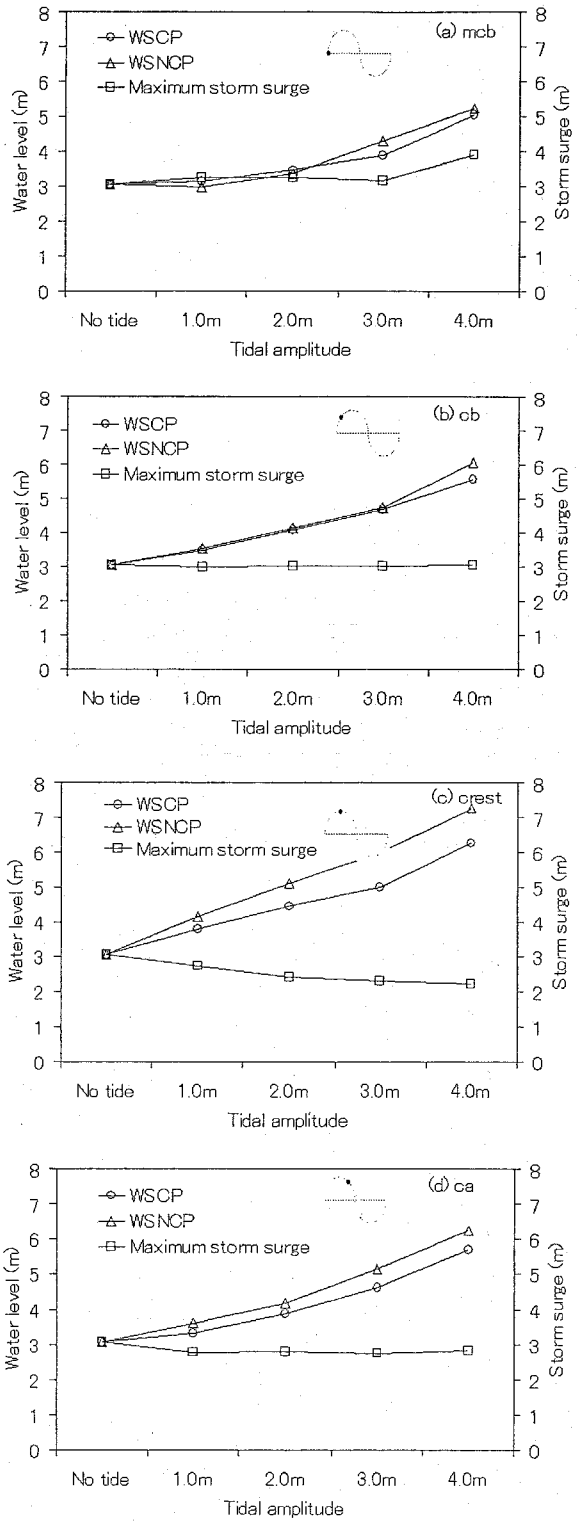

Fig. 4. 21. The comparison of the maximum water levels computed by the coupling model (WSCP) and non-coupling model (WSNCP) associated with the tidal amplitude at the station of *B* (the depth; 1.17m).

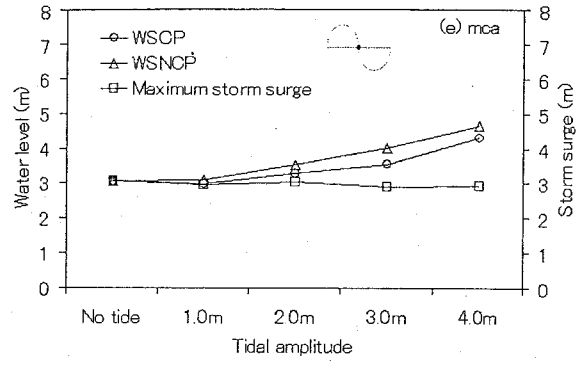

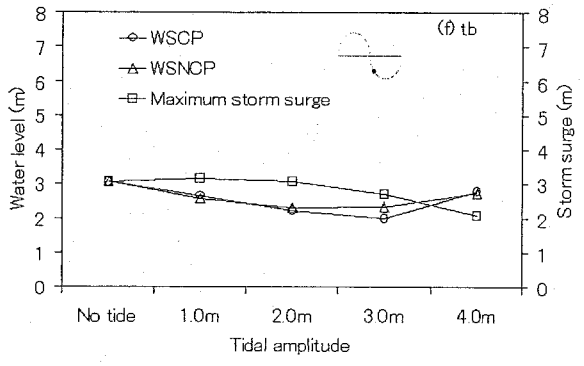

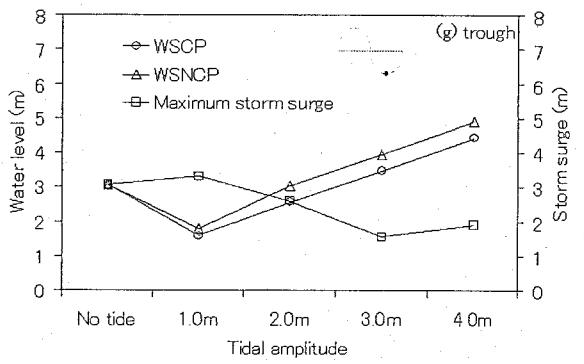

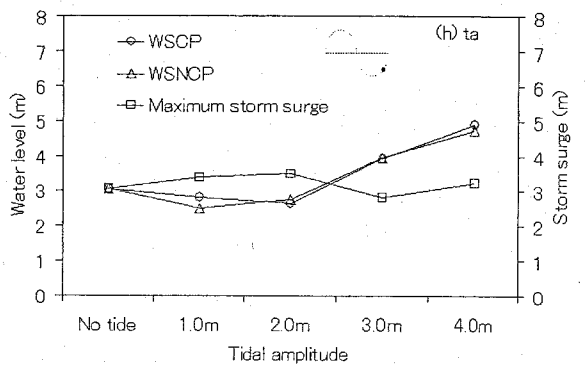

Fig. 4.21. (Continued).

When tidal phases indicated below the mean water level, the difference between WSCP and WSNCP was also shown in (f), (g) and (h). But their differences were insignificant unlike the rest. In (g), the difference between WSCP and WSNCP was significant as the tidal amplitude increased. The maximum storm surge was larger than WSCP and WSNCP in the case of the tidal amplitude of 1.0m in (g). Because the water depth was 1.17m at the observation station of *B*, the water depth was maintained even though the tidal phase was on the neap tide and then, the maximum storm surge occurred. However, in the case of the tidal amplitude of 2.0, 3.0 and 4.0m, the tidal flat was exposed at the station of *B* as well as the vicinity. As a result of that, it was expected that the maximum storm surge was smaller than WSCP and WSNCP.

Figure 4.22 (a) shows the comparison of the maximum water levels between the coupling and non-coupling model. The maximum water levels computed by the coupling model were smaller than that of non-coupling model in cases of *mcb* to *mca*, but it was opposite in cases of *mca* to *ta*. The difference of the maximum water levels between the coupling and non-coupling model appeared again in Fig. 4.22 (b) and the pattern of the variation in the difference in Fig. 4.22 (b) was similar to that in Fig. 4.22 (a). That is to say, the profile of the maximum water level variation at each tidal amplitude was very similar to the sinusoidal curve with one period. In addition, the difference of the maximum water levels between the coupling and non-coupling model became larger, when the tidal amplitude became higher as shown in Fig. 4.22 (c) and (d). Moreover, the maximum water level computed by the coupling model became smaller than that computed by non-coupling model, when the tidal amplitude became larger. Among the maximum water levels computed by the coupling model, the highest maximum water level occurred as 6.3m in the case of crest and the tidal amplitude of 4.0m as shown in Fig. 4.22 (d). When the storm surge coincided with the crest of spring tide of 4.0m, the highest water level should occur at the moment.

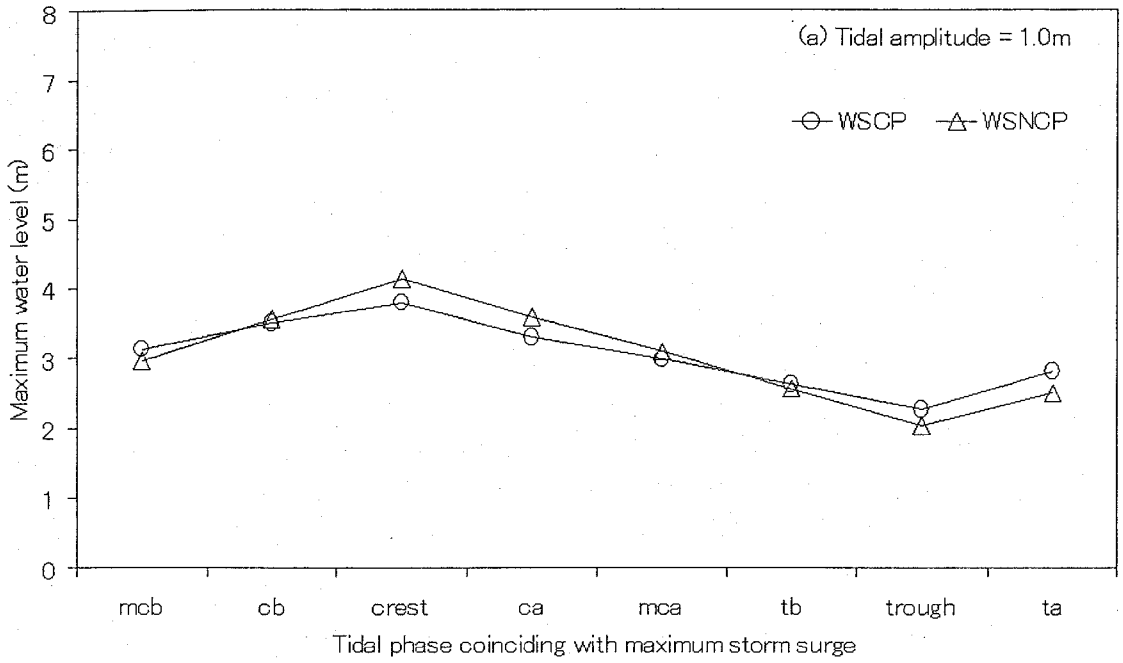

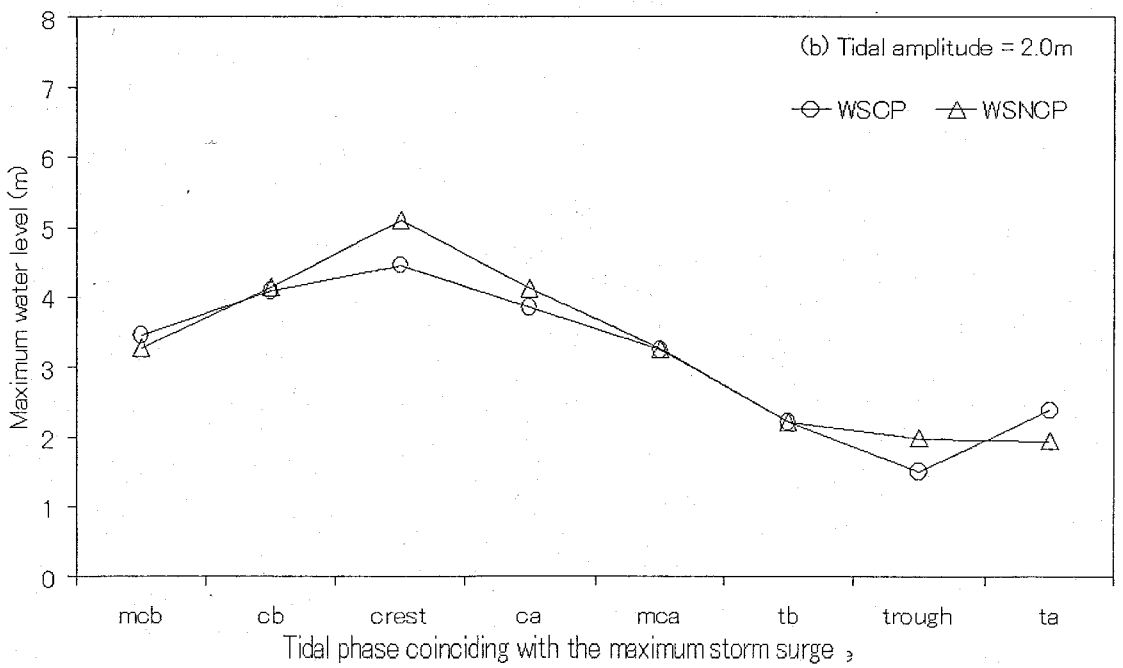

Fig. 4.22. The comparison of the maximum water level between the coupling model and non-coupling model associated with the tidal phase at the station of *B* (the depth; 1.17m, WSCP; the coupling model, WSNCP; the non-coupling model).

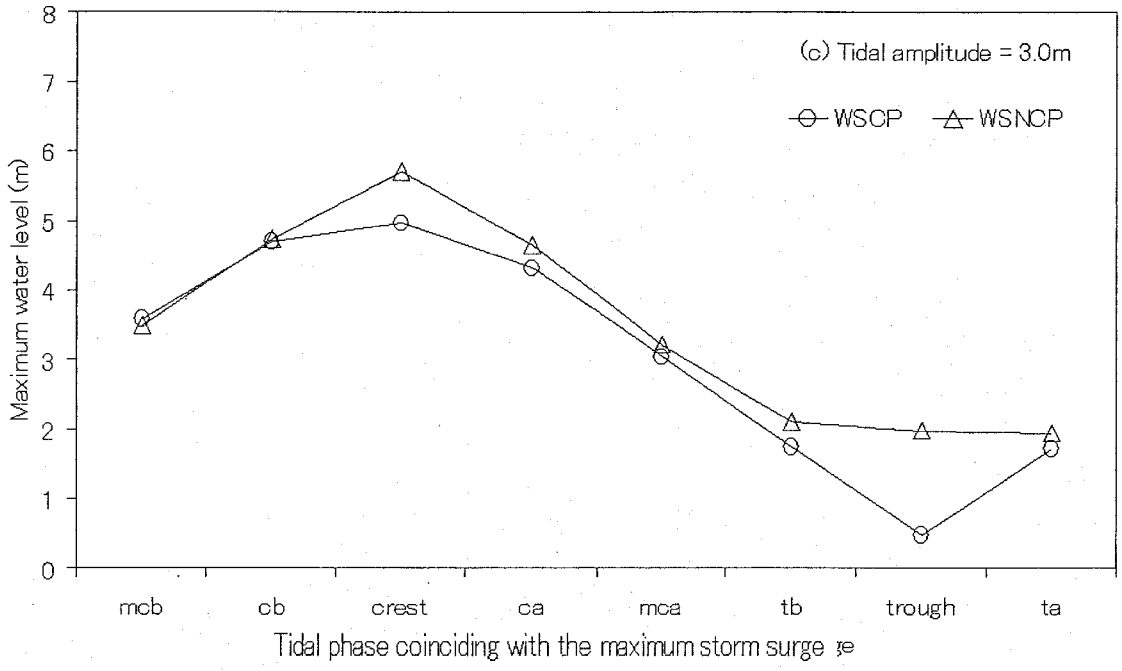

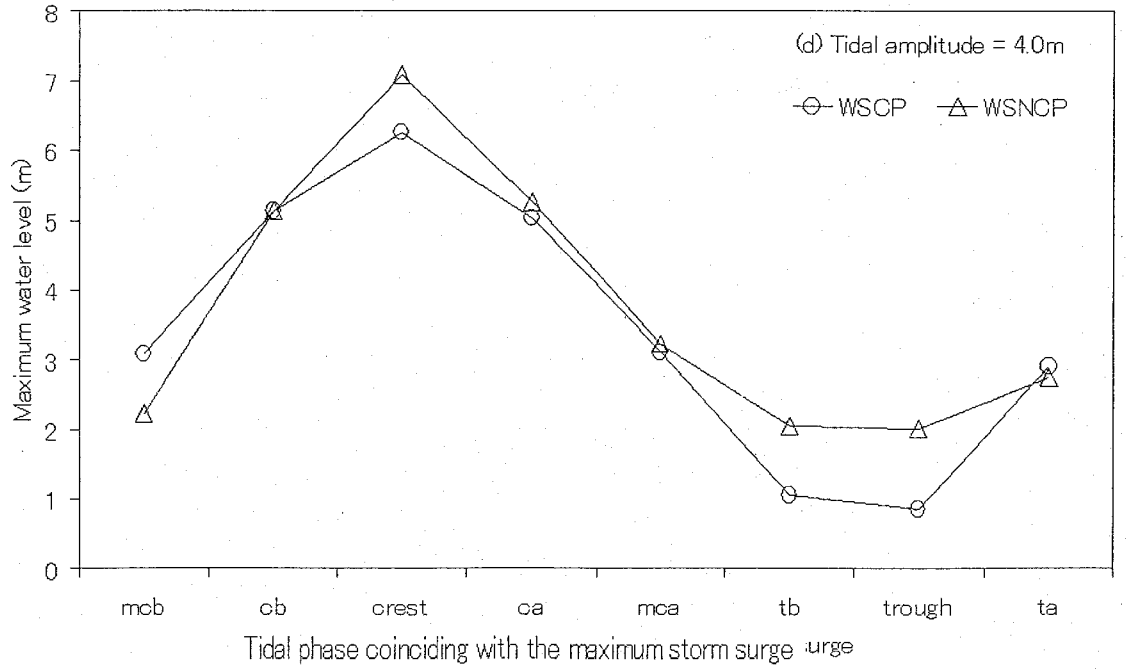

Fig. 4.22. (Continued).

Chpater 5

Hindcast of Typhoon 0603 (Ewiniar)

5.1. Typhoon 0603 (Ewiniar)

The hindcast of Typhoon 0603 (Ewiniar) was conducted to confirm the applicability of the coupling model. Typhoon 0603 (Ewiniar), which hit the western coastal sea of Korea in 2006, was selected to validate the hindcast simulation in comparison with the observation. As listed in Table 5.1, Typhoon 0603 (Ewiniar) was born on UTC 30 June in 2006 near 7.5°N 137.8°E The tropical storm born at UTC 1 July changed to the typhoon near 14°N 136°E at UTC 3 July. The typhoon moved northwestward, turned northeastward at UTC 9 July and hit the southwest of Korea on UTC 10 July in 2006 with the central atmospheric pressure of 975hPa. The typhoon passed through the middle of the western coastal region of Korea and disappeared on the East Sea (Japan Sea) at 11 July. The wind speed of 25m/s was recorded at the western coastal area of Korea. The typhoon remained the life loss and missing of 8 persons, and caused the inundation and the property damage of 600,000USD in Korea. Fig. 5.1 shows the track of Typhoon 0603 (Ewiniar). The storm surge simulation for the hindcast of Typhoon 0603 (Ewiniar) is conducted from 18:00 06 July to UTC 06:00 11 July 2006. In order to reproduce the wind and atmospheric field of Typhoon 0603 (Ewiniar), the atmospheric pressure data observed on the sea surface by Japan Meteorological Agency and Korea Meteorological Administration are employed. The

computational domain shown in Fig. 4.1 was again used. Fig. 5.2 shows the observation points of the wave and tide around Korean peninsula. Table 5.2 shows the status of observation points. Three points were chosen for the wave and five points were used for the storm surge. The stations of (3) for the wave and (2) for the tide were located in the domain 4, while the other stations were located in the domain 1. The resolutions of about 300m to 10km were employed to produce the wave and the storm surge. Ministry of Maritime Affairs Fisheries (MMAF) in Korea provides the observation data on the internet and is available to access at any time.

Table 5.1. Track of Typhoon 0603 (Ewiniar).

TIME(UTC)	Latitude(°N)	Longitude(°E)	Pressure(hPa)
2006070700	208	1276	950
2006070706	214	1274	950
2006070712	221	1271	950
2006070718	225	1265	950
2006070800	231	1266	950
2006070806	241	1263	950
2006070812	251	1261	955
2006070818	263	1259	955
2006070900	275	1258	960
2006070906	293	1258	960
2006070912	306	1258	965
2006070918	316	1257	965
2006071000	336	1261	975
2006071006	355	1265	985
2006071012	368	1270	990
2006071018	382	1283	994
2006071100	402	1314	996

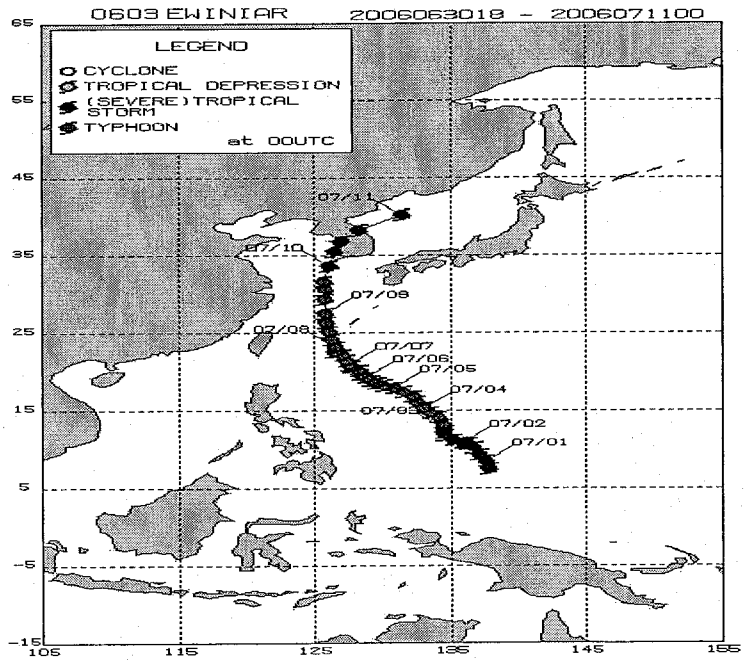

Fig. 5.1. The track of Typhoon 0603 (Ewiniar).

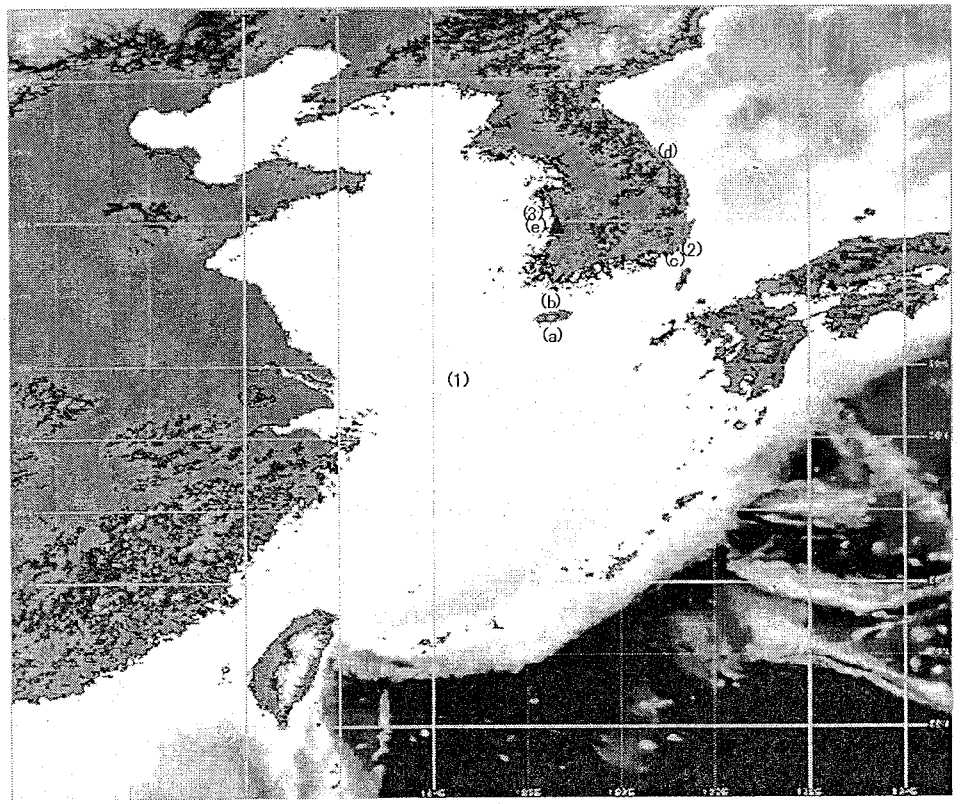

Fig. 5. 2. The observation points around Korea Peninsula (wave; (1), (2) and (3), tide; (a), (b), (c), (d) and (e)).

Table 5.2. The status of the stations.

No.	Station	Latitude(N)	Longitude(E)	Observation	Domain No.
(1)	Iedo	32-07-23	125-10-57	Wave	1st
(2)	Pusan	35-07-47	129-08-16	Wave	1st
(3)	Sucheon	36-07-12	126-32-24	Wave	4th
(a)	Seoguipo	33-14-12	126-33-49	Tide	1st
(b)	Jeju	33-31-27	126-32-43	Tide	1st
(c)	Pusan	35-05-35	129-02-15	Tide	1st
(d)	Sokcho	38-12-16	128-35-48	Tide	1st
(e)	Gunsan	35-58-06	126-37-36	Tide	4th

5.2. Discussion and result

The storm surge, wave and tide generated by Tyhpoon 0603 (Ewiniar) were hindcasted for 5 days starting from UTC 18:00 on 06 July by the coupling model. Before the coupling procedure started, the tide was first calculated to distribute the steady state through all domains. Once the tide was sufficiently steady, the coupling model begun to calculate the storm surge and wave propagation with the tide imposed on open boundary (Kim et al., 2006a, b). As listed on Table 5.2, the results of coupling model at points (1), (2), (a), (b), (c) and (d) were obtained in the first domain. On the other hand, the results at points (3) and (e) were achieved in the fourth domain. The observation data such as the wind, atmospheric pressure, significant wave height and storm surge are obtained from National Oceanographic Research Institute (NORI) in Korea.

5.2.1. Meteorological data

The results obtained from the hindcast simulation of Typhoon 0603 (Ewiniar) on the first and fourth domain were compared with the observation and these provided the information of the storm surge at the coastal region where the typhoon passed through. Before the results of the simulation were discussed, the meteorological data were described with the comparison with the observation.

Figure 5.3 shows the meteorological data observed at Iedo of (1) as shown in Fig. 5.2. The maximum depression of the atmospheric pressure at the center of Typhoon 0603 (Ewiniar) was about 968 hPa. On the other hand, the storm surge simulation produced that of 978 hPa.. In addition to the magnitude of the atmospheric pressure, the maximum depression of the simulation generated later about 3hours. From this fact, the difference of the storm surge

between the hindcast prediction and the observation might occur more than 0.1m near Iedo, because it is assumed that 1 hPa = 1cm. Unfortunately, the observation of the wind velocity could not be done until 12:00 10 July in 2006, but started after that. Unlike the wind speed, the wind direction had been observed during the storm event. The direction of wind was relatively good agreement with the observation when the typhoon only passed through Iedo. The observed wind direction was rapidly changed in comparison with the prediction before and after at 2:00 7 July.

Figure 5.4 shows the meteorological data observed at Pusan of (2) in the domain 1. It was estimated that the pressure of 996 hPa fairly produced by the simulation in comparison with the observed atmospheric pressure of 993 hPa at 13:00 7 July. Although the observed wind speed showed the local change in its direction, the overall predicted wind speed was well produced by the simulation. Especially, the maximum wind speed of 18m/s in the simulation was good agreement with the observation. Until 0:00 10 July, the rapid change of the wind direction occurred. When the typhoon passed through around Pusan located on the right side of its track, the wind direction changed to blow from the east toward the west.

The predicted meteorological data at Sucheon had the highest resolution of about 300m in the grid size as shown in Fig. 5.5. The time lag of the generation in the maximum depression of the pressure was about 6 hours. Typhoon model produced the overestimated maximum depression of the pressure. In addition to the pressure, the predicted wind speed was underestimated before 14:00 10 July and overestimated after that compared to the observation. The overall change of the wind direction in the computation relatively agreed with the observation before 18:00 10 July, but was in disagreement with the observation after that. The observed direction was changed from 270° to 90°, but the computed direction of 270° was not changed after 18:00 10 July.

Until now on, the meteorological data in the computation was compared with the observation at three station of Iedo, Sucheon and Pusan. At the early stage of the hindcast simulation when the typhoon was on deep sea, the discrepancy between the observation and the computation highly occurred.

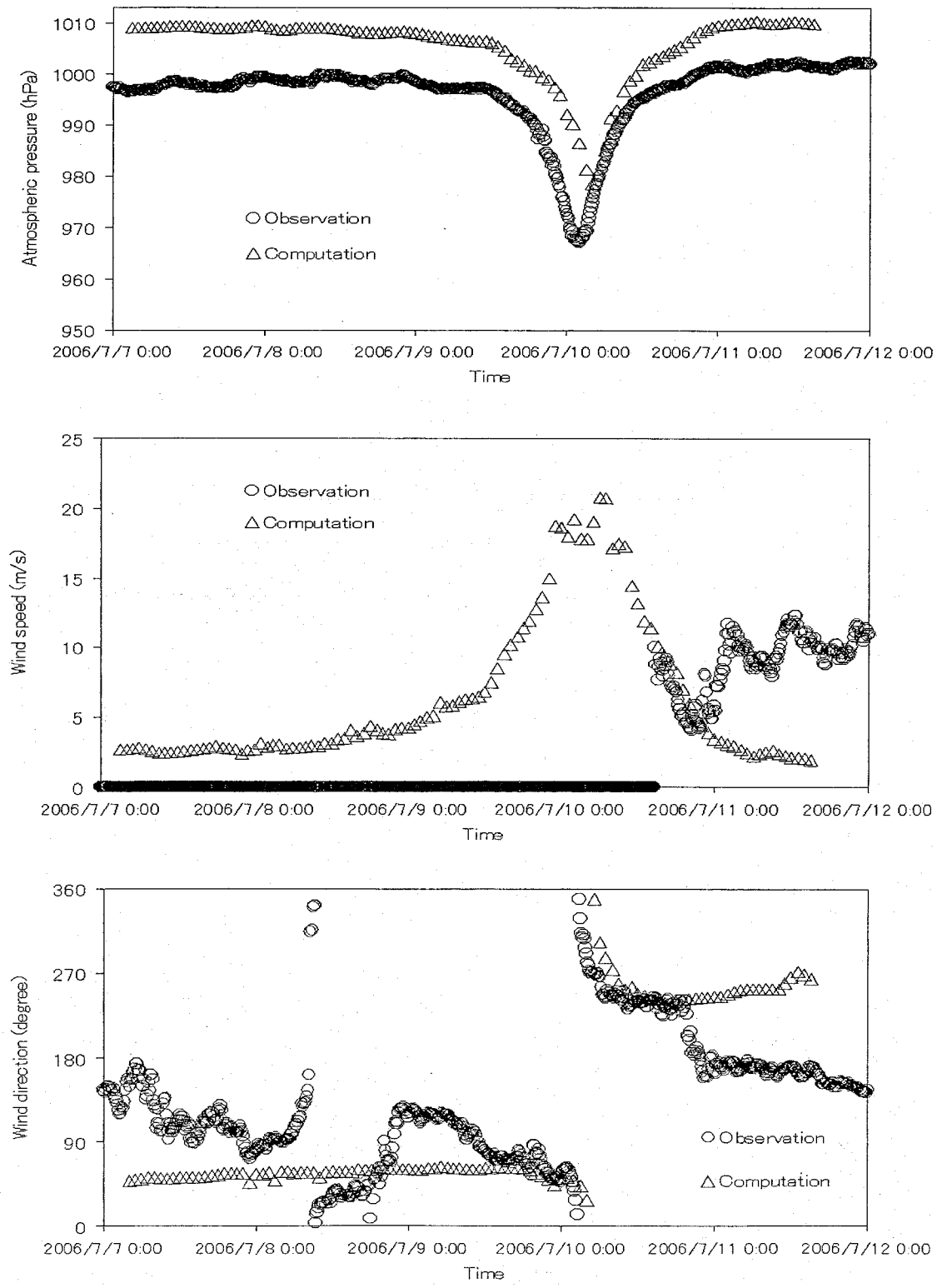

Fig. 5.3. The meteorological data observed at Iedo of (1) (Upper; the atmospheric pressure, middle; the wind speed, lower; the wind direction).

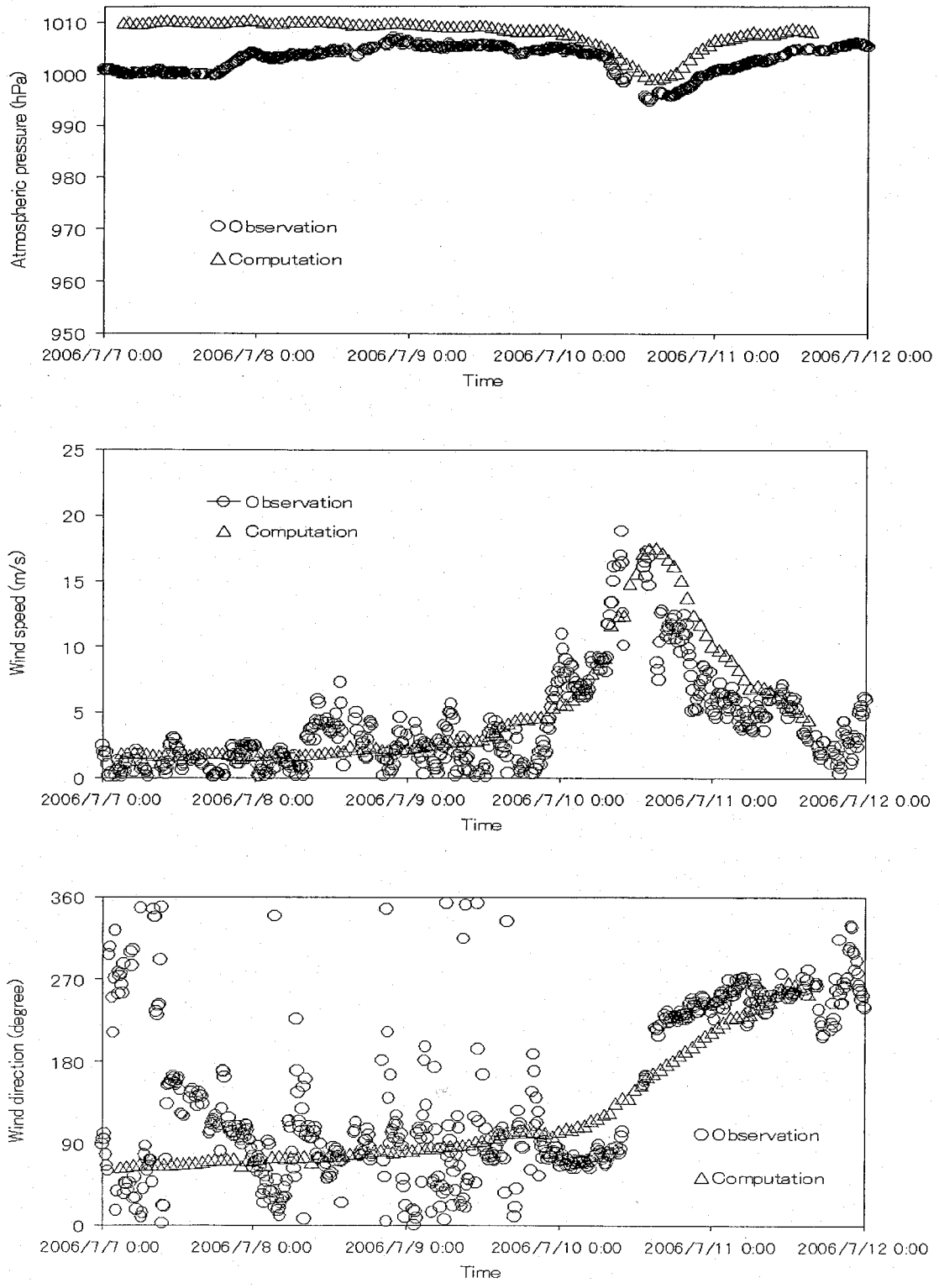

Fig. 5.4. The meteorological data observed at Pusan of (2) ((Upper; the atmospheric pressure, middle; the wind speed, lower; the wind direction).

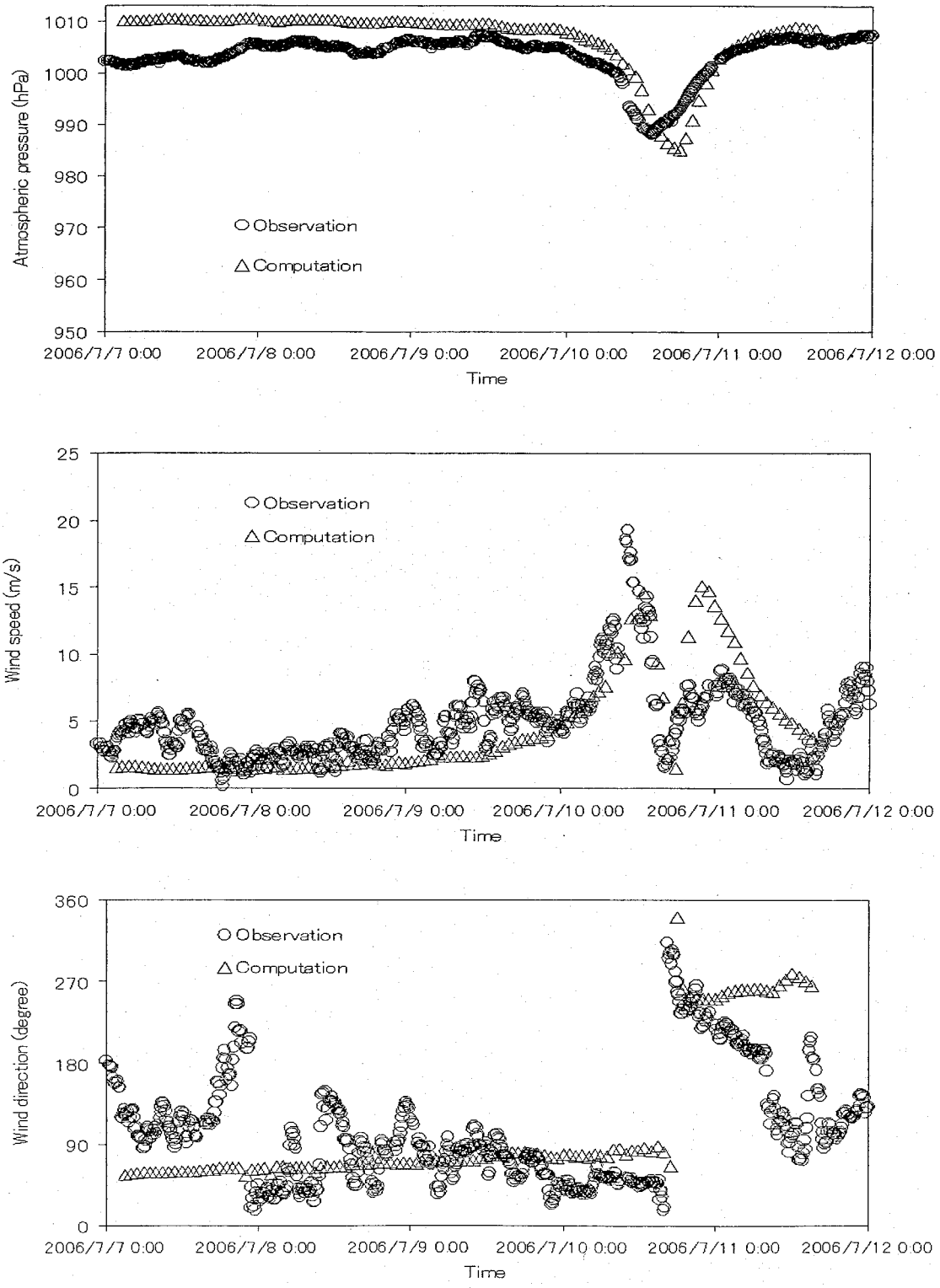

Fig. 5.5. The meteorological data observed at Sucheon of (3) (Upper; the atmospheric pressure, middle; the wind speed, lower; the wind direction).

5.2.2. Significant wave height

The significant wave height computed by the coupling model was compared with the observation data. In the study, three observed data were obtained from NORI in Korea. Fig. 5.6 shows that the significant wave height was observed at Iedo of (1) as shown in Fig. 5.2. The significant wave height of 6m in the computation showed the good agreement with the observation, until it developed to its peak. After its peak, the observation was rapidly decreased. Although those peaks of the observation and the computation significantly agreed, they showed the discrepancy after 0:00 10 July. Based on the wind speed and direction in Fig. 5.3, it was expected that the observed wind speed and direction should resulted in those discrepancy between the result of the computation and the observation, even though the wind speed was not observed actually.

Although the predicted meteorological data showed the good agreement with the observation at Pusan of Fig 5.7, the peak of the observed significant wave height was 7m high. On the other hand, the predicted peak was 4m. The discrepancy between them was quite large. It was estimated that the computation of wave could not produce the shoaling, because of the resolution of 10km in the computational domain 1. Therefore, waves in the computation could not propagate sufficiently from the deep to coastal sea, even though the wind speed and direction computed by the coupling model was well produced at Pusan.

The significant wave height was observed less than 0.7m at Sucheon as shown in Fig. 5.8. Although the observed wind speed of about 20m/s was not small at Sucheon compared to at Pusan and Iedo, the wind direction, blowing from the land toward the sea, resulted in the small significant wave height developed by the wind. On the other hand, the significant wave height was predicted about 1.0m and overestimated in comparison with the observation after 0:00 11 July.

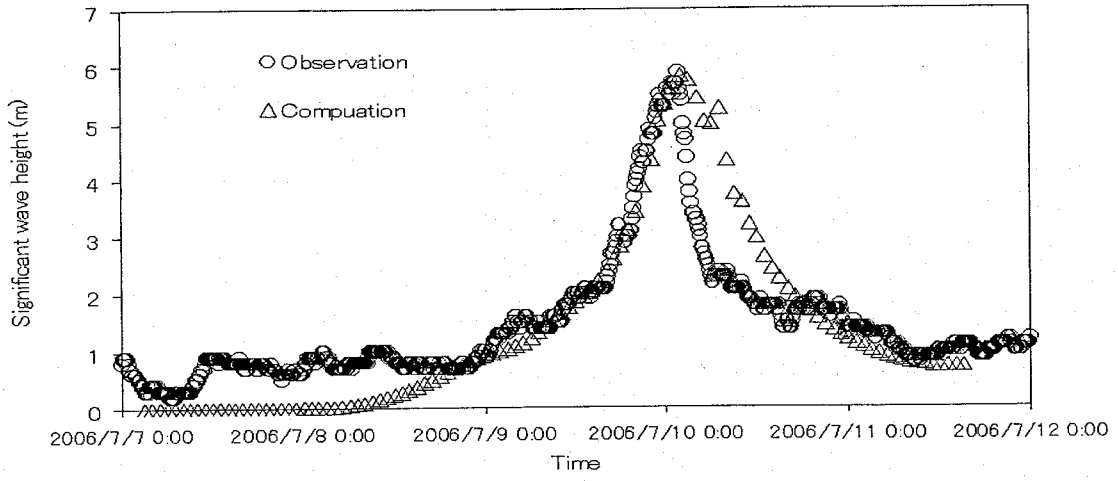

Fig. 5.6. The significant wave height of the observation and computation at Iedo of (1).

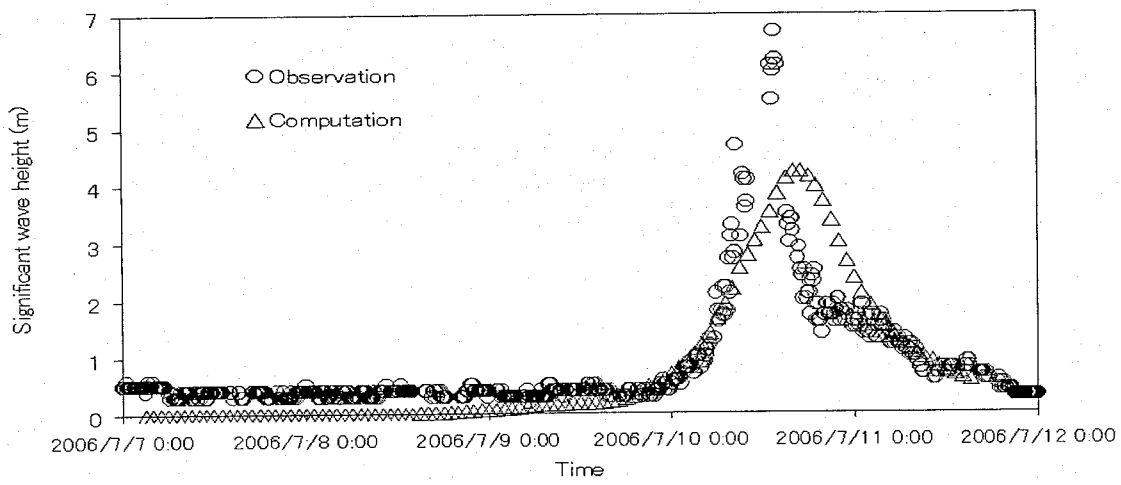

Fig. 5.7. The significant wave height of the observation and computation at Pusan of (2).

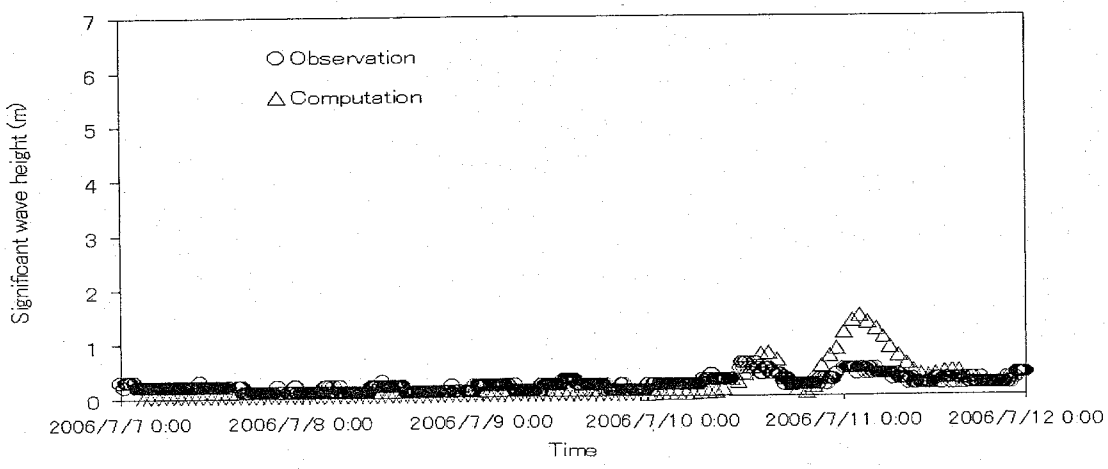

Fig. 5.8. The significant wave height of the observation and computation at Sucheon of (3).

5.2.3. Storm surge

At previous sections 5.2.1 and 5.2.2, it was discussed that the result of computation in the meteorological data and the significant wave height in the comparison with the observation. Although the prediction at Pusan agreed well with the observation for the meteorological data, the hindcast simulation could not produced sufficiently the significant wave height compared to the observation. On the other hand, the peak of the significant wave height in the computation agreed well with the observation at Iedo where the wind speed could not be observed. In addition, the result of hindcast simulation did not agree with the observation for the peak of significant wave height and meteorological data at Sucheon where the center of Typhoon 0603 (Ewiniar) passed through.

Jeju and Seoguipo of (b) and (a) as shown in Fig. 5.2 are located in the Jeju island. Seoguipo is located in the south coast of Jeju island, while Jeju is in the north coast of Jeju island. Seoguipo and Jeju are first the observation points faced to the effect of the typhoon moving to the Korean Peninsula except Iedo of (1). At the early stage of the generation in the storm surge due to Typhoon 0603 (Ewiniar), the water level started to be disturbed at Seoguipo facing to the open sea. It was also expected that the wind blew from the land as the typhoon approaches. When the typhoon arrived at Jeju island, the maximum storm surge should occur at Jeju and Seoguipo at the same time as shown in Fig. 5.9 and 5.10, even though the tides of the computation were larger than the observation. In addition, the maximum storm surge generated at both was similar as approximately 0.5m as shown in Fig. 5.14.

On the other hand, it was expected that the storm surge generated at Gunsan of (c) in Fig. 5.2 was overestimated by the hindcast simulation in comparison with the meteorological data observed at Sucheon as shown in Fig. 5.5. Sucheon of (3) is very close to Gunsan of (c) as shown in Fig. 5.2. The storm surge started to apparently generate after 12:00 10 July and its peak occurred around 22:00 10 July as shown in Fig. 5.13. The atmospheric pressure and the wind speed were overestimated and then, the wind blew from the sea to the land by the computation. Therefore, the impractical storm surge was predicted by the combination of three factors such as the atmospheric pressure, the wind speed and direction.

In the case of Pusan located in the right side of its track, the water level computed by the simulation agreed well with the observation, even though the significant wave height of the computation was underestimated as 50% of the observation. Although the computed meteorological data agreed well with the observation, the hindcast simulation computed the

reasonable water level at Pusan as shown in Fig. 5.11.

In the case of Sokcho of (d) in Fig. 5.2, the track of Typhoon 0603 (Ewiniar) passed through Sokcho and the water level increased and oscillated as shown in Fig. 5.12. The wind should blow from the sea to the land, because the wind around the typhoon blew into its center. However, the water depth in the East Sea (Janpan Sea) is so deep that the magnitude of the storm surge becomes smaller. Additionally the reason was that the magnitude of the typhoon was weaken when passing through Sokcho.

Fig. 5.14 shows the maximum storm surge occurred at each station. The highest maximum storm surge generated as 0.55m at the station of Seoguipo, while the lowest maximum storm surge of 0.2m occurred at Pusan during the storm event of Typhoon 0603 (Ewiniar).

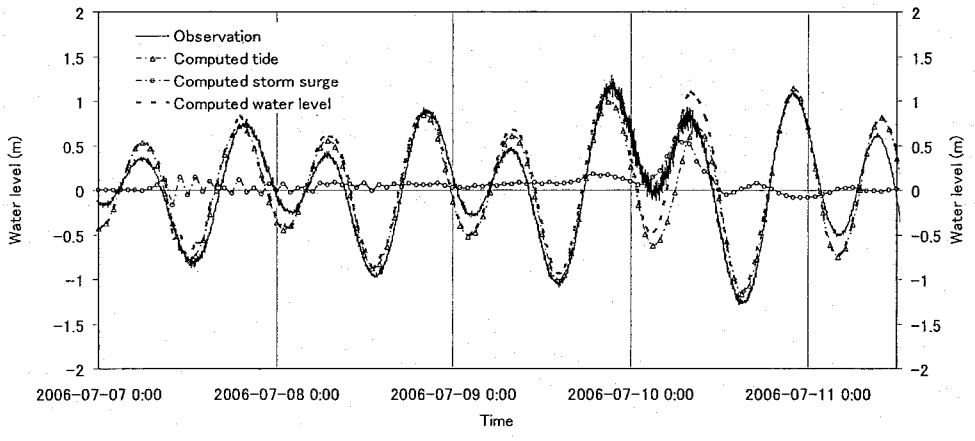

Fig. 5.9. The water level at Seoguipo of (a).

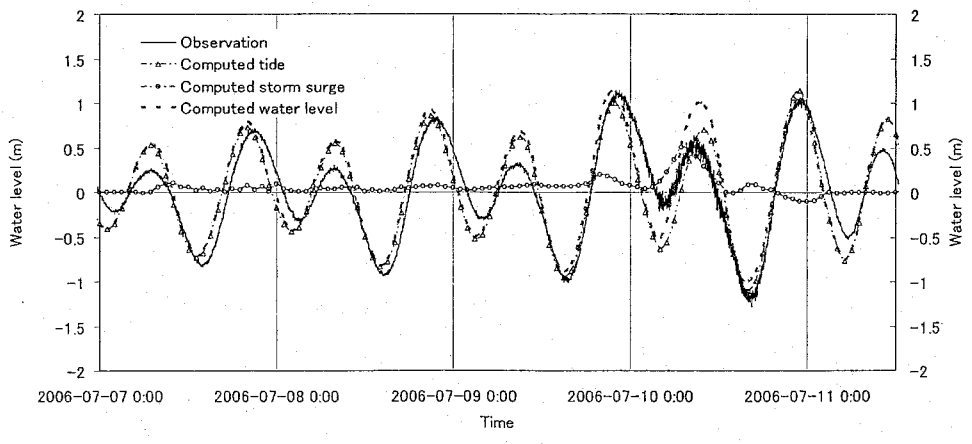

Fig. 5.10. The water level at Jeju of (b).

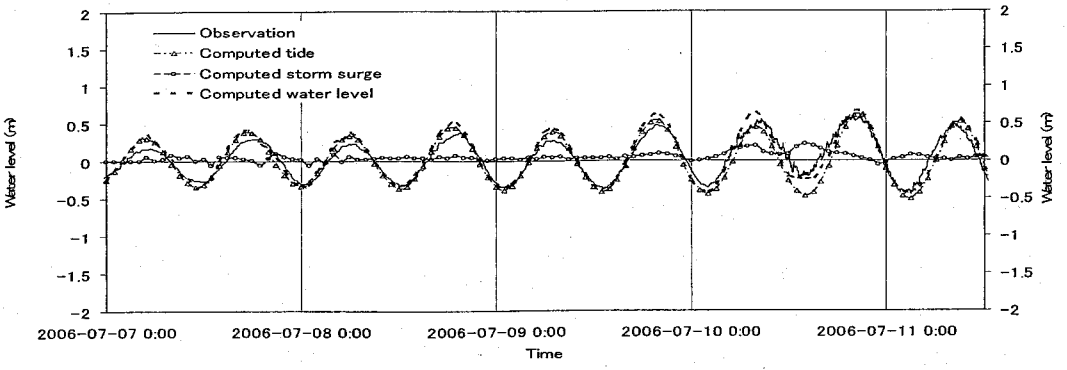

Fig. 5. 11. The water level at Pusan (c).

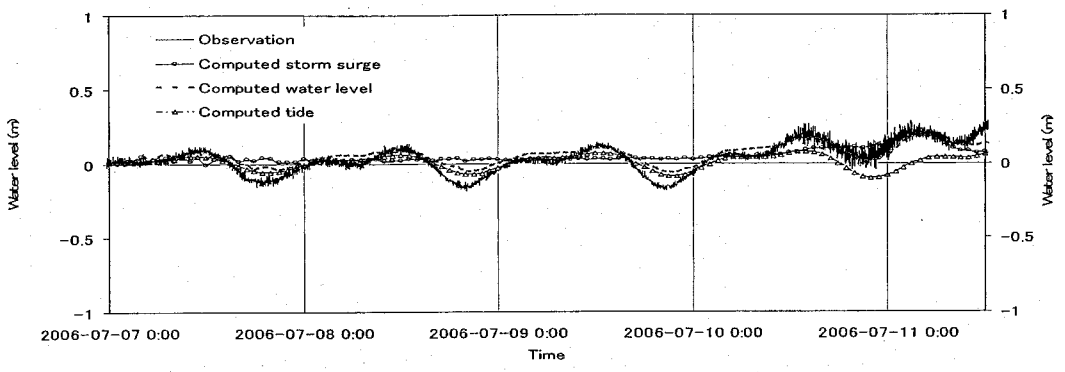

Fig. 5. 12. The water level at Sokcho (d).

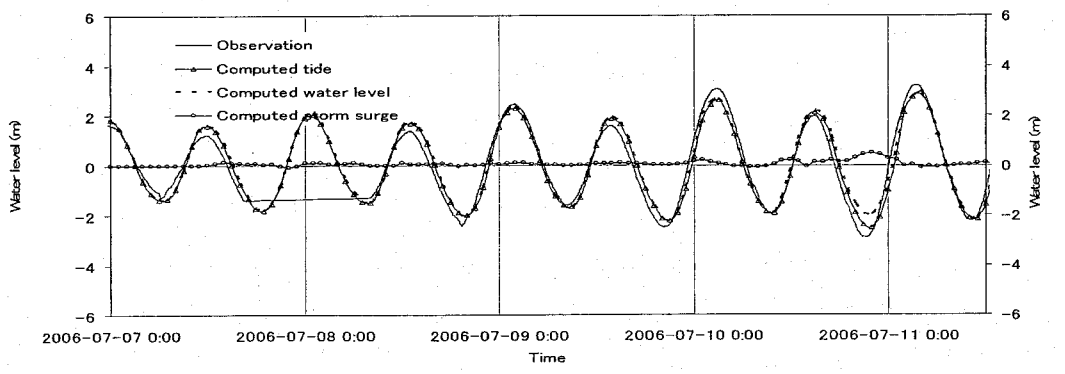

Fig. 5. 13. The water level at Gunsan (e).

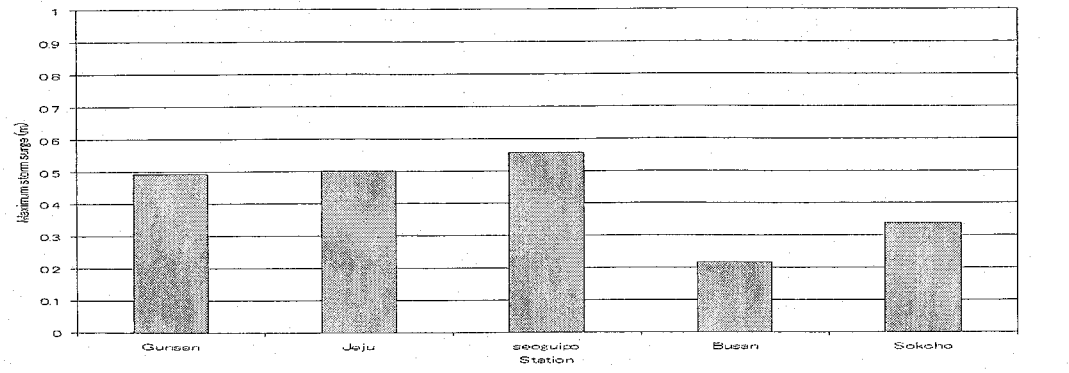

Fig. 5.14. The maximum storm surge occurred at each station.

Chapter 6

Conclusions

The present study was conducted to understand the behavior of the storm surge under the condition of the large tidal variation. To investigate it, the coupling model of the storm surge and wave model has been developed by applying the nested scheme from the deep to the coastal sea and allowing the hindcast simulation of the typhoon with the realistic tidal variation. The coupling model was applied to the numerical experiments of the simplified sea region. It was also applied the experimental hindcast simulation in the western coastal sea of Korea. Finally the simulation of Typhoon 0603 was conduced.

Main results in the study are as follows:

Chapter 2.
Development of alternative coupling model

The main coupling model is composed of the following sub models:

- Typhoon model
- Ocean tide model (for the only coarsest domain)
- Storm surge model
- Wave model (SWAN).

The typhoon model provides the atmospheric pressure field to the storm surge model and the wind field to the storm surge and wave model, which can be applied to the coastal area from the ocean as well as the tidal flat. The water level and currents predicted by the storm surge model are transferred to the wave model. The wave dependent drag coefficient and radiation stress are oppositely transferred to the storm surge model. To compute the high resolution in the computational domain, each sub coupling model is simultaneously parallelized by MPI (Massage Passing Interface) on Windows platform. The realistic tide is imposed on open boundaries by the ocean tide model. In addition, the wet and dry scheme is applied to the storm surge model.

Chapter 3.

Study for effect of tide on magnitude of storm surge under simplified condition

The coupling model was applied to the simplified bathymetry under the sinusoidal tide with a period of 12 hours and the maximum wind speed of 40m/s with Gaussian distribution. The simulation conditions are as follows:

- Bottom slope: 0.2, 0.1, 0.05, and 0.01.
- Tidal amplitude: 0, 0.5, 1.0, 2.0 and 3.0m
- Tidal phase: eight cases.

in which the encountering phase between the tide and storm surge was determined as follows: the peak of storm surge encounters the tide in same phase and with different phase lags of 1.5 hours. The observation point was selected near the coastal line. The coupling model was performed by imposing the tide. The non-coupling model was also carried out on the still water level.

In the case of the storm surge induced by the combination of the wind stress and radiation stress

1) The shallower the water depth is, the larger the peak of the storm surge becomes.
2) The peak of the storm surge computed by the coupling model became smaller than the maximum storm surge computed by the non-coupling model, when the storm surge coincided with the crest of higher tidal amplitude.

Therefore, the tidal variation significantly affected the storm surge.

In the case of the wave set-up induced by the only wave radiation stress

3) The shallower the water depth is, the larger the peak of the wave set-up becomes.
4) The peak of the wave set-up became higher on the shallow water when the tidal variation became larger.

Therefore, the peak of the wave set-up was highly changed and became larger by the effect of the large tidal variation on the shallow water. As a consequence, the wave set-up was very

sensitive on the shallow water and its variation was large due to the large tidal variation.

In the case of the water level:

5) The maximum water level computed by the coupling model was smaller than the total water level of the storm surge obtained by the non-coupling model and the tidal level achieved by the tidal simulation.

From the result, the summation of the storm surge and the tidal level is able to overestimate the maximum water level in comparison with it predicted by the coupling model.

Finally, the worst case defined by the generation of the highest water level during the wind event is as follows:

6) Although the maximum storm surge computed by the coupling model was smaller than the peak of the storm surge computed by the non-coupling model, the highest peak of the water level computed by the coupling model occurred when the peak of storm surge coincided with the crest of the spring tide with the tidal amplitude of 4.0m.

Chapter 4.
Study for effect of tide on magnitude of storm surge in the western coastal sea of Korea

The coupling model was applied to Gunsan region in the western coast of Korea. The hindcast simulation of the modeled typhoon with the same magnitude of Typhoon 0314 (Maemi) was carried out in order to investigate the effect of the large tidal variation on the storm surge and wave set-up.

- Tidal amplitude: 0, 1.0, 2.0, 3.0 and 4.0m
- Tidal phase: eight cases.

in which the tidal phase was determined as follows: the peak of storm surge coincides with the tide in same phase and with different phase lags of 1.5 hours. From the hindcast simulation, it was also investigated when the worst case defined by the generation of the highest water level

occurs in the western coast of Korea which the tidal variation is large. The observation point was located near the coastal line at Gunsan. The coupling model was conducted by imposing the tide, while the non-coupling model was carried out on the still water level.

In the case of the storm surge induced by the combination of the wind stress, radiation stress and atmospheric pressure:

1) The peak of the storm surge decreased as the tidal variation became large.
2) The maximum water level computed by the coupling model was smaller than the total water level of the tidal amplitude and the storm surge computed by the non coupling model.

Therefore, the large tidal variation reduced the peak of the storm surge in the western coastal sea of Korea.

In the case of the wave set-up induced by the only radiation stress

3) The variation of the peak in the wave set-up became larger and was significant when the tidal variation became larger.

It was not easy to characterize the variation of the peak of the wave set-up, however, the wave set-up with the tidal variation increased or decreased more than twice of the wave set-up on the predicted by the non-coupling model.

From the results of the computation, the highest water level occurred when storm surge coincided with the crest of the spring tide with the tidal amplitude of 4.0m. However, at that time, the maximum storm surge computed by the coupling run decreased in comparison with the peak of the storm surge on the still water level.

On the other hand, the water level computed by the coupling model became smaller than the total water level of the tidal amplitude and the storm surge computed on the still water level. In respect to the generation of the maximum storm surge, the large tidal variation reduced the magnitude of the maximum storm surge. In addition, the storm surge simulation should include the radiation stress on the shallow water because the maximum wave set-up highly varied, even though the magnitude of wave set-up was within 10% of the magnitude in the storm surge.

Finally, it is preferred to that the interaction of the storm surge and the tide should be considered

for the design of the water level at a region where the water depth is shallow and the large tidal variation exists.

Chapter 5.
Hindcast simulation of Typhoon 0603 (Ewiniar)

The storm surge caused by Typhoon 0603 was hindcasted to confirm the applicability of the coupling model. The wave and water level predicted by the coupling model showed relatively the good agreement with the observation. However, it was confirmed that the meteorological data of the computation did not agree with the observation at Sucheon among three stations. From the result of the hindcast simulation, the storm surge due to Typhoon 0603 occurred as approximately 0.5m at Jeju, Seoguipo, while it occurred as about 0.3 and 0.2m at Sokcho and Busan, respectively.

Future work

In the future work, the weather forecast model will be applied to forecast the meteorological data and to improve the accuracy of the coupling model through the study of its validity and efficiency. Additionally, if the topography of the land with the higher resolution is provided, the inundation simulation will be conducted applying to the coupling model. As described above, the integrated model will provide the important information of the forecasted storm surge to the resident at the coastal region.

REFERENCES

Battjes, J.A. and J.P.F.M. Janssen: Energy loss and set-up due to breaking of random waves, *Proc. 16th Int. Conf. Coastal Engineering*, ASCE, 569-587, 1978.

Booij, N., R. C. Ris, and L. H. Holthuijsen: "A third-generation wave model for coastal regions. Part 1, Model description and validation", *Journal of Geophysical Res.*, Vol.104, No.C4, pp. 7649-7666, 1999.

Cavaleri, L. and P. Malanotte-Rizzoli: "Wind wave prediction in shallow water:Theory and applications". *J. Geophys. Res.*, 86, No. C11, 10, 961-10,973, 1981.

Cheung, K.F., A.C. Phadke, Y. Wei, R. Rojas, Y.J.-M Douyere, C.D. Martino, S.H. Houston, P.L-F. Liu, P.J. Lynett, N.Dodd, S. Liao, E.Nakazaki: "Modeling of storm-induced coastal flooding for emergency management", *Journal of Ocean engineering*, 30, pp.1353-1386, 2003.

Choi, B. H., Hyun Min Eum and Seung Buhm Woo: "A synchronously coupled tide-wave-surge model of the Yellow Sea", *Journal of Coastal Engineering*, 47, pp. 381-398, 2003.

Collins, J.I.: Prediction of shallow water spectra, J. Geophys. Res., 77, No. 15, 2693-2707, 1972.

Dean R. G. and Dalrymple R. A: "Coastal processes with engineering applications", Cambridge University Press, 2002.

Eldeberky, Y. and J.A. Battjes: Parameterization of triad interactions in wave energy models, Proc. Coastal Dynamics Conf. '95, Gdansk, Poland, 140-148, 1995.

Eldeberky, Y. and J.A. Battjes: Spectral modelling of wave breaking: Application to Boussinesq equations, J. Geophys. Res., 101, No. C1, 1253-1264, 1996.

Flather, R. A.: "A storm surge prediction model for the Northern Bay of Bengal with application to the cyclone disaster in April 1991", *Journal of physical oceanography,* Vol. 24, pp. 172-190, 1994.

Grant, W.D. and Madsen, O.S: "The continental shelf bottom Boundary layer". *Annu. Rev. Fluid Mech.* 18, 265-305, 1986.

Günther, H., S. Hasselmann and P.A.E.M. Janssen: "The WAM model Cycle 4 (revised version)", *Deutsch. Klim. Rechenzentrm, Techn. Rep. No.* 4, Hamburg, Germany, 1992.

Hasselmann, K., T.P. Barnett, E. Bouws, H. Carlson, D.E. Cartwright, K. Enke, J.A. Ewing, H. Gienapp, D.E. Hasselmann, P. Kruseman, A. Meerburg, P. M uller, D.J. Olbers, K. Richter, W. Sell and H. Walden: Measurements of wind wave growth and swell decay during the Joint North Sea Wave Project (JONSWAP), Dtsch. Hydrogr. Z. Suppl., 12, A8, 1973.

Hasselmann, K.:"On the spectral dissipation of ocean waves due to whitecapping, *Bound.-layer Meteor.*, 6, 1-2, 107-127, 1974.

Hasselmann, S. and K. Hasselmann: A symmetrical method of computing the non-linear transfer in a gravity-wave spectrum, Hamburger Geophys. Einzelschr., Serie A., 52, 8, 1981.

Hasselmann, S., K. Hasselmann, J.H. Allender and T.P. Barnett: Computations and parameterizations of the nonlinear energy transfer in a gravity wave spectrum. Part II: Parameterizations of the nonlinear transfer for application in wave models, J. Phys. Oceanogr., 15, 11, 1378-1391, 1985.

Janssen, P. A. E. M.: "Wave-induced stress and the Drag of Air Flow over Sea Waves", *Journal of Physical Oceanography*, 19, pp. 745-754, 1989.

Janssen, P. A. E. M.: "Quasi-linear Theory of Wind-Wave Generation Applied to Wave Forecasting", *Journal of Physical Oceanography*, 21, pp. 1631-1642, 1991.

Janssen, P. A. E. M.: "Experimental evidence of the effect of surface waves on the air flow", *Journal of Physical Oceanography,* 22, pp. 1600-1604, 1992.

Kagan, B.A., O. Alvarez and A. Izquierdo: "Weak wind-wave/tide interaction over fixed and moveable bottoms: a formulation and some preliminary results", *Continental Shelf Research*, 25, pp. 753-773, 2005.

KIM, S. Y., Takayama, T. and Yasuda, Y.: "Effect of large tidal variation on storm surge",

Annuals of DPRI, Kyoto Univ., No. 49 B, 2006a.

KIM, S. Y., Takayama, T. and Yasuda, Y.: "Effect of large tidal variation on storm surge in the coast sea of western Korea", *Techno-Ocean 2006/19th JASNAOE Ocean Engineering Symposium*, P-182, 2006b.

Komen, G.J., Cavaleri, L., Donelan, M., Hasselmann, K., Hasselmann, S. and P.A.E.M. Janssen,: Dynamics and Modelling of Ocean Waves, Cambridge University, Press, 532 p. 1994.

Komen, G.J., S. Hasselmann, and K. Hasselmann,: On the existence of a fully developed wind-sea spectrum, J. Phys. Oceanogr., 14, 1271-1285, 1984.

Kowalik, Z. and Murty, T. S.: Numerical modeling of ocean dynamics, *Advanced series on ocean engineering, vol.5,* 1993.

Lalbeharry, R., Behrens, A., Guenther and H., Wilson, L.: "An evaluation of wave model performances with linear and nonlinear dissipation source terms in lake erie", *Proc. 8th int. workshop on wave hindcasting and forecasting*, Hawaii, USA, 2004.

Longuet-Higgins, M. S. and R. W. Stewart: "Radiation stresses and mass transport in gravity waves with applications to surf-beats. *J. Fluid Mech.* 13: 481-504, 1962.

Longuet-Higgins, M. S. and R. W. Stewart: "Radiation stresses in water waves; a physical discussion with applications. *Deep-Sea Res.* 11: 529-562, 1964.

Madsen, O.S., Y.-K. Poon and H.C. Graber: Spectral wave attenuation by bottom friction: Theory, Proc. 21th Int. Conf. Coastal Engineering, ASCE, 492-504, 1988.

Madsen, P.A. and O.R. S_rensen: Bound waves and triad interactions in shallow water, Ocean Engineering, 20, 4, 359-388, 1993.

Mastenbroek, C., G. Burgers, and P. A. E. M. Janssen: "The Dynamical Coupling of a Wave Model and a Storm Surge Model through the Atmospheric Boundary Layer", *Journal of Phys. Oceanogr.*, 23, pp. 1856-1866, 1993.

Matumoto, K., T. Takanezawa and M. Ooe: "Ocean Tide Models Developed by Assimilating

TOPEX/POSEIDON Altimeter Data into Hydro- dynamical Model" : A Global Model and A regional Model around Japan, *Journal of Oceanography*, Vol.56, pp 567-581, 2000.

Mei C. C.: "The applied dynamics of ocean surface waves", World Scientific, 1989.

MPI : http://www-new.mcs.anl.gov/

Murty T. S., R. A. Flather, R. F. Henry: "The storm surge problem in the bay of Bengal", *Progress in Oceanography*, Vol. 16, pp. 195-233, 1986.

Ozer, Jose., Roberto Padilla-Hernandez., Jaak Monbaliu., Enrique Alvarez Fanjul., Juan Carlos Carretero Albiach., Pedro Osuna., Jason C. S. Yu. and Judith Wolf: "A coupling module for tides, surges and waves", *Journal of Coastal Eng.*, 41, pp. 95-124, 2000.

Palma, Elbio D., Matano and Ricardo P.: "On the implementation of passive open boundary conditions for a general circulation model: The barotropic mode", *Journal of Geophysical Research*, Vol. 103, No. C1, pp. 1319-1341, January 15, 1998.

Peng M., L. Xie, L. Pietrafesa : "A numerical study of storm surge and inundation in the croatan-Albemarle-Pamlico estuary system", *Journal of Estuarine, coastal and shelf science*, Vol. 59, pp. 121-137, 2004.

Phillips, O. M.: "The dynamics of the upper ocean", 2nd ed. Cambridge University Press, 1977.

Proctor R. and R. A. Flather:"Storm surge prediction in the Bristol channel-the floods of 13 December 1981", *Continental shelf research,* Vol. 9, No. 10, pp. 889-918, 1989.

Ris, R.C., Holthuijsen, L. H. and Booij, N.: "A third generation wave model for coastal regions part 2. Verification." *Journal of Geophysical Research*, Vol. 104, C4, 7667-7681, 1999.

Sorensen R.M.: "Basic wave mechanics for coastal and ocean engineers", A Wiley-Interscience Publication, 1993.

Takayama, T.: "Present numerical simulations of storm surge and their problems to solve", Lecture Notes of the 38th Summer Seminar on Hydraulic Engineering, 02-B-6, September, 2002.

Takayama, T., Amamori, H., Kim, T. M., Mase, H., Kang, Y. K. and Kawai, H.: "Characteristics of storm surge and wave disasters caused by Typhoon 0314 (Maemi) in Korea", *Annuals of DPRI*, Kyoto Univ., No. 47 A, April 2004.

Tang, Y. M., R. Grimshaw, B. Sanderson and G. Holland: "A numerical study of the storm surge and tides, with application to the North Queensland Coast", *Journal of physical oceanography,* Vol.26, pp. 2700-2711, 1996.

Tang, Y. M., P. Holloway, R. Grimshaw: "A numerical study of the storm surge generated by Tropical Cyclone Jane", *Journal of physical oceanography,* Vol.27, pp. 963-976, 1997.

Tolman, H.J.,: "Effects of numerics on the physics in a third-generation wind-wave model", J. Phys. Oceanogr., 22, 10, 1095-1111, 1992.

WAMDI group:"The WAM model – a ghird generation ocean wave prediction model, *J. Phys. Oceanogr.*, 18, 1775-1810, 1988.

Wu, J.: "Wind-stress coefficients over sea surface from breeze to hurricane, *J. Geophys. Res.,* 87, C12, 9704-9706, 1982.

Zhang, M. Y., and Y. S. Li: "The synchronous coupling of a third-generation wave model and a two-dimensional storm surge model", *Journal of Ocean Eng.*, Vol.23 No.6, pp. 533-543, 1995.